5-2012

Verification of the clinical implementation of the respiratory gated beam delivery technique with synchrotron-based proton irradiation

Yoshikazu Tsunashima

Verification of the clinical implementation of the respiratory gated beam delivery technique with synchrotron-based proton irradiation

By

Yoshikazu Tsunashima, M.S.

APPROVED:

X Ronald Zhu, Ph.D.
Supervisory Professor

Lei Dong, Ph.D.

Radhe Mohan, Ph.D.

Narayan Sahoo, Ph.D.

Sastry Vedam, Ph.D.

Peter A Balter, Ph.D.

Susan Tucker, Ph.D.

APPROVED:

Dean, The University of Texas
Health Science Center at Houston
Graduate School of Biomedical Sciences

Verification of the clinical implementation of the respiratory gated beam delivery technique with synchrotron-based proton irradiation

A

DISSERTATION

Presented to the Faculty of
The University of Texas
Health Science Center at Houston
and
The University of Texas
M D Anderson Cancer Center
Graduate School of Biomedical Sciences
in Partial Fulfillment

of the Requirements

for the Degree of

DOCTOR OF PHILOSOPHY

by

Yoshikazu Tsunashima, M.S.

Houston, Texas

May 2012

ACKNOWLEDGEMENTS

I would like to thank my advisors, Dr. X Ronald Zhu and Dr. Lei Dong for their excellent supervision and thoughtful guidance throughout this project. I also would like to thank my supervisory committee members, Dr. Radhe Mohan, Dr. Narayan Sahoo, Dr. Sastry Vedam. Dr. Peter A Balter, and Dr. Susan Tucker for their advice and scientific expertise, which greatly enhanced the quality of this work.

I would like to express my sincere gratitude to Dr. Michel Gillen, Dr. Falk Poenisch, Dr. Xiaofei Song, Dr. Heng Li, other physicists and other physics assistants at the Proton Therapy Center in Houston for giving me an opportunity to do my experiment for this study and for all their help and advice in the experiment. I also wish to extend my sincere gratitude to all the engineers at HITACHI, Ltd. for technical advice and assistance with the PROBEAT unit. And also I would like to thank my student colleagues in our research group for their valuable input during scientific discussions.

Most importantly, I would like to thank Dr. Radhe Mohan for giving me an opportunity to study in the Medical Physics program within the Graduate School of Biomedical Sciences, University of Texas at Houston and the M.D Anderson Cancer Center. I would like to thank Dr. Tina M Briere for her patient guidance and

enthusiastic help in my life. Without their cooperation and help, this research could not have been completed.

Finally, I would like to thank my parents and my brother for being a constant source of inspiration and encouragement.

Abstract

Verification of the clinical implementation of the respiratory gated beam delivery technique with synchrotron-based proton irradiation

Publication No._____*

Yoshikazu Tsunashima, M.S.

Supervisory Professor: X Ronald Zhu, Ph.D.

The clinical advantage for protons over conventional high-energy x-rays stems from their unique depth-dose distribution, which delivers essentially no dose beyond the end of range. In order to achieve it, accurate localization of the tumor volume relative to the proton beam is necessary. For cases where the tumor moves with respiration, the resultant dose distribution is sensitive to such motion. One way to reduce uncertainty caused by respiratory motion is to use gated beam delivery.

The main goal of this dissertation is to evaluate the respiratory gating technique in both passive scattering and scanning delivery mode. Our hypothesis for the study was that **optimization of the parameters of synchrotron operation and respiratory gating can lead to greater efficiency and accuracy of respiratory gating for all modes of synchrotron-based proton treatment delivery**. The hypothesis is tested in two

specific aims. The specific aim #1 is to assess the efficiency of respiratory-gated proton beam delivery and optimize the synchrotron operations for the gated proton therapy. A simulation study was performed and introduced an efficient synchrotron operation pattern, called variable T_{cyc}. In addition, the simulation study estimated the efficiency in the respiratory gated scanning beam delivery mode as well.

The specific aim #2 is to assess the accuracy of beam delivery in respiratory-gated proton therapy. The simulation study was extended to the passive scattering mode to estimate the quality of pulsed beam delivery to the residual motion for several synchrotron operation patterns with the gating technique. The results showed that variable T_{cyc} operation can offer good reproducible beam delivery to the residual motion at a certain phase of the motion. For respiratory gated scanning beam delivery, the impact of motion on the dose distributions by scanned beams was investigated by measurement. The results showed the threshold for motion for a variety of scan patterns and the proper number of paintings for normal and respiratory gated beam deliveries. The results of specific aims 1 and 2 provided supporting data for implementation of the respiratory gating beam delivery technique into both passive and scanning modes and the validation of the hypothesis.

Table of Content

List of Figures

List of Tables

Chapter 1. Introduction

1.1 The benefit of the application of proton beams in radiotherapy

The idea for the clinical use of protons for cancer therapy was first discussed in the paper “Radiological Use of Fast Protons” published by Dr. Robart Willson in 1946 (Willson 1946). In 1950, proton beams were first used on human patient treatment by Tobias et al (1958). Following this early success, research activities on the clinical use of proton therapies for cancer treatment were initiated at some of the high energy physics facilities throughout the world (Larsson 1958, Kjellberg 1962). Between 1980 and 1990, hospital-based proton therapy facilities began to be built, and the role of the proton therapy moved from basic research to the clinic (Slater 1991, Tsujii 1993). Since 2000, more than 18 proton therapy facilities have been in operation, and proton therapy is fast becoming an established treatment method in radiation therapy.

The use of proton beams as a source of therapeutic radiation provides a substantial dosimetric improvement over conventional sources of radiation such as high-energy x-rays (Tsujii 1993, Shioyama 2003, Chang 2006). This is due to one of the physical characteristics of proton beams, the Bragg peak, in which protons stop abruptly in a medium and deliver almost no dose beyond the end of the proton beam range (Wilson 1946, Bonett 1993, Pedoroni E 1995, Smith 2006). This unique physical

characteristic brings about a clinical advantage especially for sparing radiation sensitive Organs at Risk (OAR) (ICRU 62). Dose conformity created by the proton beams can allow for increased target doses for better local tumor control without increase in, or even with reduction of, normal tissue toxicities compared to photon treatment. In order to achieve highly conformal three-dimensional beam delivery in proton therapy, a sophisticated beam delivery method is employed. The proton beam's depth direction conforms to the target shape in the beam axis direction, resulting in the so-called beam modulation in the depth direction. The proton beam also conforms to the collimator shape that is based on the 2D data of the target projected into the beam direction.

1.2 Methods for delivering a 3D proton dose distribution: Passive scattering and Beam scanning techniques

It is well known that there are two types of 3D uniform field delivery techniques in proton therapy. One is passive scattering technique (Bonett 1993, Koehler1975 and 1977), which broadens the proton beam in the lateral and depth directions using scatters and energy modulators. The second is beam scanning, in which the tumor is "painted" in three dimensions with a narrow proton beam using steering magnets

(Bonett 1993, Pedoroni E 1995). It is often easier to create a similar or usually more conformal treatment plan in proton therapy than IMRT, typically with better sparing of the normal organs from high doses

These techniques have been developed to create conformal dose distributions that concentrate the dose only to a target volume. The passive scattering method is a rather classic technique commonly used for many sites, including prostate, head and neck, liver, esophagus and lung. Especially for liver, esophagus and lung treatment, Proton Medical Research center in University of Tsukuba has a lot of clinical experience with the passive scattering method (Nakayama 2009, Sugawara 2005, Shioyama 2003). The scanning beam technique is newer and is currently used in fewer proton centers. It offers the possibility of higher conformality and obviates the need for compensators and energy modulators. From a historical point of view, the scanning techniques have been used selectively for the organs that do not move much during beam delivery because the protons in principle stop at the same point as long as the beam path length is constant. However, if the organ moves, the beam path consequently changes due to the motion. In this case, the proton's end of range is unpredictable, and this may cause either overdosage to the target and/or surrounding organs or underdosage to the target in passive scattering method (Engelsman 2006).

On the other hand, for the scanning mode the over and under dosage occur scan layer by layer due to the organ motion. The total delivered dose to the target is so deteriorated that it is very hard to predict the actually dose on the treatment planning. It is important to note that motion affects the resulting dose distributions for both passive and scanning mode, and this may be of particular importance for hypo-fractionated treatments where there is not adequate time for the dose distributions to be averaged out by the number of treatment fractions. It is therefore quite important to be overcome the difficulties in treating mobile organs for both the passive and scanning beam delivery techniques.

1.3 Difficulties in maximizing the benefits of proton therapy for mobile tumors

In the case of treatment of mobile tumors, maximizing the clinical advantages of proton therapy is made more difficult due to patient breathing. The target motion causes not only target misses from the beam delivery field but also undesirable dose distributions due to range fluctuations and anatomical motion. Thus, although the proton Bragg peak is fully used as a benefit of the proton therapy, this physical characteristic sometimes conversely becomes the weakness of proton therapy. This is because, if the radiological path length is changed due to motion, the protons either do

not reach or pass beyond the planned depth (Minohara 2003, Mori 2008). This can be seen in the case of a lung tumor, as described below.

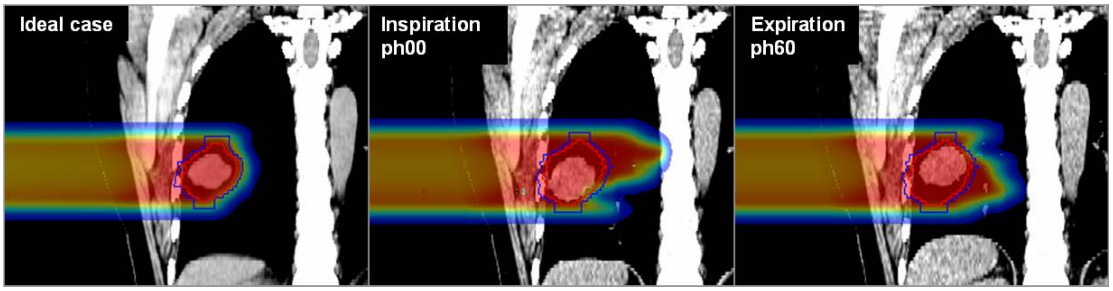

Figure 1- 1. Variation of the dose distribution in the depth direction due to target motion. Red contour: the IGTV. Blue contour: the CTV. Left: the ideal case in which the IGTV and CTV fully covered and the dose distribution terminates abruptly after the target. Middle: Ph00 represents the full inspiration phase Right: ph60 represents an expiration phase. In both breathing phases, high dose areas extend beyond the target and the IGTV and CTV are not fully covered.

Figure 1-1 shows the variation in the radiological path lengths due to target motion. The Gross Tumor Volume (GTV) accounting for tumor motion (termed the Internal Gross Tumor Volume (IGTV)) and the Clinical Target Volume (CTV) were created from the Maximum Intensity Projection CT (MIP) made from a 10-phase 4DCT data set covering the entire range of breathing motion. The compensator was created on the Average CT, or the average of the 10 phases. Dose calculations were performed on each CT data set from phase 0, full inspiration to 60, full expiration. The dose calculation algorithm used a ray-casting model, which is convenient for the purpose of expressing proton range information (Chen 1979). The left figure represents an ideal treatment, in which the IGTV and CTV are fully covered and the dose distribution into the lung is minimal. However the middle (inspiration phase) and right (expiration phase) figures show that the ideal plan is barely reflected and the delivered dose distribution is significantly different due to patient breathing motion. The maximum depth points change depending on the tumor location, as shown in the doses delivered at inspiration and expiration phases, and in both cases the dose to the normal lung is greater than in the ideal case.

1.4 Necessity for respiratory-gated proton delivery for treating tumors that move due to patient breathing

The uncertainties caused by patient setup and organ motion can affect the proton dose distribution inside the patient's body (Minohara 2003, Mori 2008) In principle, marginal errors may need to be taken into account to compensate for the uncertainties in conventional treatment delivery (Engelsman M 2006). For photon therapy, the margin can be applied to compensate for the entire tumor motion. This is based on the assumption of free-breathing beam delivery using 4DCT (Kang 2007). However it is not appropriate to make use of similar concepts for proton therapy because of increased sensitivity of proton transport to local density changes, as shown in figure 1-1. Therefore we need to handle this as a "proton specific" issue. There are generally two methods to perform beam delivery with respiratory motion. One is to manage patient breathing and reduce the magnitude of the patient's breathing as much as possible or force the patient's breathing into a regular motion (Wong 1999, Kini 2003, Mageras 2004). Inhale and exhale breath hold techniques are also forms of respiratory management (Mageras 2004). The drawbacks of respiratory management method are, however, that the uncertainty and accuracy are strongly dependent on operator (physicist or therapist) and/or patient compliance (Ref, show the proof or paper). An

alternative method is to synchronize proton beam delivery with the patient's breathing. Proton beam delivery is initiated only when the target volume is in a certain phase of the patient's respiratory cycle. This technique is called respiratory gating (Inada 1992, Kubo HD 1996, Shirato H 2000). It is similar to capturing a given moment of target motion, during which dose are delivered to the target. This is also a snapshot of beam delivery from the treatment planning point of view. Compared to the full range of breathing motion, it is much easier to take into account the uncertainty in target motion associated with gated patient breathing because the range of motion is dramatically reduced.

Respiratory-gated beam delivery with proton beams is a highly sophisticated beam delivery method. Because this method selectively uses a fraction of the beam cycle, beam delivery time becomes a concern and will depend on the specifications of the accelerator used in a particular proton facility. It is well known that there are two types of accelerators used for cancer treatment, the cyclotron and the synchrotron. The main conceptual difference between the two is that the proton beam generated from a cyclotron is a continuous beam, while the beam from a synchrotron is a pulsed beam with a certain cycle. This difference considerably influences the beam delivery time and the quality of beam delivery. With synchrotron-based beam delivery, the

complicated timing and cycle of beam extraction from the synchrotron greatly affects the beam delivery. This is not, however, a concern for cyclotron-based beam delivery. The MD Anderson Proton Therapy Center in Houston (PTCH) employs the PROBEAT proton beam delivery system (Hitachi America Ltd., Tarrytown, NY) and is a synchrotron-based proton treatment system. Therefore the following discussion will focus on the issues associated with synchrotron based beam delivery.

1.5 Review of literature relevant to this study

To date, respiratory-gated proton beam delivery using both passive and beam scanning methods has not been validated in the literature, although there have been some papers published for carbon therapy (Minohara 2003, Christoph B 2008, Grozinger2006). There are a few published papers that deal with proton beam delivery to a moving target (Paganetti 2005, Kang 2007); however, these simulation studies using the passive scattering method focus more on the dosimetric impact of free-breathing motion based on 4D simulation.

The main issue with current realistic treatment planning performed in the clinic is how to achieve either a planned beam delivery or dose distribution for the cases with a moving target that is not taken into account in the treatment planning.

Clinically, treatment planning is performed based on a static or three-dimensional space, and is not done in a dynamic, so called 4D space.

For the facilities considering using respiratory-gated proton beam delivery, it is very important to consider the optimized operation of respiratory-gated beam delivery from both the efficiency and quality in terms of accuracy and precision viewpoints. Nevertheless, there have not been adequate studies that seriously consider the feasibility of the respiratory gating technique for synchrotron-based passive scattering and beam scanning (including Intensity Modulated Proton Therapy, IMPT), accounting for the trade-off between the efficiency of the beam delivery and the dosimetric quality.

1.6 Hypothesis

Achieving clinical implementation of respiratory-gated proton beam delivery is a very urgent mission that will increase the sophistication of proton treatments, especially for the lung, esophagus and liver. This has been established as the goal of my research. I have planned and proceeded with research projects based on the following hypothesis:

"**Optimization of the parameters of synchrotron operation and respiratory gating can lead to greater efficiency and accuracy of respiratory gating for all modes of synchrotron-based proton treatment delivery**."

The hypothesis was tested using the following specific aims.

Specific aim 1

Assess the efficiency of respiratory-gated proton beam delivery and optimize the accelerator operations for synchrotron-based gated proton therapy

In synchrotron-based proton beam delivery, optimizing the cycle of the magnet excitation pattern to synchronize with patient breathing is critical to the efficiency of respiratory-gated proton delivery. I will design a computer simulation program to emulate respiratory-gated beam delivery using various operating conditions of the synchrotron accelerators. Using a realistic simulation with actual patient breathing data, the efficiency of synchrotron-based respiratory-gated proton beam delivery will be estimated. From analysis of the results from simulation, we will propose the most efficient method for synchrotron-based respiratory-gated treatment for both passive scattering and beam scanning delivery techniques.

Specific aim 2

Assess the accuracy of beam delivery in respiratory-gated proton therapy

To evaluate the quality of the gated beam delivery, we will evaluate the positional accuracy of the target volume and the precision of respiratory-gated beam delivery using a simulation technique. A wide gating window, irregular breathing or imperfect gating trigger will induce a positional inaccuracy especially for the scanned pencil beam. The analysis will be done with several patient breathing data sets. In addition to the simulation, we will conduct an experiment to validate gated treatment delivery through measurements using films and a motion phantom. Using the motion phantom, a mobile target will be driven by computer-programmed motion based on patient breathing data. Film will be placed at the center of the designated target region. An experiment will be designed to compare measured dose from: 1) the beam delivered to the moving phantom with no motion, 2) non-gated beam delivery to the moving phantom and 3) gated beam delivery to the moving phantom. This will be conducted for both the passive and the beam scanning modes. The trade-off between treatment delivery accuracy and efficiency will be evaluated. For further evaluation of these results, it is also important to show the relative benefit to patients who receive

respiratory-gated treatment compared to non-gated treatment. Such an analysis will indicate the dosimetric benefits of respiratory-gated proton therapy for mobile tumors.

In order to validate the hypothesis, the purpose of the first research project is to develop methods to optimize beam delivery of synchrotron-based proton beams for mobile tumors. To accomplish this, I plan first to conduct a simulation study and a series of measurements. Secondly, from the results I will determine the efficiency and quality of synchrotron-based respiratory-gated beam delivery. In the simulation, several electrical signals from the accelerator operation pattern and the patient's respiratory signal information run simultaneously as if the respiratory-gated beam delivery is virtually performed on the computer. The result obtained from the simulation will be the basis to improve treatment efficiency and quality. In addition, I will conduct validation experiments in order to support the simulation results. The implementation of the optimized beam delivery into clinical practice will allow us to significantly improve the efficiency and accuracy of proton treatment for lung cancer patients.

Chapter 2. Overview of synchrotron and beam delivery system for proton therapy

For this research project, it is very important to understand the characteristics of synchrotron operation and the operation parameters used in passive scattering and scanning modes. In this section synchrotron operation specific to the PTCH are described in detail.

2.1 Synchrotron-based proton beam delivery system at the University of Texas MD Anderson Cancer Center

The Proton Therapy Center at Houston (PTCH) at the MD Anderson Cancer employs the PROBEAT proton beam delivery system (Hitachi America Ltd., Tarrytown, NY). This synchrotron-based proton treatment system governs the treatment rooms, all control systems and other components associated with treatments. The PTCH has three treatment rooms with rotating gantries, two equipped for passive scattering mode and one for beam scanning mode, two fixed beam line treatment rooms, a synchrotron with a beam transport system and the control system (figure 2-1). The synchrotron at PTCH is 23 m in circumference and can accelerate proton particles from 70 to 250 MeV. A linear accelerator (linac) first injects the proton accelerated up to approximately 7 MeV into the synchrotron. The synchrotron then starts to accelerate the proton particles. The

linac is sometimes called an “injector” or “pre-accelerator” and is, in general, necessary for synchrotron operation. In the next section the synchrotron operation parameters in both passive and scanning modes are discussed.

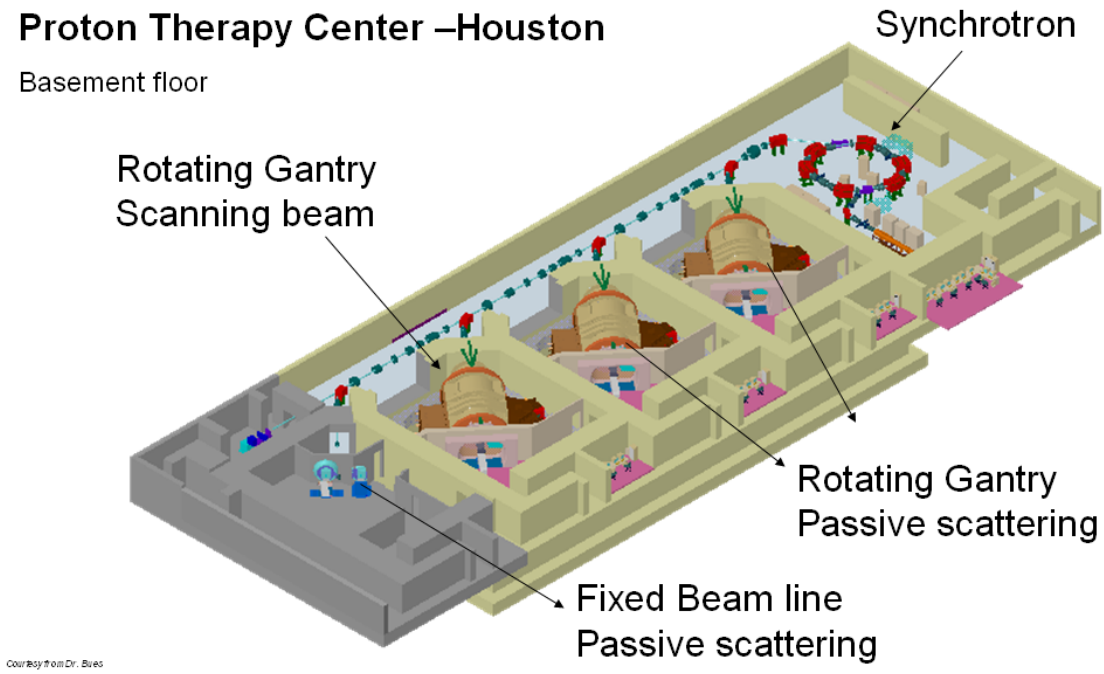

Figure 2- 1. Overview of PTCH at the MD Anderson Cancer.

2.2 Synchrotron operation pattern parameters: Passive scattering mode

The synchrotron employs the slow extraction method to extract and transport beams (Tomizawa 1993, Noda 1996) to each treatment room. In this process, synchrotron operation is governed by a sequence of phases within the magnet excitation pattern. This conceptually comprises three distinct phases: acceleration (T_{acc}), flat-top (T_{FT}), and deceleration (T_{dec}). A series of these three phases composes one cycle of the synchrotron magnet excitation pattern, which is defined as $T_{cyc} = T_{acc} + T_{FT} + T_{dec}$ in the time domain. During each excitation cycle, proton extraction is available only during the flat-top period, T_{FT}; in other words, proton beam delivery is not available during T_{acc} and T_{dec} phases in the excitation pattern, which are the main reason that the synchrotron beam is a pulsed beam. This will be important when we consider the efficiency of respiratory-gated techniques. The conceptual magnet excitation cycle is shown schematically in Figure 2-2. T_{acc} and T_{dec} are fixed values (about ~ 1.05 sec each) independent of the selected beam energy. T_{cyc} is a user-selected value from 2.6 – 7.1 s where, since T_{acc} and T_{dec} are fixed values, effectively $T_{FT}=T_{cyc}$-2.1.s is selectable parameter. The T_{cyc} needs to be preset prior to the start of beam delivery for each treatment (treatment field). Once T_{cyc} is set, the user cannot change its value until the completion of the beam delivery. The flat-top phase, T_{FT}, is the phase during which the

protons are available for extraction and delivery. Thus synchrotron-based proton beam delivery is a pulsed beam delivery, and it is quite different from the continuous beam delivery available from a cyclotron. The pulsed beam is called a ”spill”. The pulse length of a spill is defined as T_{spill} in this study, and it has a fixed value, T_{spill}=0.5 sec.

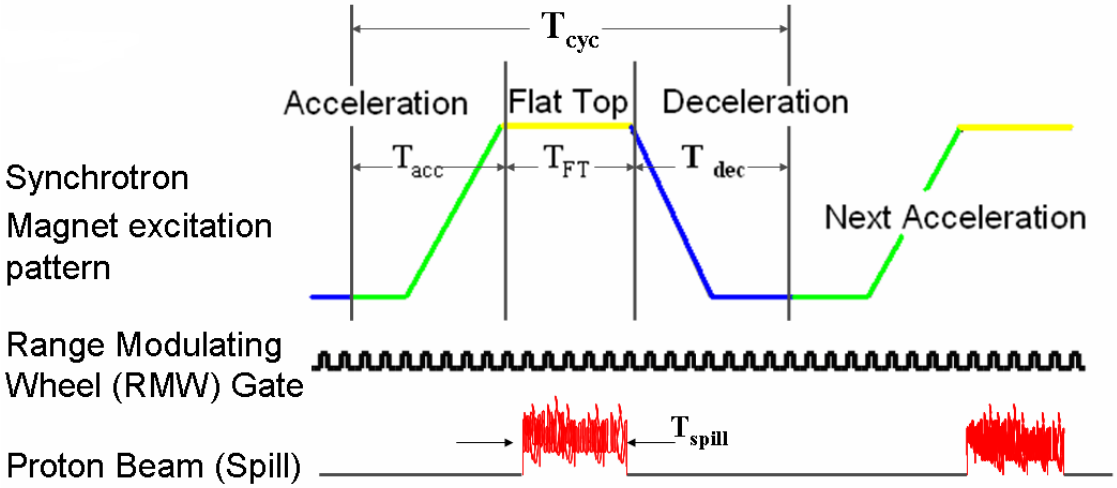

Figure 2- 2. Time sequence of the synchrotron magnetic excitation pattern with fixed T_{cyc}. T_{cyc} consists of an acceleration time (T_{acc}), a flat-top time (T_{FT}), and a deceleration time (T_{dec}). For non-gated proton beam delivery, protons are available for delivery during the flat-top phase.

Because both T_{acc} and T_{dec} are fixed, T_{FT}, calculated by T_{cyc}= 2.1 s, is the only phase that can be varied with the length of T_{cyc} and can range from 0.5 to 5.0 s. Once a given value of T_{cyc} is set, the synchrotron keeps running with T_{cyc} governed by T_{FT} until the preset MU beam delivery is completed. The value of T_{FT} is not allowed to change during ongoing beam delivery. The deceleration phase initiates following completion of the preset flat-top phase, T_{FT}, or when all proton beams available to be delivered in one operation cycle are delivered. In the case when the actual duration time of the flat-top, T_{FT}, is less than T_{FT}, the remaining time $[T_{cyc}-(T_{acc}+T_{FT}+T_{dec})]$ becomes dead time (figure 2-3), and this dead time must pass before the next cycle begins.

The normal operation pattern described above is named “fixed T_{cyc} mode” in this study. There is also another operation pattern named “variable T_{cyc} mode”, where T_{FT} is not a fixed value but a dynamic variable; it dynamically varies from the initial default value of 0.5 s (2.7 sec for T_{cyc}) to 5.0 s (7.2 sec for T_{cyc}) . This is the major important difference between fixed T_{cyc} mode and variable T_{cyc} mode. In variable T_{cyc} mode, the duration time of T_{FT} can dynamically change up to 5.0 s to wait for the respiratory gate signal to be turned on. Following the beam delivery and the deceleration phase, the next magnet excitation pattern with T_{cyc} starts immediately after the end of the previous deceleration phase. Such a variable T_{cyc} operation pattern

may reduce the time consuming process of waiting in the previous deceleration phase to be completed as happens with fixed T_{cyc} mode.

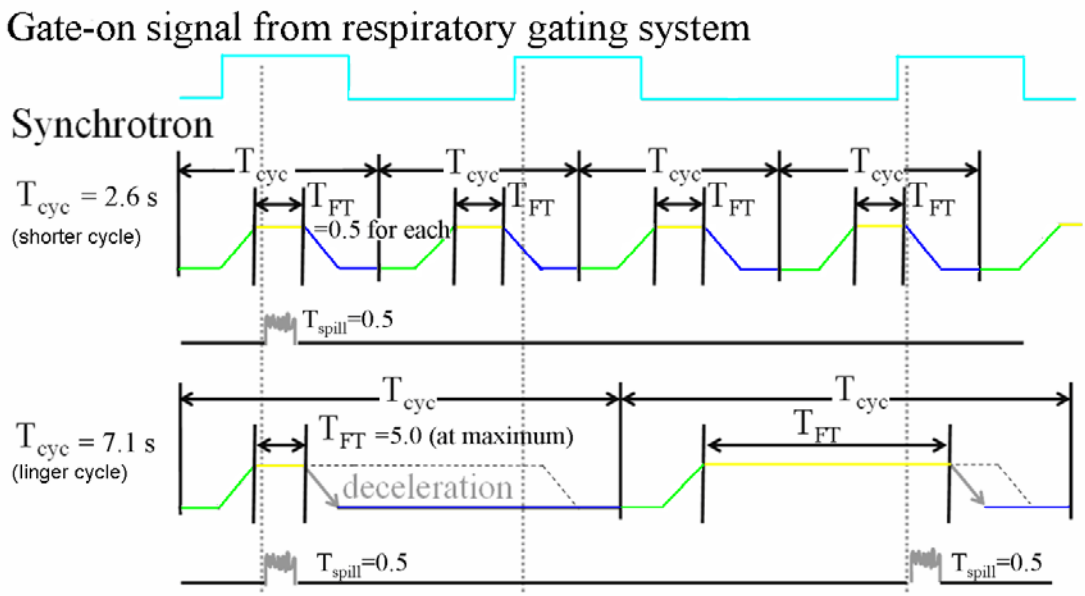

Figure 2- 3. Fixed Tcyc synchrotron magnet excitation pattern with short T_{cyc} (T_{FT}=0.5 s) and long T_{cyc} (T_{FT}=5.0 s).

2.3 **The relationship between the Rotating Modulation Wheel (RMW) and beam delivery**

A Spread-Out Bragg Peak (SOBP) provides the possibility to deliver a uniform depth dose to the target volume. The SOBP is a superposition of quasi-monoenergetic beams of different intensity. In the passive scattering method, a range modulator shifts the proton beam towards the proximal direction corresponding to a given SOBP size. Summation of the all distributions of these modulated protons forms a uniform dose distribution in the depth direction along the beam axis. The protons passing through each path length in the steps are modulated in range and the SOBP is created. Currently, the most commonly used method employs a range modulator wheel (RMW, figure 2-4). It has a cylindrical shape of ridged steps and is composed of three segments on the same ridge-shaped steps. The RMW rotates at the constant rate of 400 rpm. The proton beam axis is placed at a small segment of the RMW. During RMW rotation, as the protons pass through the rotating RMW, some of protons are modulated proximally depending on the beam path length of the corresponding step on the beam axis at the moment. The length of the SOBP is governed by the number of steps of the RMW the protons have passed through. The number of the steps that are needed to create a given SOBP length is controlled by turning the proton beam on and off to just

irradiate the corresponding steps (Figure 2-5). This method is called “Gating-off”. It is carefully controlled to generate a uniform SOBP. However, it also reduces the number of protons that can be delivered in a given time and thus the dose rate drops (typically by a factor of 2).

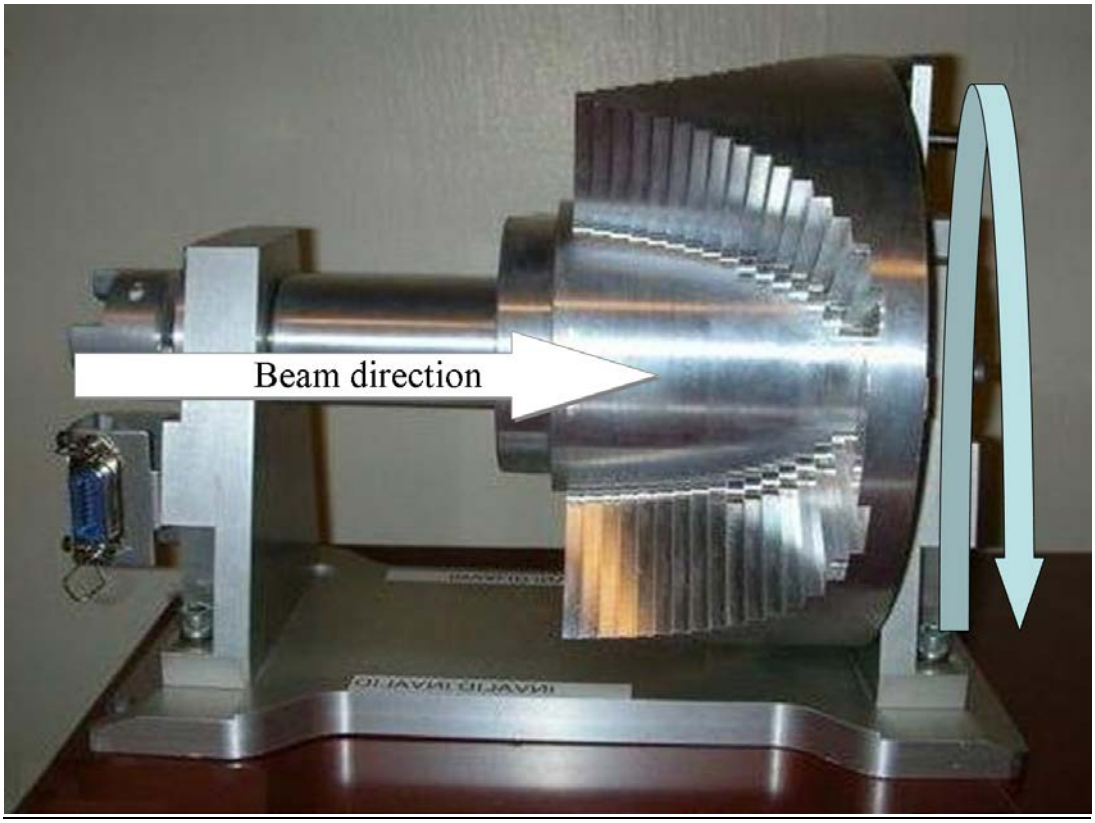

Figure 2- 4. Range modulator wheel (RMW).

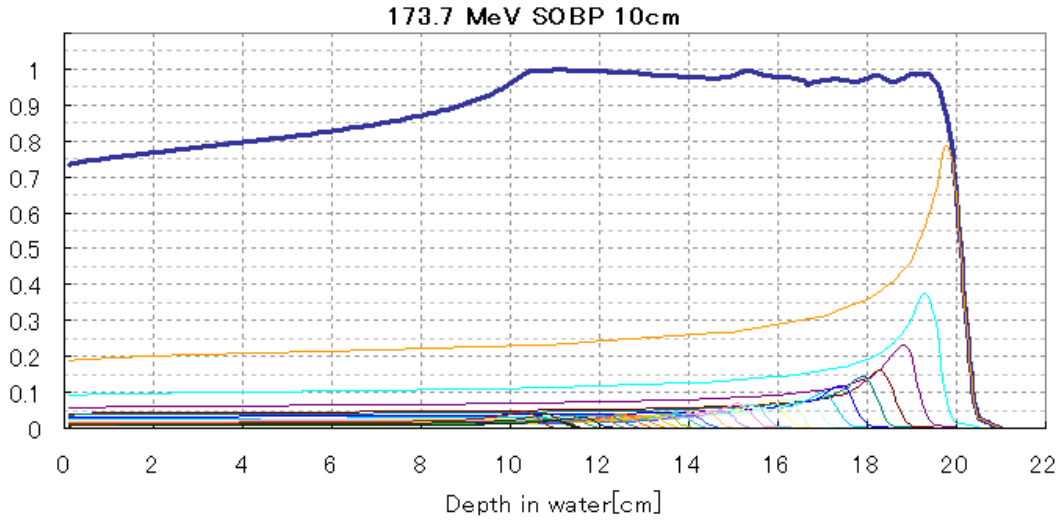

Figure 2- 5. Spread-Out Bragg Peak (SOBP) made with the RMW.

2.4 Synchrotron operation pattern parameters: Beam scanning mode (spot scanning)

Figure 2-6 shows the schematics of details about the synchrotron magnet excitation operation in scanning mode. The main difference in scanning mode from the passively scattering mode is that the synchrotron needs to adjust the acceleration energy for completion of beam delivery to a target volume in one treatment session. In passively scattering mode, the acceleration energy would never change during one session. However the scanning beam delivery needs to change the proton acceleration energy in order to change the depth in scan layer of the target volume from the deepest layer (highest energy) down to the shallowest layer (lowest energy). In accordance with the changing beam energy, the acceleration time, T_{acc}, is consequently supposed to change gradually layer by layer. On the other hand, regarding the deceleration phase, for the purpose of avoiding a hysterics of the excited magnets and maintaining the following acceleration phase in the next cycle stable, an additional acceleration is applied to excite the magnet up to a certain constant level, E_{const}, from a given energy level in the flattop phase, E_{FT}, prior to transition to the deceleration phase. Therefore the re-acceleration phase (T'_{acc}) is variable depending on the difference in energy level between E_{const} and E_{FT}. The deceleration starts at the re-accelerated energy level, E_{const},

and immediately after the end of the deceleration phase the next acceleration phase, n+1, is initiated. Since the deceleration phase basically starts from a constant energy level, the decelerate time, T_{dec} is constant. However supposing T'_{acc}, T_{dec} at a given phase, n, is expressed here by $T'_{acc,n}$ and $T_{dec,n}$, and also T_{acc} in next the phase, n+1, also is expressed by $T_{acc,n+1}$.

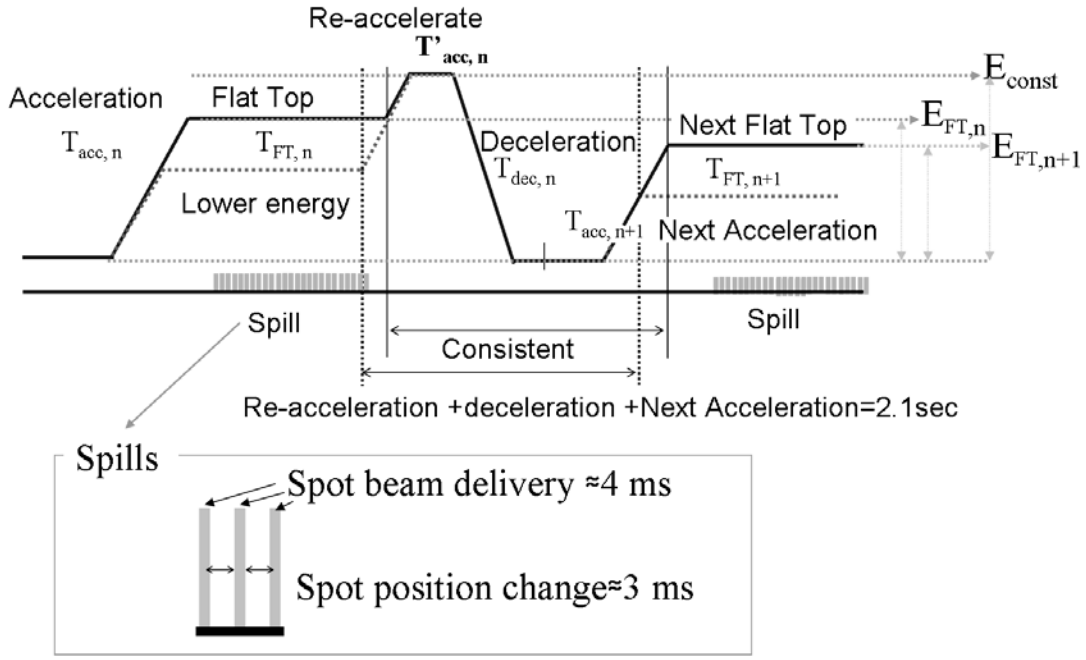

Figure 2- 6. Synchrotron magnet excitation pattern for spot scanning mode.

The spill control (beam-on and -off) for scanning mode is also different from that for passive scattering delivery mode. The beam delivery in passive scattering mode is off when the spill with 0.4 MU and T_{spill} duration time is delivered. The completion of the beam delivery for one treatment session is controlled with a preset dose (MU). While, because the scanning beam delivery is mainly controlled by scan position files rather than preset dose, following the spot file, the synchrotron is controlled to deliver as many spot beams as possible at each energy layer (depth) within the maximum duration time of T_{FT}. This means that the length of T_{FT} needs to be dynamically variable depending on the number of spots to be delivered in each layer. The variable T_{cyc} mode operates on the basis of a minimum cycle, T_{cyc}= 2.1 +T_{FT} sec where the T_{FT} can be flexibly extended up to 5.0 sec to deliver as many spot beams as possible.

When T_{FT} reaches 5.0 sec, the flat-top phase is immediately terminated, even if the respiratory gate is still on and the scanning beam is being delivered, and the deceleration sequence is sequentially started. The next acceleration sequence starts immediately following the deceleration phase of the current T_{cyc}. Scanning beam delivery at a given spot takes t_s =3~4 ms, while the transition time of the scanning beam on a single layer between spots is about t_m= 3 ms at a minimum (figure 2-5), and these numbers vary depending on the spot distance and beam energy. Thus the time for

each spot beam delivery, t_{spot}, takes in total $t_{spot} = t_s+t_m$. The spill length in scanning beam delivery mode is then calculated by t_{spot} multiplied by the number of spots available to be delivered. In changing the scan layer (scan depth), it takes approximately 2.1 s to change the energy to scan the next layer, where the accelerator needs to decelerate and move to the next acceleration phase.

Chapter3. **Specific aim 1: Passive scattering mode**

A study of efficiency of passive scattering beam delivery with respiratory gated proton beam delivery

3.1 Introduction

The main goal of this specific aim is to estimate optimal synchrotron operations for synchrotron-based respiratory gated proton beam irradiation with passively scattered protons. The beam delivery time, which is a part of the patient treatment time, is estimated from a simulation study where various types of synchrotron operations run with respiratory gating mode. From the result, the optimal synchrotron operation parameters are determined to ensure efficient beam delivery in respiratory-gated beam delivery mode.

3.2 Methods and Materials

3.2.1.1 Proton beam delivery parameters

In order to prepare for the simulation study, it is necessary to comprehend synchrotron operation parameters relevant to the efficiency. The following operation parameters and numbers were built into the simulation program.

3.2.1.2 Synchrotron operation

Basic information of a synchrotron operation has been already explained previously in chapter 2. The synchrotron magnetic excitation cycle, T_{cyc}, can be set from 2.7 – 6.5 s prior to the start of beam delivery for each treatment. However once the T_{cyc} is set, it is impossible to change its value until the beam delivery has been completed for each treatment. The values for the acceleration phase, T_{acc}, and deceleration phase, T_{dec}, are fixed (~ 1.1 sec each) for all synchrotron operation. During the flat top phase, T_{FT}, expressed by T_{cyc}-(T_{acc}+T_{dec}), the protons can be extracted. The value of T_{FT} ranges from 0.5 to 5.0 s, and T_{FT} is always < T_{cyc}. T_{dec} usually begins following completion of the flat-top phase. There are two modes of synchrotron operation, distinguished by whether or not the synchrotron remains in the deceleration phase until the passage of the remaining time in the current T_{cyc}.

One of these modes is named as a "fixed T_{cyc}" mode. If the spill has been delivered before completion of T_{FT} (that is, when T_{FT} > T_{sp}), the phase of the magnet excitation pattern shifts to the deceleration phase. Even after the protons are decelerated, this phase still continues until the current T_{cyc} phase is completed normally in non-magnetic excitation status. The shortest possible duration of T_{cyc} in this mode is

2.7 s (T_{acc} = 1.1 s, T_{dec} = 1.1 s, and T_{FT} = 0.5 s), and for non-gated delivery the beam delivery time is shortest and effective dose rate is at a maximum.

The second type of operation is named as a "Variable T_{cyc}" mode. The initial default values of 0.5 s for T_{FT} and 2.7 s for T_{cyc} are variable during every spill. The value of T_{FT} can be dynamically changed from 0.5 s to 5 s to wait for the respiratory gate signal. In addition, the next synchrotron operation cycle begins immediately following completion of the deceleration phase of the previous synchrotron cycle. As a result, it is expected that the variable T_{cyc} mode enables one to reduce time consumed in the deceleration phase in fixed T_{cyc} mode.

Figure 3-1 shows a timing diagram of the respiratory gate signals and synchrotron magnetic excitation patterns in both fixed and variable T_{cyc} mode. Figure 3-1(a) illustrates an example in which the fixed T_{cyc} values have a shorter duration time compared to the average respiratory gate duration. In this case, there is lesser chance of signal match between the flat top and the respiratory gate-on. This consequently leads to a prolonged beam delivery time in respiratory-gated proton delivery. As shown in figure 3-1(b), if the T_{cyc} value is longer than the average respiratory gate duration, most of time would be wasted in the deceleration mode waiting for the completion of the T_{cyc} even though the spill has been delivered in the current T_{cyc}. This also leads to a

worsening of the efficiency of proton delivery under respiratory gating. Thus, inefficiencies occur during fixed T_{cyc} mode, whether the duration time is long or short.

Alternatively, the variable T_{cyc} mode (figure 3-1c), offers the potential to achieve more efficient beam delivery because the synchrotron does not have to spend time in the deceleration phase until the remaining time within T_{cyc} is completed.

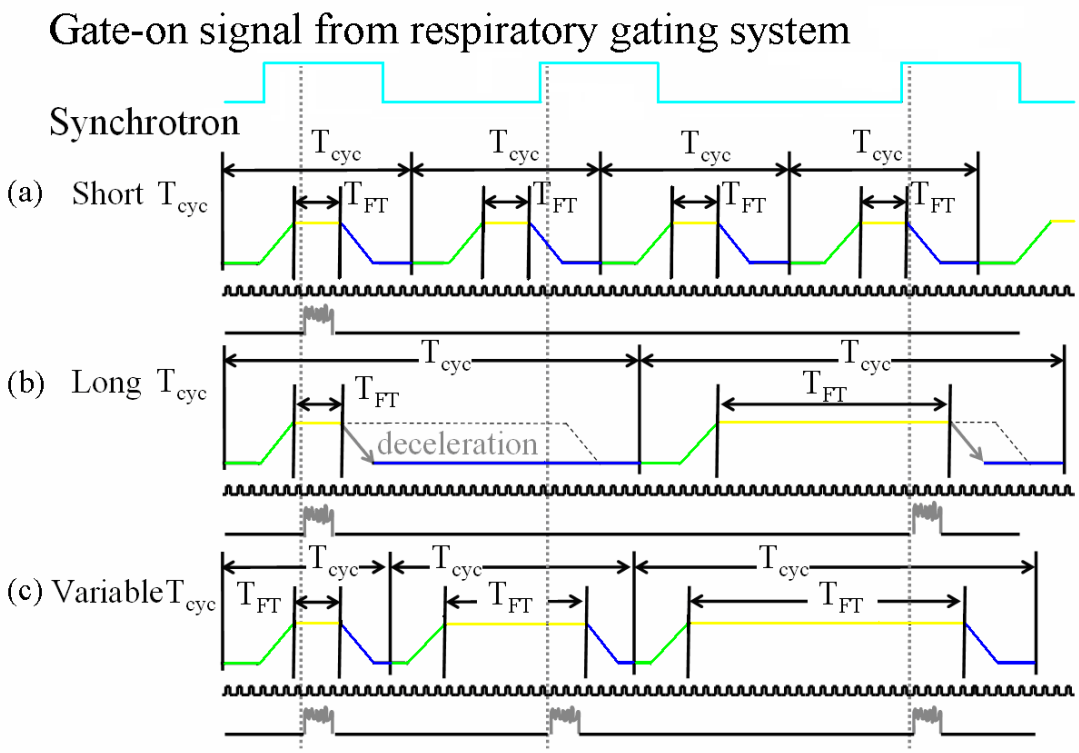

Figure 3- 1. Timing diagram of the respiratory gate signal and synchrotron magnet excitation patterns for fixed (short and long T_{cyc}) and variable T_{cyc}. Three types of T_{cyc} are shown: (a) short T_{cyc}, (b) long T_{cyc}, and (c) variable T_{cyc}. (a) T_{cyc} is too short to synchronize with the respiratory gate signals. (b) There is a long waiting time following deceleration in the first spill delivery. For the second spill, T_{FT} waits for the respiratory gate signal within the preset duration time. This case occasionally induces better efficiency than (a). (c) Variable T_{cyc} can dynamically extend T_{FT} in every T_{cyc} and wait for the next respiratory gate signal. The number of misses of the respiratory gate signal is limited in this case.

3.2.1.3 Uniform proton beam delivery

For each patient treatment, the beam intensity depends on the field size as well as the beam energy. In addition, the Range Modulating Wheel (RMW) also has an influence on the beam intensity. The RMW is a range modulator that has a combination of many steps corresponding to different water equivalent thicknesses (figure 2-4 in the chapter 2). The small portion in the peripheral edge of the RMW is placed on the beam axis. From this point of view, the thickness of the steps seems to be dynamically changing during rotation of the RMW. It rotates at a high speed to create a “Spread out Bragg Peak (SOBP)”. For example, the rotation time of the RMW is, at maximum, approximately 50 ms for a 120 mm SOBP dose distribution. In this case, the beam needs to cross through most of the steps in the RMW. From the beam control point of view, the beam needs to be turned on for the entire RMW rotation. For smaller SOBP sizes consistent with typical lung or liver tumors in this study, assuming the same RMW is used, the beam does not need to be on for entire RMW rotation but the beam needs to be turned on for a certain part of the RMW steps and off for other steps. Therefore the beam “on or off” need to be controlled in binary mode, for instance 50 ms of entire beam on duration time, and the effective beam on duration time can be less than the time resolution of the RPM data, 1/30 second.

The spill data was set to 4 Monitor Units (MU) /1spill in this simulation. The beam current provided by the synchrotron has a consistent intensity spill by spill. The intensity is preserved within 5% for each spill. The effective beam on time caused by the beam turn-on/off during a certain phase of RMW rotation was set to 30% of 50 ms.

3.2.1.4 Patient breathing data

The Real-Time Position Management (RPM) respiratory gating system (Varian Medical Systems, Palo Alto, CA), which indirectly tracks the motion of a patient's chest or abdominal wall during breathing, has been used for clinical operations at MD Anderson Cancer Center mainly for thoracic and liver patients. The RPM system records displacement and phase data of a patient's respiration at the rate of 30 frames per second. Sixty-two sets of free breathing data were acquired for patients who had been enrolled previously in lung cancer treatment studies. These breathing data sets were used for this simulation, which provided unique respiratory gate signals for each patient's breathing pattern and cycle. For each patient breathing data set, the duty cycle of various respiratory gate threshold levels, the mean respiratory motion cycle, and the starting phase of the respiratory cycle were used in the simulation.

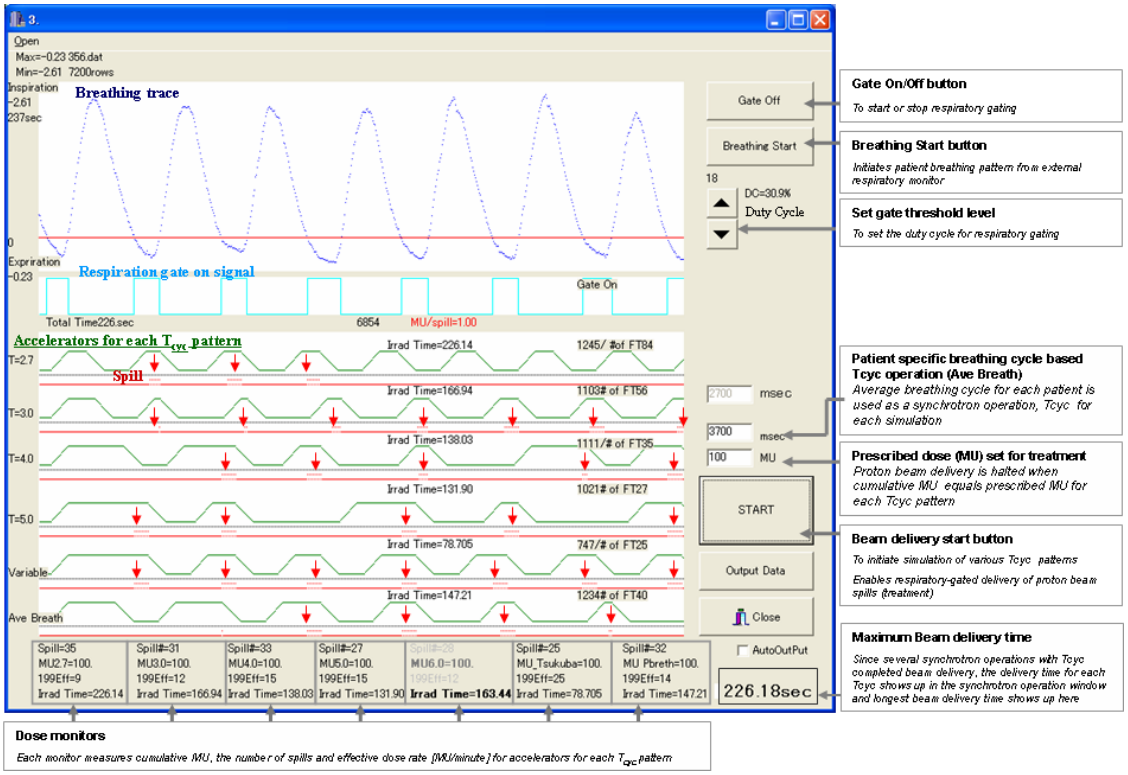

Figure 3- 2. Screenshot of simulation interface. The patient data exported from RPM is used for the simulation. It enables the user to simulate respiratory gated beam delivery for several synchrotrons with different T_{cyc}. The gate threshold level is selectable and the user can perform the simulation with different gate threshold levels.

3.2.2 Respiratory gating simulation interface

A simulation program was developed to estimate the treatment time based on the input of a respiratory pattern and various parameters. This software includes the accelerator operation parameters and can perform a virtual proton beam delivery. The simulation program can import patient breathing data exported from RPM. It enables the user to freely set the respiratory gate threshold level (duty cycle). When the breathing signal is below this level, a respiratory gate signal "on status" is generated. While the accelerator patterns mentioned above sequentially runs on the simulation program at the same time, the accelerator also sends "beam delivery ready" status in the flattop phase. It is also possible to run multiple accelerator operation patterns with different T_{cyc}s and it can show the total beam delivery time for individual accelerator operation.

Figure 3-2 shows the simulation program interface. In the simulations, the user sets the MU values as well as the respiratory gate threshold. Figure 3-3 shows the underlying logical flowchart for the simulation interface. Using the simulation interface the beam delivery times were estimated for several types of synchrotron operations with different T_{cyc}. From this, the optimal synchrotron operation cycle, T_{cyc}, for passively scattered respiratory-gated proton beam delivery were determined on the basis of the following data analysis.

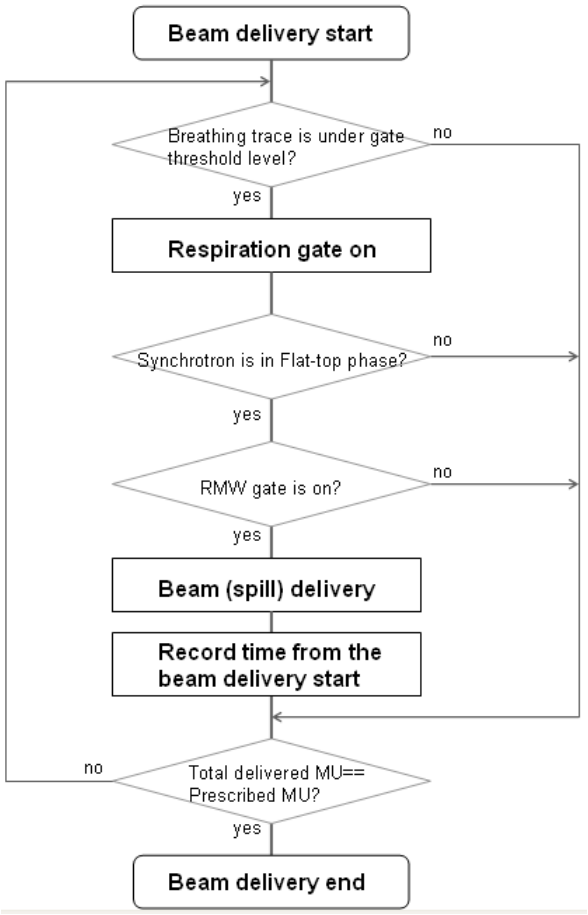

Figure 3- 3. Concept of the simulation interface of respiratory gated beam delivery in passively scattered mode.

3.2.3 Simulations

The simulations were performed for 62 patient breathing data sets to examine the overall beam delivery time for delivery of 100 MU with respiratory gating under different conditions of T_{cyc} and gate threshold levels. The efficiency was examined with an effective dose rate, which is expressed by the prescribed dose of 100 MU divided by the beam delivery time obtained by the simulation. A reference set based on the ideal efficiency of the same amount of radiation (here, again 100 MU) without respiratory gating was used for comparison. In this case, the minimum allowable T_{cyc} value was 2.7 s for the passive scattering mode.

3.2.4.1 Effect of starting phase of beam delivery

Synchrotron based proton beams produce a “spill”, which is a pulsed beam in the time domain. The duration time of an individual respiratory gate signal varies patient by patient. Figure 3-4 shows two simulation results where all simulation conditions were same but the synchrotron magnet pattern has started at different breathing phase by π based on the breathing phase information. One of beam delivery time was almost two times loner than another result just due to beam stating at different phase by π. Thus the chance of signal matching between the synchrotron flat-top phase and respiratory

gate signal varies strongly depending on which phase in the breathing cycle the beam delivery or the synchrotron magnet excitation pattern is initiated. It consequently has a great impact on the efficiency of proton beam delivery. This is called the “starting phase effect” and was taken into account in this simulation. The patient breathing data set exported from RPM includes phase information expressed with values between 0 and 2π (0 represents a peak of the inspiration phase, and π represents the end expiration phase). Using this information, the same simulations were repeated for four different phases: 0, $\pi/2$, π, $3\pi/2$, and 2π (=0 but it means the 0 phase in the next breathing cycle). The average value of these four simulation results is defined as the estimated beam delivery time in this simulation.

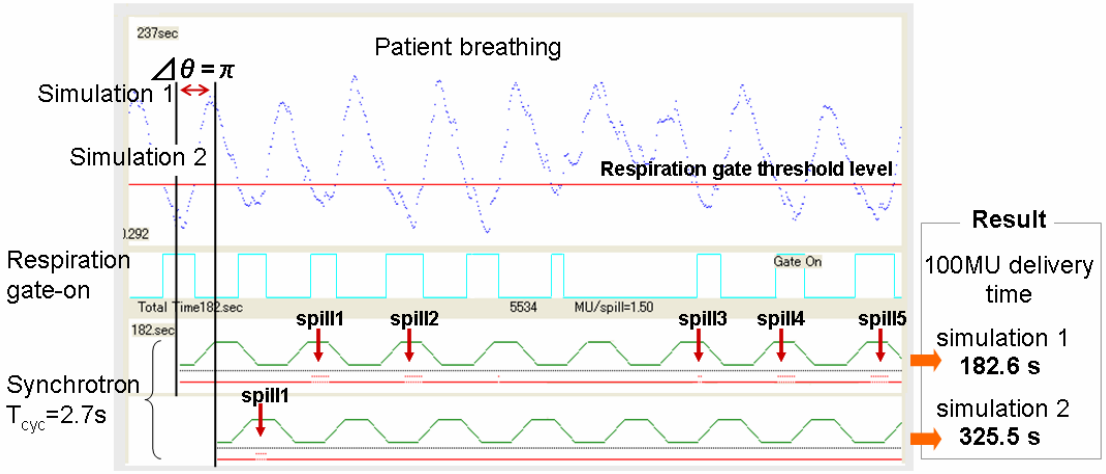

Figure 3- 4. Beam delivery starting phase effect. The same simulation was performed for different phases. Simulation 2 started by π later than simulation 1. The phase information followed RPM data. There was more signal matching between the flat-top phase of the synchrotron and the respiratory gate signal in simulation 1, and therefore the beam delivery time was approximately two times shorter than simulation 2. The beam delivery starting phase to a patient breathing has a great influence on the beam delivery time.

3.2.4.2 Effect of T_{cyc} duration

The respiratory-gated beam delivery for different T_{cyc} based synchrotron operations were simulated. There were, in total, seven T_{cyc}s used for the simulation: (i) fixed T_{cyc} ranging from 2.7 s (the minimum permitted value) up to 6.0 s, (ii) T_{cyc} preset to the average breathing cycle for each patient, and (iii) variable T_{cyc} (explained in section *3.2.1*). The overall beam delivery time for 100 MU was examined for each setting of T_{cyc}. The efficiency of gated treatment delivery and the effective dose rate were determined for each T_{cyc} operation and compared to the ones with non-gated delivery.

3.2.4.3 Effect of the respiratory gating threshold level

One can define the duty cycle for respiratory-gated beam delivery by the ratio of patient breathing under a selected gate threshold to the entire duration of patient breathing during a beam delivery. This was computed from the RPM data for each patient when the gate threshold level was preset. Based on each patient's breathing data set, the simulation accounting for the starting phase effect was repeated for three different gate threshold levels set at the duty cycles of 10%, 20%, and 30% for each.

3.3 Results

With respect to non-respiratory gated beam delivery, from the results of simulation it took 1.11 min to deliver 100 MU. This resulted in an effective dose rate of 90.1 MU/min. These values were used as the reference for comparison with the 100 MU equivalent beam delivery time with respiratory gating for each T_{cyc}.

3.3.1 Effect of starting phase of beam delivery

Figure 3-5 shows a histogram of the time to deliver 100 MU with respiratory gating for a T_{cyc} of 2.7 s and a gate threshold level set for a 10% duty cycle (narrow gate window) simulated with 62 patient breathing data sets. This is one example that demonstrates the impact of starting phase on the result of beam delivery time analysis. The “0 shift” in the legend indicates simulation results calculated at an arbitrary patient breathing phase where this phase is regarded as the reference phase. Based on the reference phase, the same simulation was repeated for different phases. As seen from these graphs, the spread of the beam delivery time distribution increased as the effect of starting phase was taken into account. The maximum beam delivery time with respiratory gating for a T_{cyc} of 2,7 s was 23.2 min for a 10% duty cycle at the reference

phase of 0, the starting phase. However, by accounting for the effect of starting phase, the maximum beam delivery time was 43.6 min, nearly double the time for non-gating.

Similarly figure 3-6 and figure 3-7 illustrate the histograms of the 100 MU beam delivery time with respiratory gating for a T_{cyc} of 2.7 s and a gate threshold level set for 20% and 30% duty cycles. The greater the gate threshold level, the wider the gate window became. A comparison of figures 3-5 to figures 3-6 and 3-7 showed that the distribution of the beam delivery time in each histogram became more spread out with a decrease in the gate threshold level from the 30% to 10% duty cycle. Consequently, as the respiratory gate threshold level decreased, the average beam delivery time increased. In addition, the comparison revealed that any variation in the starting phase of beam delivery tends to have a greater influence on the beam delivery time for the lower respiratory gating threshold level (10% duty cycle), as compared to the higher threshold (20% and 30% duty cycle).

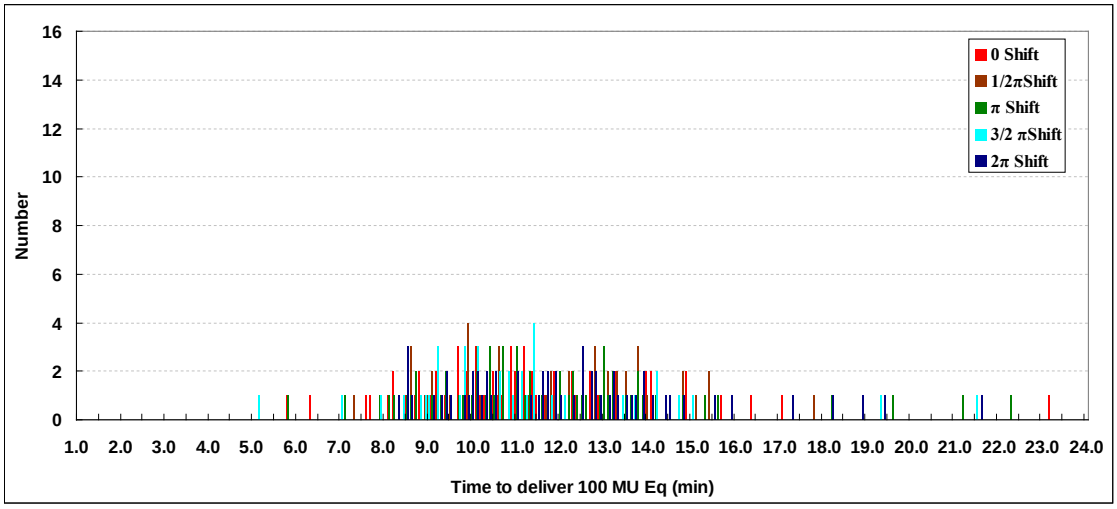

Figure 3- 5. Histogram of 100 MU delivery time with respiratory gating for a T_{cyc} of 2.7 s and the gate threshold level set at the 10% duty cycle. The simulation was performed for 62 patient breathing data sets at four different starting phases from 0 to 2π.

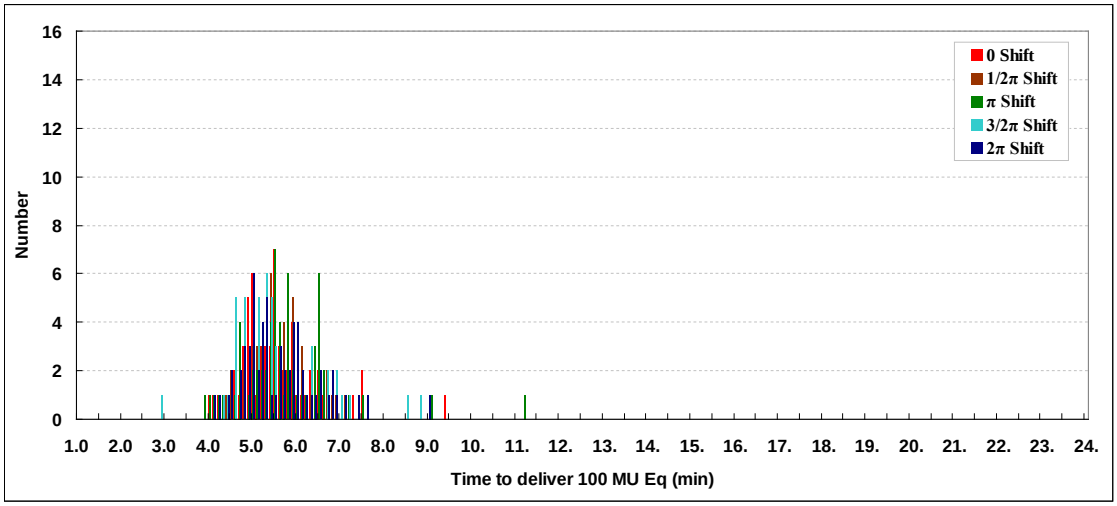

Figure 3- 6. Histogram of 100 MU delivery time with respiratory gating for a T_{cyc} of 2.7 s and the gate threshold level set at the 20% duty cycle.

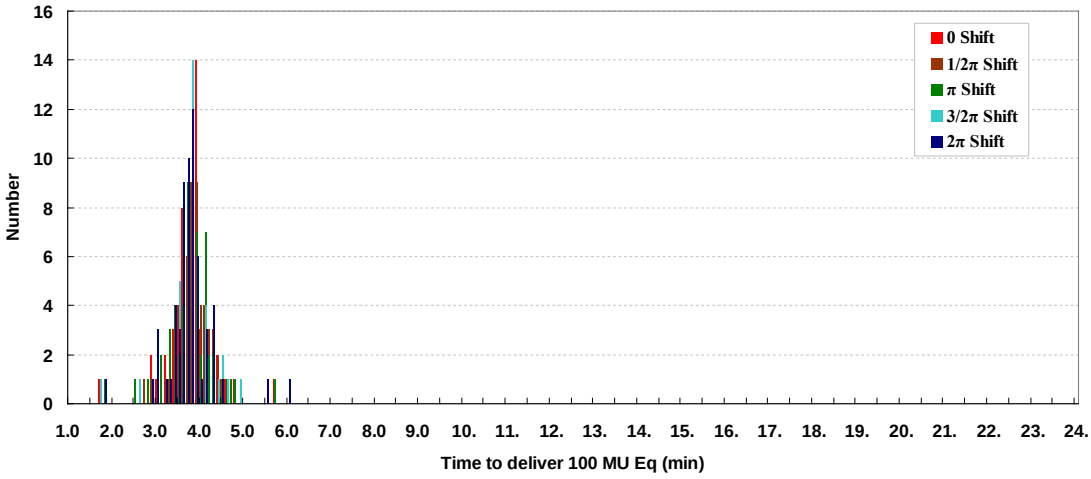

Figure 3- 7. Histogram of 100 MU delivery time with respiratory gating for a T_{cyc} of 2.7 s and the gate threshold level set at the 30% duty cycle.

3.3.2 Effect of T_{cyc} duration

Figure 3-8 summarized the overall simulation results of the 100 MU beam delivery time for each condition with non-gating and with respiratory gating for each T_{cyc} at each gate threshold level using 62 breathing data sets. Each bar in figure 3-8 represents the mean value of the distribution of beam delivery time simulation results including the starting phase effect for each T_{cyc} value and gate threshold level. Examples are shown in figures 3-5, 3-6 ad 3-7. The error bars represent the maximum and minimum values in the distribution of the 100 MU beam delivery time for each condition including the starting phase, which indicates the best and worst cases of the beam delivery time for each T_{cyc} and gate threshold level. The mean beam delivery time for respiratory gated beam delivery, as figure 3-8 shows, was two to ten times longer than the beam delivery time for non-gated mode, depending on the value of T_{cyc} as well as the respiratory gate threshold level. At a gate threshold level for the 10% duty cycle, the average time to deliver 100 MU gradually decreased until the value of T_{cyc} reached 5.0 s, and then leveled off when T_{cyc} values were greater than 5.0 s. For T_{cyc} was set to the average breathing cycle for each patient data set, the average beam delivery time exceeded that when T_{cyc} was 4.0 s or longer ($T_{cyc} \geq 4.0$ s). Furthermore, as seen in the width between the maximum and minimum beam delivery times, the beam delivery

times were widely distributed. This showed that the beam delivery time for patient breathing cycle specific T_{cyc} was strongly influenced by the starting phase and/or patient breathing type. For a variable T_{cyc}, the mean beam delivery time was indeed shorter than other T_{cyc}s and the beam delivery time was less sensitive to the starting phase and patient breathing type. Thereby the overall simulation results indicated that the variable T_{cyc} mode improved the efficiency of respiratory gated beam delivery independent of patient breathing and starting phase effect. Since T_{FT} in a variable T_{cyc} mode can be extended until a respiratory gate is yielded and the magnet excitation pattern can shift to the next T_{cyc} sequence immediately after previous deceleration sequence, the starting phase effect was mitigated. This led to the reduction in overall beam delivery time. One should note that the differences between the maximum and minimum beam delivery times with $T_{cyc} > 4.0$ sec were also comparable to variable T_{cyc}. These results were also considered from the efficiency point of view for each T_{cyc} and each gate threshold level. The efficiency is defined as the ratio of 100 MU to the beam delivery time, averaged over the simulation results using 62 patient breathing data sets for each T_{cyc} and gate threshold level. This is called the “effective dose rate”. The effective dose rate decreases compared with the effective dose rate in the non-gated case, which is the ideal efficiency. Therefore the effective dose rate

indicates how much the efficiency of beam delivery is decreased by respiratory gating compared with the non-gating case. The overall improvement in efficiency expressed by the effective dose rate, which shows mean values only, is shown in figure 3-9. The variable T_{cyc} operation offers 1/2 through 1/4 of efficiency compared with the non-gated beam delivery. This is the maximum efficiency regardless of the gate threshold level.

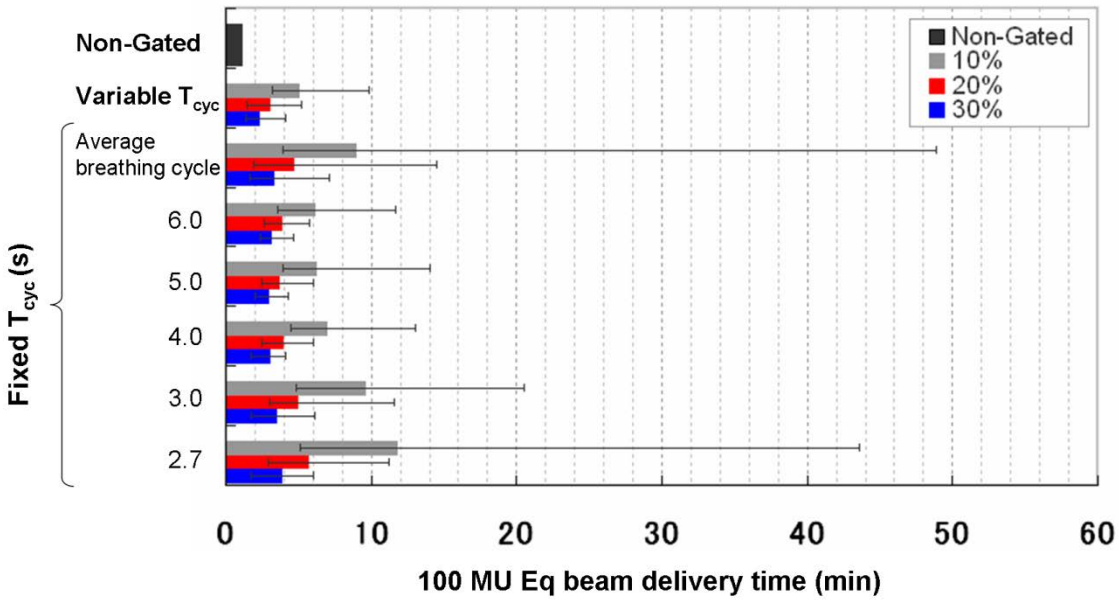

Figure 3- 8. Overall results of average times to deliver 100 MU over 62 patient breathing data sets for non-gated and respiratory-gated beam delivery for each T_{cyc} at each gate threshold level of 10%, 20% and 30% duty cycle, including the starting phase effect. The bars represent the average beam delivery time and the maximum and minimum beam delivery time are also shown as error bars for the distributions of each simulation condition for 62 patient breathing data sets.

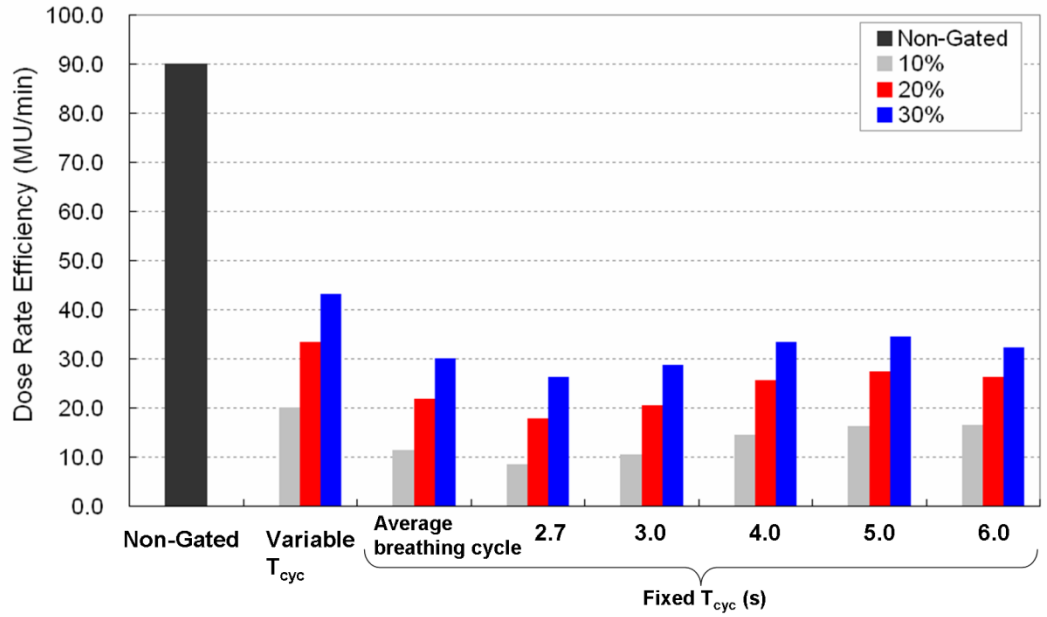

Figure 3- 9. Effective dose rate for respiratory-gated beam delivery with different values of T_{cyc} for each gate threshold level of duty cycle and effective dose rate for non-gated delivery (used as a reference). The effective dose rate is defined by 100 MU divided by the average beam delivery time for each T_{cyc} and gate threshold level obtained from figure 3-8.

3.3.3 Effect of respiratory gating threshold level

One can see from figures 3-8 and 3-9 that increasing the gate threshold level from a 10% duty cycle to a 30% duty cycle led to a decrease in the average beam delivery time, and this performed as well as increasing T_{cyc} did. At the lower gate threshold level setting, as the duration time of each respiratory gate signal decreased, the chance of signal matching between the respiratory gate signal and synchrotron flat-top phase became lower than the higher gate threshold level. As a result, the 100 MU beam delivery time with a lower gate threshold typically took longer than with a higher gate threshold, resulting in a lower effective dose rate. In addition to the lower gate threshold level, when the shortest T_{cyc} of 2.7 s was used, the effective dose rate represented the worst case result (figure 3-9). As shown in figure 3-8, the error bars became longer with the lower gate threshold level irrespective of any T_{cyc} pattern because the sensitivity to the starting phase increased with a decrease in the gate threshold level.

3.4 Discussion

One of the major approaches for active beam delivery to a moving target due to patient breathing is respiratory gated beam delivery. When the proton beams are delivered during specific phases of the target motion, the effective target motion is estimated to be small, which can reduce the internal target volume in treatment planning. This enables one to provide greater normal tissue sparing (Chang, 2006). It also permits dose escalation to tumors complexly surrounded by normal structures. However, respiratory gated proton beam delivery is still much less commonly discussed in the literature. The main objective of this chapter was to determine the optimal combination of parameters for efficient beam delivery with respiratory gating. In order to do this, a simulation study incorporating the synchrotron magnet excitation pattern, patient breathing data sets, gate threshold levels and beam delivery starting phase was performed.

First, the results of the simulation indicated that the average beam delivery time with respiratory gating increased by a factor of 2.0 to 3.4 times for the 30% gate threshold, 2.6 to 5.1 times for the 20% gate level and 4.3 -10.5 times for the 10% as compared to non-gated delivery. The beam delivery time varies for each gate threshold level depending on synchrotron operation with T_{cyc}. Secondly the simulation results

showed that the variable T_{cyc} operation has the greatest efficiency and lowest increase in beam delivery time for all gate threshold levels. For a 30% duty cycle gate threshold level, the effective dose rate was 45 MU/min for the variable T_{cyc} mode. However for other fixed T_{cyc} operations the highest efficiency was 35 MU/min. Thirdly the starting phase of beam delivery inherently had a considerable impact on the beam delivery time. This effect was clearly observed with short T_{cyc} operation (=2.7 s) as well as T_{cyc} set to the average patient breathing cycle. On the other hand, the variable T_{cyc} exhibited robustness against the starting phase and the use of a higher gate threshold level for all values of T_{cyc} also had less impact on the beam delivery time. The worst case of the beam starting effect was that, for T_{cyc} set to the average patient breathing cycle, the beam delivery time increased by a factor of 12 (between the minimum and maximum beam delivery times) due entirely to the change in the starting phase of beam delivery. Thus these are very important factors influencing the efficiency of respiratory gated beam delivery. As several studies have demonstrated, providing audio-visual biofeedback (George, 2006, Kini, 2003) to patients to assist in stabilizing their breathing and synchronizing with the synchrotron operation could be one solution to minimize the effect of such factors.

The patient breathing data set exported from the RPM system was indirectly obtained by monitoring the patient's chest or abdominal surface motion using a box placed on the patient. In most cases, it is well known that such an external surrogate cannot reflect accurate internal tumor motion (AAPM Report of Task Group 76, 2006). Tsunashima et al (2004) reported that the there are phase differences on the order of 0.0 ~0.3 s between external respiratory motion and internal tumor motion in the liver, esophagus and lung. Thus, if one were to evaluate gated beam delivery to the moving target from a dosimetric point of view, it might have been controversial to use the external surrogate based patient breathing information. However the objective of the simulation study is to estimate the beam delivery time. The important information used in the simulation study is time domain information. The simulation result would not be influenced by how the accuracy the external surrogate used would express the target location, the phase difference between external surrogate and the target motion, even if its amount is significant, has no impact on the beam delivery time as long as an external surrogate is used for the respiratory gating system.

The beam delivery time of respiratory gated beam delivery was estimated by simulation, and its efficiency was also discussed for the passively scattered proton delivery mode only in this study. Further study is also required to ensure respiratory

gated proton beam delivery in passive scattered mode from the accuracy point of view with the different T_{cyc} operations investigated in this study. A similar study for respiratory gated proton beam delivery for spot (pencil beam) scanning beams will be an important subject in the further development of proton therapy. It may offer further potential to improve dose conformity on the target and increase normal tissue sparing. This could facilitate dose escalation to tumors that are surrounded by critical normal tissues, which would not have been otherwise possible.

3.5 Conclusions

The simulation study demonstrated the feasibility of respiratory gated beam delivery of synchrotron-based pulsed proton irradiation with minimal increase in beam delivery time. The results in this study indicate that a variable T_{cyc} mode of operation offers the greatest efficiency and is impacted less by patient breathing and the beam starting phase effect for respiratory gated delivery of pulsed proton irradiation.

Chapter 4. Specific aim 1: Beam scanning

A study of efficiency of spot scanning beam delivery with respiratory gated proton beam delivery

4.1 Introduction

The purpose of this study is to perform a simulation study similar to that done for passive scattering mode in previous chapter in order to evaluate the efficiency of synchrotron-based respiratory gated beam delivery for spot scanning mode. The simulation program is modified for scanning beam operation mode where all accelerator operation parameters for scanning beam delivery mode were employed. In addition, since it is expected that the scanning beam delivery time depends on the scan volume, scan volume information was taken into account in this study. The simulations are based on various scanning treatment plans using real lung patient CT data. The treatment plan generates a scanning file including the scan position and its beam intensity for each scanning volume. The scan position pattern is run with a variety of patient breathing motion files in the simulation, and the beam delivery time and its efficiency under various respiratory gate levels are evaluated. The simulation results could be useful when considering the feasibility of respiratory-gated proton scanning treatment.

4.2 Methods and Materials

As already discussed in chapter 2, the synchrotron operation and the structure of a spill in spot scanning mode are different from those in passive scattering mode. Some of the synchrotron operation parameters employed for scanning mode play a very important role in the simulation study. First, the synchrotron operation for scanning mode is introduced in this section. Second, the patient breathing pattern and scanning plan used in the simulation study is explained, and finally the procedure for simulation and analysis is described.

4.2.1 Characteristics of synchrotron operation for spot scanning mode

As briefly mentioned in the introduction, the synchrotron magnetic excitation pattern runs in the variable T_{cyc} operation mode. This is currently the only mode available for scanning beams in Gantry 3 at PTCH. Furthermore, in previous chapter, the variable T_{cyc} mode was demonstrated to be the most efficient beam delivery operation for respiratory gating mode for passively scattered beams. Variable T_{cyc} operation is also less influenced by the starting phase of the beam delivery in terms of the patient breathing phase (discussed in chapter 3). Therefore the simulation study was performed only for the evaluation of the variable T_{cyc} operation with respiratory gating

in scanning beam operation. Since the synchrotron magnetic excitation pattern for scanning mode is somewhat different from passive scattering mode, the synchrotron operation and its parameters used in the simulation program for scanning mode are introduced in the following session.

4.2.1.1 Synchrotron operation pattern and parameters for simulation

The synchrotron magnet excitation pattern for scanning mode, as explained in the chapter 2, is quite complicated. The simulation program for this study simplified the synchrotron operation patterns with identical accuracy. Figure 4-1(a) shows the schematics of actual synchrotron magnet excitation operation in scanning mode. According to the specifications for synchrotron operation in scanning mode, the duration time from re-acceleration to the end of the next acceleration phase, $T'_{acc,n} + T'_{dce,n} + T_{acc,n+1}$, is a constant value regardless of energy. Therefore we have defined a new expression for the deceleration phase, $T'_{dec,n}$ for convenience as

$$T'_{dec,n} \equiv T'_{acc,n} + T_{dec,n}$$

And therefore,

$T'_{dec,n}+T_{acc,n+1} \approx 2.1$ sec (constant)

by which the simplified accelerator operation pattern is also regarded as the classic acceleration pattern used in the passive scattering mode represented in figure 4-1(b). In addition, it is possible to replace the summed value of $T'_{dec,\,n}+T_{acc,\,n+1}$ with a constant value, 2.1 sec. This enables one to simplify the accelerator operation pattern in our simulation study so that the acceleration pattern is expressed as the classical accelerator patterns. However it should be noted that, since there is a difference between $T'_{dec,n}$, and $T_{dec,n}$, the $T'_{dec,n}$ is used in our simulation.

Regarding other parameters required for the simulation, there is a 180 ms delay time from beam-on (extraction) ready signal to actual beam irradiation in the variable T_{cyc} mode. The synchrotron with the variable Tcyc mode has a function of dynamically changing the flat top phase to wait for the signal coming from the respiratory gating system. The available waiting duration time ranges from 0 ~ 200 ms. The spill length, T_{sp}, ranges from 0 ~ 5000 ms but the effective spill length is the number subtracted from the available waiting time. If all the spot beams are delivered on a given scan layer while the respiratory gate is on and the synchrotron is in ready

status or in the case that a respiratory gate signal turns off while the beam is being delivered (the synchrotron ready status), the deceleration phase is forced to start as soon as the spot being delivered at the moment has been completed. The mechanical delay time of the transition to deceleration phase is consequently the last spot delivery time at each spill. There may be an uncertainty arising in beam delivery measurement. However this can be ignored when accounting for the spot delivery time, as discussed in the next chapter.

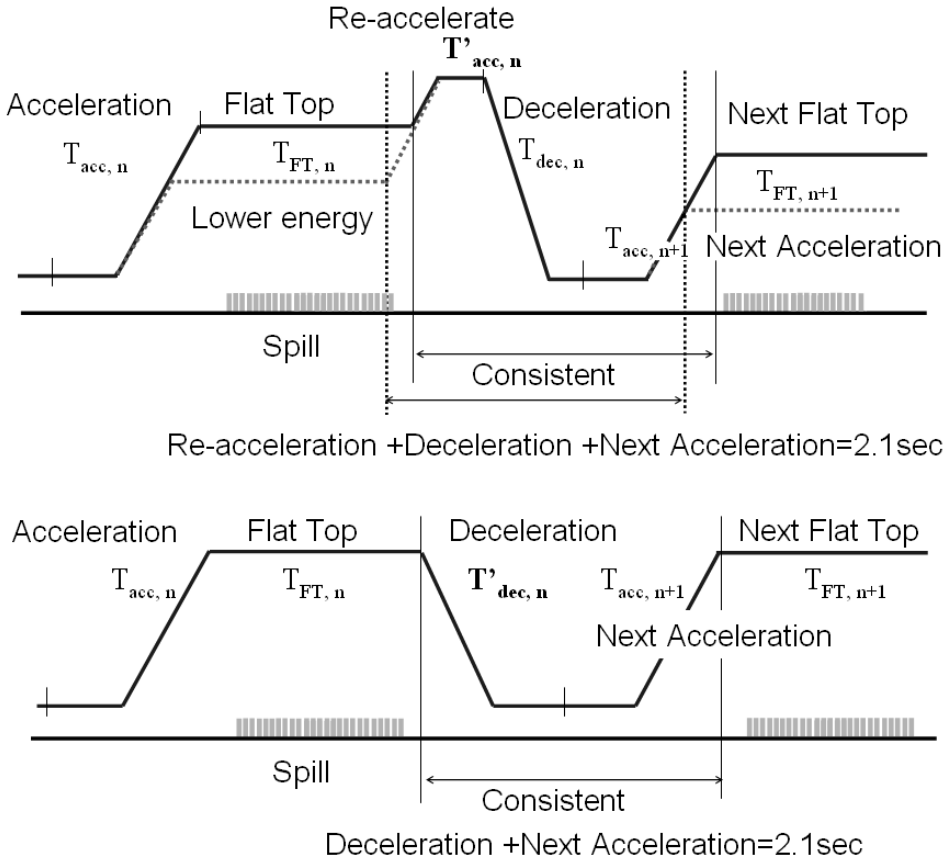

Figure 4- 1. Illustration of synchrotron magnet excitation pattern. The solid line expresses the higher energy acceleration pattern and the dashed line represents the lower energy acceleration pattern.

4.2.1.2 Spot scanning beam delivery

The coordinate system of the scanning data is that the y-axis is defined as the patient longitudinal direction and x is perpendicular to the y axis, which is not always the patient lateral direction because the direction changes with gantry angle. The scanning beam delivery time consists of two parts: shooting one spot beam and moving on to the next spot position. The former takes approximately 4 ms to produce the maximum spot dose. The spot position transition time is parameterized with the distance from one point ($x_{s,i}$, $y_{s,i}$) to next position (x_{i+1},y_{i+1}) and the beam energy. Currently the minimum spot spacing is set to 4 mm for each direction and the spot transition takes approximately 3.2 ms to move to 4 mm distance in each direction. Table 4-1 shows experimental data for spot transition time for the x- and y-directions for a proton energy of 219.3 MeV.

The spot position transition time is different in the x- and y-directions for each. It also varies depending on spot spacing (dx, dy in distance) and spot energy (*E*). The spot transition time for each condition is interpolated from the data in table 1. There are two sets of formulas for computing the spot transition time for each direction:

When dx > 0.4 cm and dy < 2.0 cm,

$$t_x = \frac{5.3 - 3.2}{2.0 - 0.4} \frac{1}{\sqrt{E^2 + E_p E}} \sqrt{219.3^2 + E_p * 219.3} * dx + b$$

$$t_y = \frac{3.7 - 3.2}{2.0 - 0.4} \frac{1}{\sqrt{E^2 + E_p E}} \sqrt{219.3^2 + E_p * 219.3} * dy + b$$

When dx > 2.0 cm and dy < 30.0 cm,

$$t_x = \frac{33.6 - 5.3}{30 - 2} \frac{1}{\sqrt{E^2 + E_p E}} \sqrt{219.3^2 + E_p * 219.3} * dx + b$$

$$t_y = \frac{17.0 - 3.7}{30 - 2} \frac{1}{\sqrt{E^2 + E_p E}} \sqrt{219.3^2 + E_p * 219.3} * dy + b$$

where

b: variable depending on *E*

E_p: rest energy of a proton (=938.3MeV)

When the spot moves to an oblique position, the spot transition occurs in the x- and y-directions simultaneously; therefore the total transition time, T, takes the maximum value from either,

$T_{spot}=\max(t_x, t_y)$

and T_{spot} is calculated for every spot in the simulation.

The spot information used in the simulation includes the spot position (x- and y-direction on the beams eye view plane) and scan energy (layer) and beam weight. These are included in the spot file exported from treatment planning system used clinically (Eclipse, Varian®). Although the spot size and dose, with ranges 0.04 ~ 0.005 MU, may be very important to configure the patient dose distribution and evaluate the dosimetric impact, the geometrical size of the spot beam was not used and does not influence the beam delivery time. It was therefore not discussed in this study.

Distance [cm]	Transition Time [ms]	
	x	Y
0.4	3.2	3.2
2	5.3	3.7
30	33.6	17.0

Table 4- 1. Experimental data the spot transition time for a proton energy of 219.3 MeV.

4.2.2 Spot scanning plan file

The DICOMRT file includes a scan plan including the number of control points (CPs), spot position, spot weighting and spot energy for each CP. The scan plan file for each treatment session is connected to the beam delivery time because the beam delivery time is in principle governed by the number of spots. Some spot locations are duplicated, which indicates a re-scanning process, meaning that rescanning is performed following the original scan. Rescanning is currently required because the maximum dose per spot is limited to 0.04 MU/spot. If more dose is needed at a given position, repainting is needed. The total number of the spots is a very important factor in the beam delivery time estimation because if the number of spots is too great, the spot beam delivery of one CP would be unable to be done within the maximum T_{cyc}, which would cause the next beam delivery sequence to commence after waiting for the $T_{dec}+T_{acc}$ =2.1 s interval. Each layer is additionally parameterized by depth (or effectively associated with a specific proton energy). When changing the scan layer, the synchrotron needs to take a sequence of declaration and acceleration. The sequence of energy change would be potentially a main cause of time consumption in beam delivery. It is associated with the number of CPs, and also the number CPs is determined by the target shape in a given beam direction. The scanning beam delivery

simulation is should be applied to many kinds of target volumes and shapes even in same volume of targets.

4.2.3 Scan target volume

In this simulation study, the scanning beam delivery run following the scan pattern files were made from intensity modulated proton therapy plans. The scan target volumes were made based on the planning target volumes for each treatment plan. The 10 IMPT treatment plans including 38 sessions (beam angles) were used for the simulation. Table 4-2 summarizes the scan target volume. Scan target volumes for each patient were calculated from the scan position files. These plans were made using Eclipse version (8.1.8 Varian®) for research purposes (Zhang X, 2010). The target volumes accounted for target motion using a 4DCT data set; in other words, since the target volumes were made based on the average CT data set (Underberg R W M, 2005), the scan volumes were consequently different from the true target volume that would be used in respiratory gating mode. Although these plans were not originally created for the respiratory gating beam delivery, it is would not be a concern because the aim of this study was focused on investigating the relationship between the variety of scan target volumes and beam delivery time. For this reason, the simulation study needed as

many types of scan target volumes as possible for measuring the scanning beam delivery time. Further, because the optimization process in the treatment planning system does not include a factor accounting for either motion uncertainty or the respiratory gating, it does not also matter what kind of scan target we use.

	Scan volume information		
	Median	minimum	maximum
Volume [cm^3]	315.4	85.5	932.9
Number of layers	55	46	150
Number of Spots	2189	272	5748

Table 4- 2. Statistics of the scanning target volumes used in the scanning beam simulation study. The data includes 38 different beam angles for 10 patient plans.

4.2.4 Respiratory motion data sets

The Real-Time Position Management (RPM) respiratory gating system (Varian Medical Systems, Palo Alto, CA) was used in this study. The RPM system tracks the displacement of a patient's external morphological features and records displacement and phase data for patient breathing at the rate of 30 data points per second. The synchrotron operation parameters and spot delivery time are recorded in ms order in the program, thus the RPM data were also converted into ms order through interpolation. Ten free-breathing data sets acquired when patients had been previously enrolled in treatment for lung cancer were used for the simulation.

4.2.5 Respiratory gating simulation program

Figure 4-3 shows the in-house simulation software interface that enables virtual simulation on the scanning treatment with or without the respiratory gating (selectable). It can import a scanning treatment plan output made from Eclipse DICOMRT file (Varian), which includes scan positions, scan energies, and spot weights for each scan layer, which is the control point (CP) for each treatment session distinguished by gantry angle. The software can also import patient breathing trace data exported from RPM in respiratory gating simulation mode, and we can arbitrarily set the respiratory

gate threshold level. As the simulation begins, the patient breathing data read from the patient breathing file and the synchrotron magnetic excitation pattern with the variable T_{cyc} mode run simultaneously. When the respiratory gate is on and the synchrotron is in flattop phase, ready for beam delivery, the spot beam delivery starts following the scan plan created with Eclipse. The scan beam delivery is finished when the spot beam has been delivered to all scanning positions. The simulation interface expresses the signal interaction between patient breathing and synchrotron and beam delivery operations as if we are looking at signal outputs on an oscilloscope.

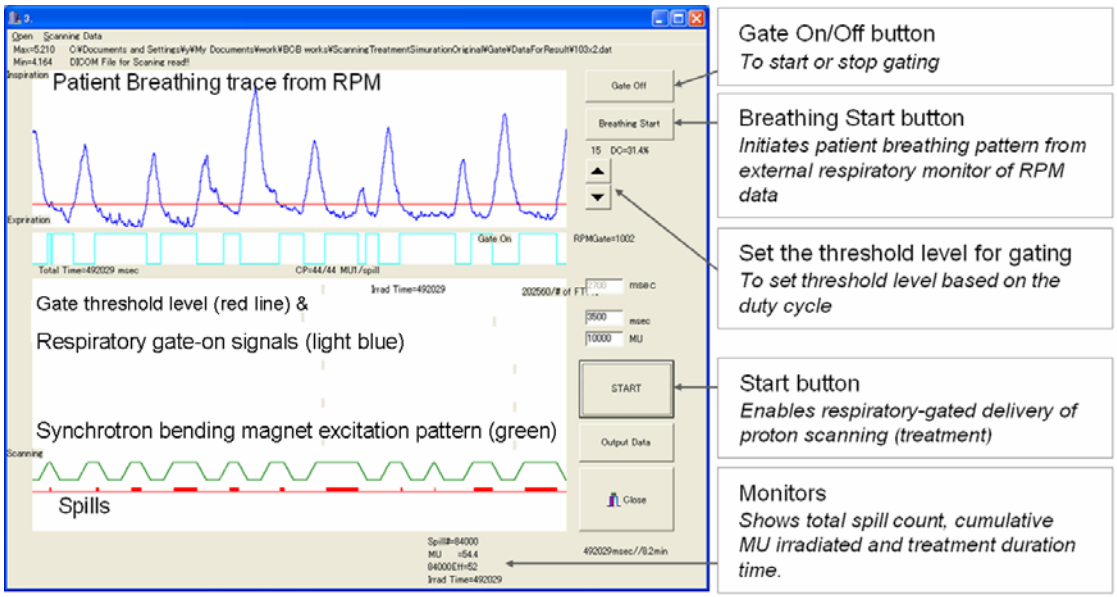

Figure 4- 2. Screenshot of the in-house simulation software interface for respiratory gated scanning beam delivery. It enables the user to import a spot file exported from treatment planning (Eclipse Varian ®) and a patient breathing data set from RPM (Varian ®). The user can select the respiration gate threshold level for each simulation.

4.2.6 Simulation study

The simulation was performed using the software described above. From the simulation results the beam delivery time was analyzed and the variation efficiency of scanning beam delivery due to the interaction between scanning plans and patient breathing patterns was observed, and the results were compared to those for the non-respiratory gated scanning technique.

4.2.7 Simulation of scanning beam delivery time and analysis

The imported patient breathing data sets and the synchrotron magnet excitation patterns were run on the software at the same time, and respiration gate signal was also simultaneously generated based on a preset gate threshold level. When the signal matching between the respiratory gate signal and the flat-top phase of synchrotron magnet excitation pattern occurs, the spot beam is delivered following the order specified in the CP file. The simulation software measured the beam delivery times for each control point file. This comprised one session of simulation to measure the beam delivery time for each CP file (each treatment field) with one breathing data set and a certain gate threshold level. This was repeated for different breathing data sets and gate threshold levels and estimated the overall beam delivery time of respiratory gated spot

beam delivery for each treatment field (each CP file). The treatment efficiency and effective dose rate were also calculated.

The efficiency of the passive scattering beam delivery mode discussed in the previous chapter was evaluated with 100 MU equivalent beam delivery as a reference for measuring the dose delivery time. It followed the beam delivery control system for the passive scattering mode. As the delivered dose met the preset dose of 100 MU, the beam delivery for each treatment session (at each gantry angle) was completed and also defined as an end of the given treatment session. The completion of beam delivery for scanning mode is quite different from passive scattering mode, however. The completion of beam delivery is recognized in the control system when the scan pattern following a scan file (DICOMRT exported from Eclipse) is completed. Thus, it does not use a certain preset dose as the main beam delivery control parameter. Therefore, in the scanning simulation study, the beam delivery times obtained from each simulation were not based on a consistent number of MUs, and thus it is not as easy to compare the dose delivery times for the scanning mode as for the passive scattering mode. This is why we mainly focused on the relationship between the effective dose rate and target volume or shape for the comparison of efficiencies.

4.2.8 Starting phase effect

The synchrotron-based proton beam, that is spill, has a pulsed beam which is neither a continuous beam or always available to be delivered. Therefore the proton spill is yielded only when the respiratory gate signal is turned on during the flat-top phase in the synchrotron magnet excitation pattern. For this reason, in chapter 3, the effect of the starting phase had a significant impact on the beam delivery time in accordance with the choice of T_{cyc}. In spot scanning mode, the variable T_{cyc} mode is employed, and is most efficient operation, being robust against to the effect of starting. Concerning variable T_{cyc} operation, its unique advantage is that the synchrotron can wait for the respiratory gate signal coming for 5.0 s at maximum. It was demonstrated in the previous chapter that the starting phase effect is effectively reduced when using the variable T_{cyc} operation, and the error that arose in the results of the beam delivery time were caused by the variations in patient breathing patterns rather than the starting phase. Therefore the simulation study did not take the starting phase effect into account. The focus in this study was on the variability of scan beam delivery caused by variability of the patient breathing pattern and the scan target volumes and shapes.

4.2.9 Effect of respiratory gate threshold level

Respiratory gating was applied in exhale phase under regular patient breathing conditions. From each set of patient breathing data, the simulation for respiratory gating beam delivery to each treatment field (scan volume) was repeated for three exhalation threshold levels of 10%, 20%, and 30% duty cycles.

4.3 Results

The scan beam delivery times were calculated from simulation. First the relationship between the time to the cover the target volume with the scanning beam, the number of spots and the number of control points (scan layers) was investigated. Secondly the efficiency analysis using MU was discussed.

4.3.1 Scanning beam delivery time

Figure 4-3 shows the relationship between the scanning beam delivery time with respiratory gating and the number of the layers (control point, figure 4-3 (a)), the number of spots (figure 4-3 (b)) and the scan target volume (figure 4-3 (c)). The results of simulation for the beam delivery time without respiratory gating were also shown in the graphs for comparison. Each plot represents the averaged values from one session

running with 10 patient breathing data sets. The graphs showed that the scanning beam delivery time with respiratory gating is dependent on the scan volume and the number of layers, and the relation depended consistently on the gate threshold. The worst case was approximately 36 min needed for beam delivery to a 906.2 cm^3 volume with a 10% duty cycle. For the beam delivery times with 30% and 20% duty cycles, these became 2.4 and 3.6 times longer on average than the reference beam delivery time without gating. On the other hand, the beam delivery time with a 10 % duty cycle gate level was 9.0 times longer on average than the reference, and the delivery times varied significantly with the scan volume compared with those with 30% and 20% duty cycles.

Figure 4-3 (d) shows a summery of the correlation coefficients between the beam delivery time and factors in each graph for each gate threshold level. Comparing these, the beam delivery time had stronger relationship with the number of the control points and spots than the scan volume. Without gated scanning beam delivery, the number of control points has much stronger correlation with the beam delivery time than other two factors, which indicated that the beam delivery time was governed by the number of control points. For the respiratory gating mode, the beam delivery time was governed by the number of spots when the gate threshold level was high; however as

the gate level was lowered, the beam delivery time become much more correlated with the number of control potions.

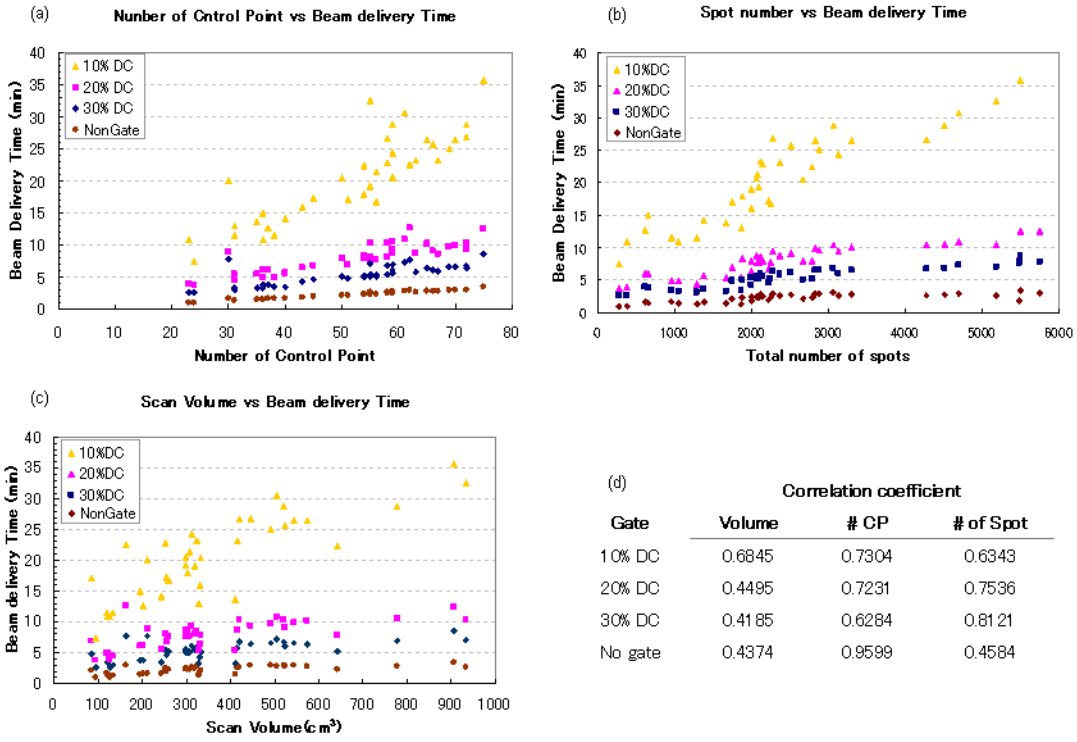

(d)

Correlation coefficient

Gate	Volume	# CP	# of Spot
10% DC	0.6845	0.7304	0.6343
20% DC	0.4495	0.7231	0.7536
30% DC	0.4185	0.6284	0.8121
No gate	0.4374	0.9599	0.4584

Figure 4- 3. Scanning beam delivery time vs. target volume, number of control points and number of spots to be delivered.

4.3.2 Effective dose rate (MU/min) analysis

The beam delivery time theoretically increases with the size of scanning volume and its delivered dose. Therefore the simulation results need to be normalized with either of them for comparison. Figure 4-4(a) shows the relationship between the effective dose rate (MU/min) and the scan volume. The effective MU/min was calculated by the prescribed dose in MU divided by the beam delivery time. The results of the graph indicated that there was no significant difference in the effective MU/min over the scan volumes. As shown in figure 4-3 (c), the correlation between the scan beam delivery time and volume is weaker than the scan volume and CP. Figure 4-4 (a) also showed that the efficiency of respiratory gated beam delivery expressed with the effective MU was consistent. It was clearly seen in figure 4-4(b), which represents the histogram of the effective MU/min shown in figure 4-3(a). The average effective dose rate was 34.2±18.8 (MU/min) for the non-gated scanning beam delivery where the spot position scan patterns were run without respiratory gating. Ideally, the beam efficiency would be as close to this value as possible for scanning beam delivery treatment with respiratory gating. With gating, the effective MU/min was however reduced to 13.0±3.4, 8.6±2.2 and 3.3±0.7 MU/min for 30%, 20% and 10% duty cycles respectively. The beam efficiency dropped down to 2.3 ~ 10.3 times with respiratory

gating. The graph also showed that as the gate level was lowered (a narrow gate window), the standard deviations of the effective MU/min for each gate level decreased. The effective MU/min seemed to become independent of the scan plan and patient breathing and converged to a certain value.

(a)

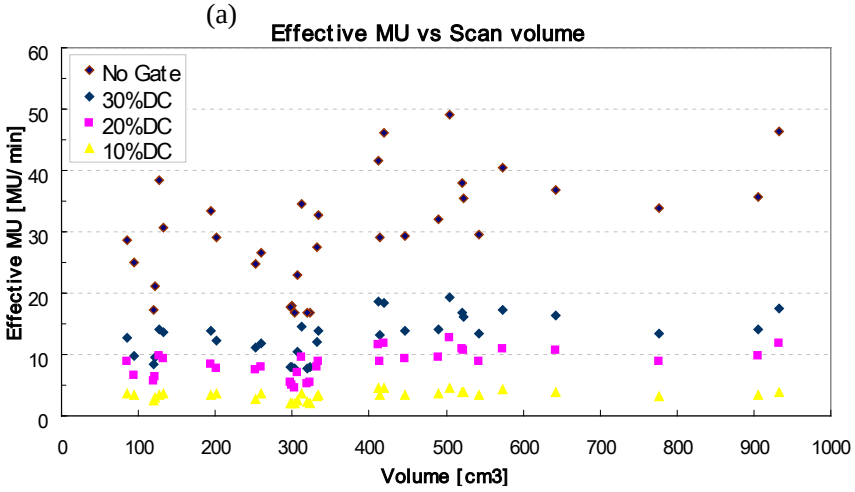

(b)

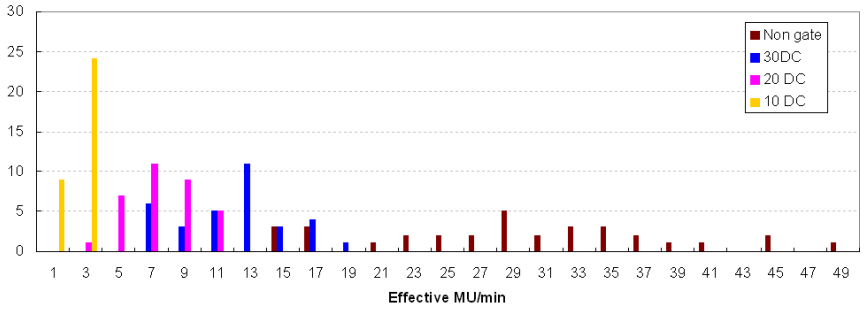

(c)Effective MU/min

Gate level	Mean	SD
10% DC	3.3	0.7
20% DC	8.6	2.2
30% DC	13.0	3.4
No gate	30.4	9.1

Figure 4- 4. Result of the effective MU/min for 10 scanning plans (total beam 33 angles).

4.4 **Discussion**

The results of simulation showed that the beam delivery time with the respiratory gating was more dependent on the number of control points (CPs) than the scan volume. The efficiency decreased 2.3 ~ 10.3 times compared to non-gating beam delivery.

For scanning beam delivery without respiratory gating, in most case, all spots of an identical scan energy layer are delivered within one cycle of synchrotron operation T_{cyc} as long as the spill length, T_{spill}, does not exceed the maximum duration time of 5.0 s. This is an ideal situation and the best efficiency case scenario for scanning beam delivery. In this case, according to the simulation results, only approximately 30% in the entire beam delivery time for each session is spent for actual beam delivery, that is calculated by integration of all values of T_{spill}. The remaining 70% was spent for the acceleration and deceleration of the synchrotron, the sum of which is $T_{acc}+T_{dec}=2.1$ s for each session. As the number of CPs increases, the number of $T_{acc}+T_{dec}=2.1$ s cycles consequently increases because, when the energy layer is changed corresponding to the changing CP, the synchrotron needs to have deceleration and acceleration phase every single time. Since the time for scanning beam delivery without gating is mainly spent for energy changes ($T_{acc}+T_{dec}=2.1$), as shown in

figure4-3(d) the beam delivery time has of course good correlation with the number of CPs. The number of CP has low correlation with the target volume. For example, assuming that a scan plan is made for a given target with an oval shape, the number of CPs made in the longitudinal direction is greater than the one made in the direction perpendicular to the original one. The difference in the number of CPs is connected to the number of acceleration and deceleration phases (2.1 s), which consequently has a great effects on the beam delivery time even for the same target volume. This is not taken into account in the relationship between the scan volume and the beam delivery time.

This explains the poor correlation seen in figure 4-4(c). The time consumption for energy change may be a synchrotron-specific issue. As discussed in the literature, it is in principal not a big issue for one type of cyclotron (Pedroni, 1995); however, a somewhat there is a similar issue associated with machine specification was reported for another type of cyclotron in which energy changes were reported to require 2~ 10 s (Paganetti, 2005 and Lu, 2007).

On the other hand, for beam delivery time with respiratory gating, the total beam delivery time becomes longer depending on the gate threshold. The main reason is the mismatch between the respiratory gate-on status and the flattop phase. When

such a mismatch occurs, the beam is not delivered and which is time wasting while the synchrotron is waiting for the respiratory gate signal to be on, but when it is not on, the synchrotron is forced to decelerate and move to next acceleration. This considerably affects the beam delivery time and efficiency. The total spill is basically nearly consistent whether the respiratory gate is used or not. The time consumption due to energy change, which was main cause of the beam delivery without gating, was still the main contribution to the beam delivery time with respect to 30% duty cycle. It was 5 times the value of T_{spill} and to the other major contribution due to gate signal mismatching was 2.3 times T_{spill} in the total beam delivery time. However, for the beam delivery for a 20% duty cycle, these ratios were 5.6 and 5.3 times T_{spill} for each, and finally 7.9 and 11.1 times T_{spill} for a 10% duty cycle. The contribution to the time consumption due to sum of T_{acc}+T_{dec} increased for low gate thresholds because the width of each respiratory gate signal is narrower, limiting the time for beam delivery and requiring the next T_{acc}+T_{dec} sequence to complete the remaining beam delivery. Therefore there is a greater number of spills needed to complete the same beam delivery. For this reason the correlation between the number of CPs and beam delivery time improved. However, the time consumption due to the signal mismatch had a greater impact on the beam delivery time than the time consumption of T_{acc}+T_{dec}

repetition for the lower gate threshold level. As mentioned above, the signal mismatch had significantly less impact on beam delivery for 30% duty cycle (5 to 2.3 compared to T_{spill}); however, this becomes nearly equivalent for a 20% duty cycle, and for a 10% duty cycle signal mismatch becomes the main reason for time consumption over the T_{acc}+T_{dec} repetition (7.9 to 11.1).

As shown in figure 4-4(b), the effective MUs without gating beam delivery were naturally higher and diverging for each scan plan compared to the case with respiratory gating. The effective MU/mins obtained without gating are strongly depending on each scan plan including the number of CPs and the prescribed dose (MU) for each plan. This is why the effective MU/mins were diverging. On the other hand, for the effective MU/min with gating, there is another factor to limit the spill length, which is the gate signal from respiratory gating system. For a lower gate threshold level, the width of the respiratory gate signal (duration time) becomes short and nearly consistent every gate signal regardless of the patient breathing pattern. For example, the average duration times of respiratory gate signal over the 10 patient breathing traces used in this study were 1.2±0.5, 0.8±0.3 and 0.5±0.2 s for the 30%, 20% and 10% duty cycle gate thresholds, respectively. This shows that the number of deliverable spots, that is spill time, are very limited by these numbers, and the spill

time consequently becomes nearly independent of the patient breathing pattern. However, it should be noted that the lower gate threshold takes very long time to deliver all spots shown in figure 4-3.

As a comparison, the effective MU/min for respiratory gated beam delivery in passive scattering mode obtained similarly in previous chapter were 43.5 MU/min, 33.3 MU/min and 20.0 MU/min for 30%, 20% and 10% duty cycles, respectively. Strictly speaking, it is difficult to compare the effective MU/min between the passive and scanning beam delivery with respiratory gating because the basic concept of beam delivery is quite different. However, the differences in the numbers have important meanings and may be very helpful to estimate the treatment time for respiratory gated scanning beam delivery.

4.5 Conclusions

Delivery of pulsed scanning beam proton therapy with respiratory gating is less efficient than passively-scattered proton irradiation. The results of this study quantified the reduction in efficiency for respiratory-gated scanning beam delivery. It is certainly true that a lower gate threshold greatly increases the beam delivery time. However, these results suggest very important information when making a decision of what gate level would be reasonable considering the balance between dosimetric quality and efficiency.

Chapter 5. Specific aim 2: Passive scattering mode

Assess the accuracy of dose delivery in respiratory-gated proton therapy in passively scattered beam delivery

5.1 Introduction

A spill in synchrotron-based respiratory gated delivery can be delivered only when the respiratory gating system turns on the gate signal during the flat-top phase of the synchrotron. A mismatch between the respiratory gate-on signal and the flat-top phase can worsen the efficiency in respiratory-gated proton delivery. The impact on the efficiencies due to the synchrotron operation cycle, T_{cyc}, have been investigated in specific aim 1: passive scattering mode (Tsunashima 2008). In addition to the inefficiencies, especially for the passively scattered beam delivery mode, the pulse length of the spill is currently fixed at 0.5 s/spill. If the duration time of a breathing phase under the gate threshold and ready for the gate-on is longer than the spill length, the spill is delivered at some time during the gate-on phase with the respiratory gating system. This is a stochastic event where the spill is almost randomly delivered within the patient breathing phase under the threshold level.

In accordance with this, it is hypothesized that because proton beams extracted from a synchrotron are pulsed-proton beams the quality of proton beam delivery to the moving target with respiratory gating has an uncertainty pulse-by-pulse. Such uncertainties could be dependent on the synchrotron operation cycles, T_{cyc}, discussed in chapter 3. However, as already stated in chapter 3, the feasibility of the respiratory gated beam delivery from the quality point of view has not been studied in detail. Therefore, the purpose of specific aim 2 is to quantify and evaluate the uncertainties of the synchrotron-based respiratory gated proton beam delivery.

This chapter focuses on the passive scattering technique and the investigation of the uncertainty of beam delivery with respiratory gating from the viewpoint of the patient's breathing signal. The simulations developed in specific aim 1 were extended to analyze the precision of respiratory gated proton beam delivery for different gate threshold levels and synchrotron T_{cyc} durations using different types of patient breathing patterns.

5.2 Methods and Materials

In specific aim 1, in-house simulation software for respiratory gating was developed to estimate the *efficiency* of respiratory gated proton delivery (Tsunashima *et al* 2008). In order to examine the *precision* of respiratory gated proton delivery the software used in chapter 3 has been modified to record the beam delivery in the time domain.

5.2.1 Synchrotron operation patterns and patient breathing data sets

The synchrotron magnet excitation patterns of the PROBEAT proton beam system with fixed and variable T_{cyc} operations were discussed in chapters 2 and 3. The simulation was implemented for three different synchrotron magnet excitation operations with T_{cyc}s. First, T_{cyc} was fixed to 2.7 – 4.0 s with which the T_{cyc} is too short to synchronize with the respiratory gate signal (figure 5-1(a)). Secondly T_{cyc} was fixed conversely too long (5.0 -6.0 s,), with which the synchrotron can synchronize with the respiration gate; however, once beam has been delivered, it is forced to spend a long wait time for completion of T_{cyc} operation. This leads to diminished efficiency (figure 5-1(b)). Thirdly the variable T_{cyc} (figure 5-3(a)) has the most efficient operation pattern. Further details on the variable T_{cyc} were discussed in chapter 3, specific aim 1. The simulation with different types of T_{cyc} synchrotron operations was performed for 100

MU beam delivery, different gate threshold levels and 70 breathing data sets exported from RPM (Varian Medical Systems, Palo Alto, CA). The details of T_{cyc}, gate threshold levels and other conditions used in the simulation were described in the previous chapter.

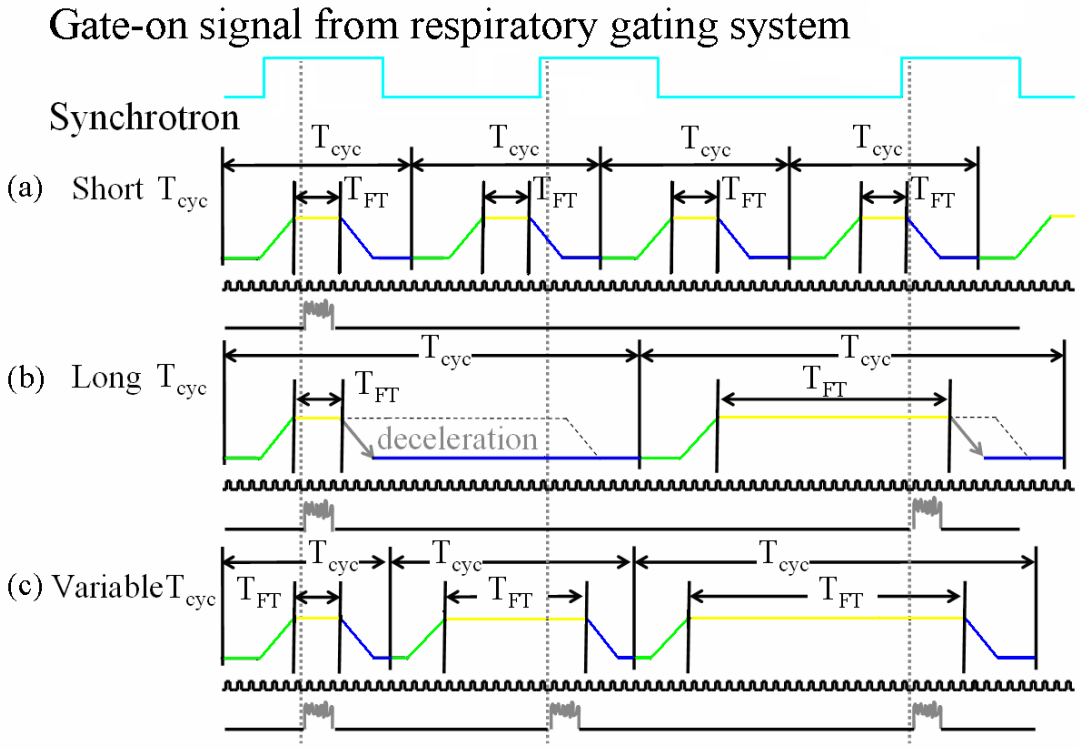

Figure 5- 1. Examples of beam delivery for fixed T_{cyc} having (a) short (T_{cyc}=2.7 s) and (b) long (T_{cyc}=5.0 s) operation and (c) variable T_{cyc} operation.

5.2.2 The precision of respiratory gated proton delivery

Figure 5-2 (a) shows an example of the simulation result. The RPM amplitude information, synchrotron magnet pattern and spill delivery were expressed in time domain (*t*). Each spill delivery was represented on the bottom of the graph and simultaneously these points were superimposed on the breathing trace (the blanked boxes plotted in figure 5-2(a)). For data analysis, each beam delivery point was assigned to each corresponding amplitude, x_k *(k=0,1,2….)*, of a random variable *X* with probability P($X=x_k$). This subsequently represented the probability density function (PDF) of the beam delivery points for respiratory gated beam delivery (figure 5-2 (b), (c)). For figure 5-2 (b), since the random variable *X* originally represented the patient breathing signal from the RPM system in the amplitude domain, the PDF, denoted by P(*X*), represented when or on which amplitude based patient breathing trace the spills were most probably delivered with respiratory gating. With respiratory gating, all beam delivery points obtained from the simulations, x_k, were distributed under the gate threshold level. Thus, the PDF of the beam delivery points were expressed by the probability distribution $f(x_k)$ (figure 5-2 (c)):

$$P(X = x_k) = f(x_k) \qquad (k = 0,1,2.....) \tag{1}$$

$$x_{k=0} = x_{GateThreshold}$$

At first the PDF of all the data points of the breathing trace under the gating threshold level was calculated. This represents the overall residual position uncertainty during the respiratory gated beam delivery. Assuming an accelerator provides a direct current beam delivery such as a cyclotron, the residual position uncertainty could represent the residual motions during the direct current beam delivery. This is useful as a reference when comparing synchrotron-based respiratory gating to cyclotron-based respiratory gating. Figure 5-2 (d) is the result of summing each plot from the gate threshold level, $x_{GateThreshold}$, on the PDF. This is defined as cumulative distribution function (CDF), denoted by $\Phi(x)$, which was expressed as follows:

$$\Phi(x) = P(X \le x) = \sum_{k=0}^{i} f(x_k) \qquad (2)$$

$$x_{k=i} = x$$

and this process was used to determine a metric to calculate the uncertainty of respiratory gated proton delivery. In figure 5-2(d) there is a point, denoted by ***x'***, set on the CDF at which approximately 95% of the total number of beam delivery points have been reached.

This is expressed by the following formula:

$$CDF_{95} = \Phi(x') = P(X < x') \quad (3)$$

$$R_{95} = x' - x_{GateThreshold}$$

Here the relative distance from the gate threshold to *x'* is defined as R_{95}. The R_{95} is a variable depending on the T_{cyc} operation, respiratory gate threshold level and starting phase of beam delivery. In order to take these into account, one session of a simulation was performed for several conditions with these parameters, and each simulation was repeated using 70 breathing data sets. From the simulation results the CDF and R_{95} for each condition were statistically analyzed.

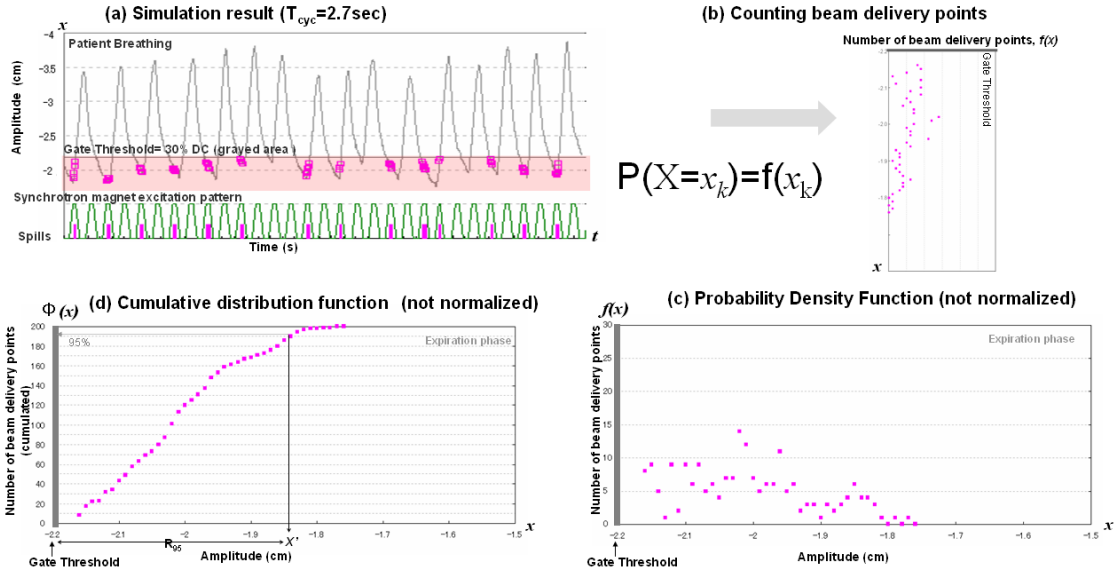

Figure 5- 2. Procedure to create the PDF and CDF from the simulation result. (a) is the simulation result for T_{cyc}=2.7 s and a 30% DC as the gate threshold level. The spill delivery was expressed with unfilled square symbols plotted on the breathing trace below the gate threshold level (shadowed area in (a)). (b) and (c) show the probability density function of the symbols (PDF). (d) shows the cumulative density function (CDF) calculated by summing each plot from (c).

R_{95} represents the most probable phase of spill delivery from the viewpoint of the patient breathing trace. For example, if R_{95} is very close to the gate threshold ($R_{95}\approx 0$), it means that most of the spills are probably delivered just after the breathing trace drops below the gate threshold rather than in the true end-expiration phase. Conversely, if R_{95} is farther from the gate threshold level, most spills are delivered almost randomly under the gate level as shown in figure 5-2(a). Therefore, in the former case, the phase of the spill delivery is reproducible yet has a systematic uncertainty near the gate threshold level. The systematic uncertainty follows the PDF obtained from the simulations for each patient breathing pattern. The latter shows the spill delivery has a random uncertainty or lower reproducibility under the gate threshold. The uncertainties discussed in this simulation study indicate the reproducibility of the beam delivery phase, and are expressed with the terms “precision” or “reproducibility” in the following analysis.

5.2.3 Parameters used for the respiratory gating beam delivery simulations

The simulation study undertaken accounted for the following three effects parameters: starting phase, T_{cyc}, and respiratory gate threshold.

5.2.3.1 Effect of start phase of beam delivery

The simulation result could change depending on when the synchrotron magnet excitation pattern or the first beam delivery is initiated from the patient breathing viewpoint. This was observed in chapter 3. The precision of synchrotron-based pulsed proton beam delivery may be also influenced by the starting phase of beam delivery as well as the efficiency (Tsunashima 2008). In order to account for this, by using the phase information obtained from each patient breathing data set exported from the RPM system, the same simulation was repeated for five different starting phase values; 0, $\pi/2$, π, $3\pi/2$ and 2π. From this, the five values of R_{95} were calculated for each starting phase. Among the R_{95}s the average and standard deviation (σ) were calculated for each simulation condition and set of patient breathing data.

5.2.3.2 Effect of synchrotron operation cycle T_{cyc}

The bending magnet excitation pattern of the synchrotron was simulated using various T_{cyc} settings: (i) fixed T_{cyc} settings from the minimum of 2.7, to 3.0, 4.0, 5.0 and 6.0 s, (ii) a fixed T_{cyc} approximately equal to the patient's average respiratory cycle (which was defined as a patient specific T_{cyc}), and (iii) the variable T_{cyc} operation mode shown

in figure 3-1 (Tsunashima 2008). For each of these settings, the R_{95} values were determined and analyzed.

5.2.3.3 Effect of the respiratory gate threshold level

The simulation with a given T_{cyc} for each breathing data set was repeated for three different gate threshold levels with 10%, 20%, and 30% duty cycles in the exhalation phase. The definition of duty cycle (DC) for respiratory gated beam delivery was previously explained in section *3.2.4.3*.As with the other effects discussed earlier, the average R_{95} and its standard deviations were determined for each simulation condition.

5.3 Results

The overview of one simulation result for all T_{cyc}s is shown in figure 5-3. It represents 100 MU equivalent beam delivery simulations for an unstable breathing pattern for seven different values of T_{cyc}, a 30% duty cycle and a starting phase of 0 (discussed in chapter 3). The entire breathing traces were shown for the result of T_{cyc}=2.7s only. The breathing traces just under the gate threshold were shown in gray color from the result of T_{cyc}=3.0 s. The green lines were synchrotron magnet excitation pattern operating for each T_{cyc}. The spill delivery was expressed as a certain value in each color inside of each synchrotron operation pattern. The spill delivery points were also projected on the breathing traces with colored structures for each T_{cyc}. The PDFs were created from these plots on the breathing traces, and are referred to as the residual beam delivery positions. Figure 5-4 shows a PDF of the residual beam delivery positions for the gated delivery obtained from figure 5-3; however, each PDF was not normalized and showed the number of plots for each residual beam delivery position. The PDF of the breathing trace under the gate threshold level was also shown as a reference. This was used as the PDF of the continuous direct current beam delivery assuming the respiratory gated cyclotron beam delivery. The horizontal axis in figure 5-4 corresponds to the amplitude information of the breathing trace. The bin size of the PDF was 0.01 cm.

The vertical axis expressed the number of plots for each bin of PDF corresponding to the residual beam delivery position for each a fixed T_{cyc} of 2.7~ 6 s, patient breathing cycle specific T_{cyc} and the variable T_{cyc}. The left edge of figure 5-4 was regarded as the threshold level and the right side of the graph corresponds to the expiration phase of breathing data. Figure 5-5 shows the cumulative PDF calculated from figure 5-4. The vertical axis was normalized by the total number of plots for each T_{cyc} and the breathing trace under the gate threshold level in order to easily recognize the point of R_{95}. R_{95}s obtained from the CDF graph were analyzed with each gate threshold level for all breathing traces.

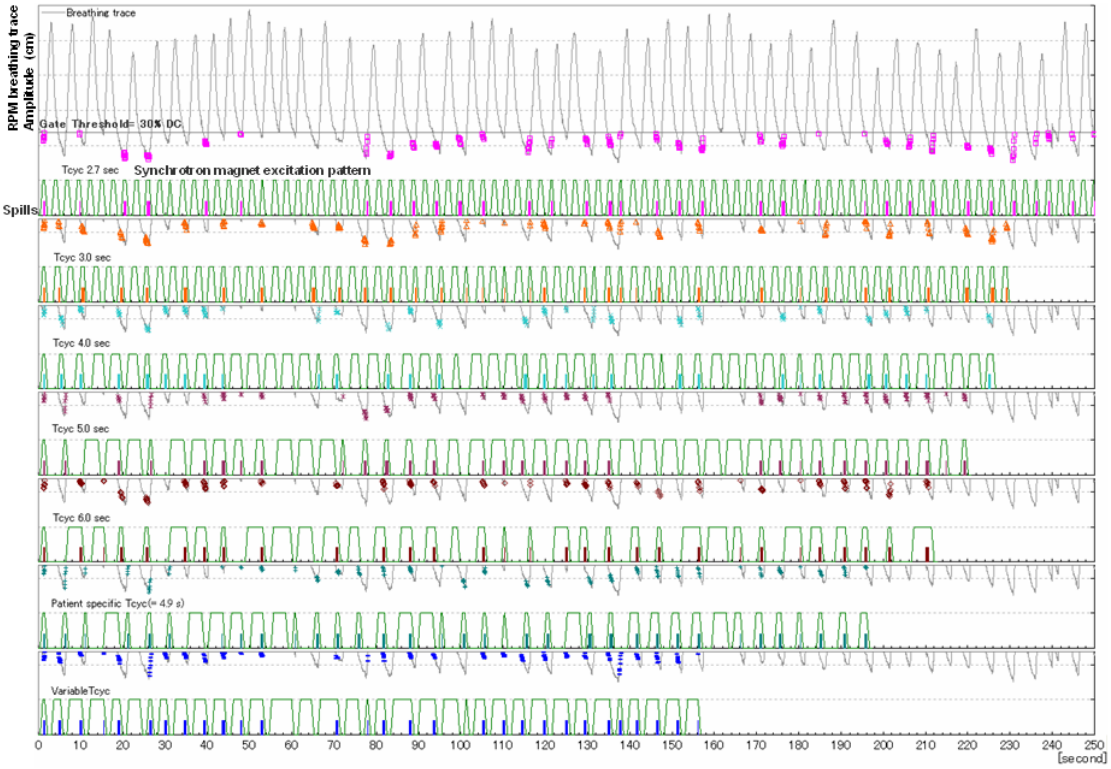

Figure 5- 3. Example of the simulation result of 100 MU equivalent beam delivery at a gate threshold for a 30% duty cycle for each synchrotron operation cycle, T_{cyc}. Each rectangular box shows breathing trace under the gate threshold level (gray line), synchrotron magnet excitation pattern (green line) with T_{cyc} and spill delivery (different color) and the spill delivery points projected on the breathing trace (expressed with symbols). In the simulation, each spill delivery event was recorded and plotted on the breathing trace. The patient specific T_{cyc} used for this simulation was T_{cyc}=4.9 s.

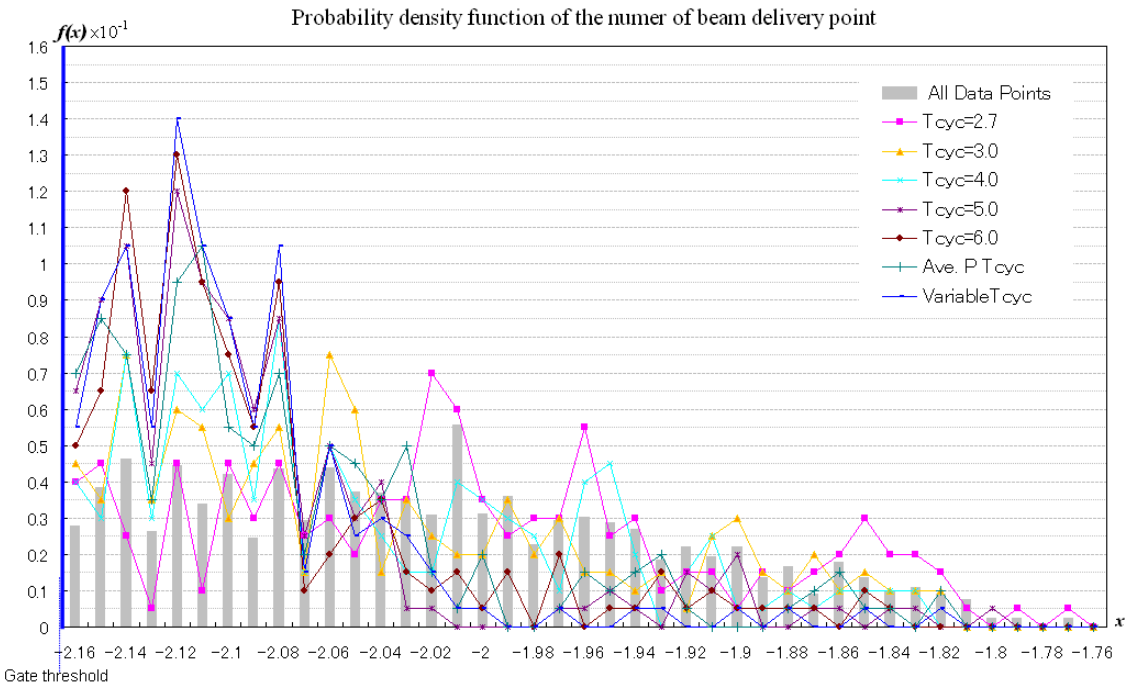

Figure 5- 4. Probability density function (PDF) of the beam delivery points plotted on the breathing trace in figure 5-3 for each T_{cyc}. The horizontal axis corresponds to the amplitude information of the breathing trace (cm). The vertical axis represents the number of symbols for each bin. The gate threshold corresponds to the vertical axis (blue line) on the graph. The PDF shows the number of beam delivery positions (amplitude) on the breathing trace (not normalized) for seven different types of T_{cyc}. The symbols for each PDF correspond to the symbols with same colors in figure 5-3.

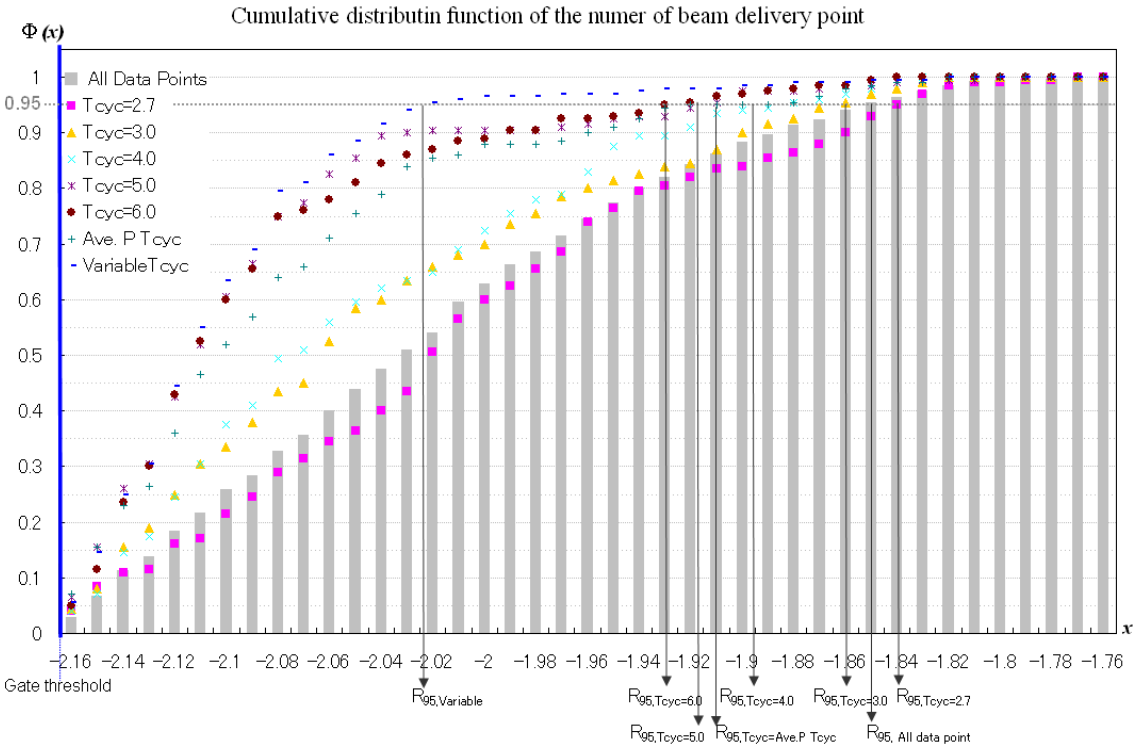

Figure 5- 5. Cumulative distributions of the beam delivery points plotted on the breathing trace in figure 5-3 for each T_{cyc}. This is computed from the PDF in figure 5-4 by cumulative addition from the left side (gate threshold) on figure 5-3. The horizontal axis is the same as the PDF (cm). The R_{95} value represents the relative distance from the amplitude value at the gate threshold to the point indicated by arrows that shows 95% of the total number of beam delivery points (cm).

5.3.1 Effect of the starting phase of beam delivery

Figure 5-6 shows the histograms of the standard deviations (SD) of R_{95} for each simulation with the gate threshold level offset for duty cycles of 10%, 20% and 30% and T_{cyc}s accounting for the starting phase from 0~2π using the total breathing traces (n=70). The SD for one breathing trace (patient) was calculated from the R_{95} values obtained by repeating the simulation from 0~2π for each patient breathing trace. It was repeated for each T_{cyc}.

For T_{cyc}s of 2.7 s and 3.0 s, a group of shorter T_{cyc}s, figure 5-6 showed that there was almost no change seen in the distributions of the standard deviations of R_{95} and the peak positions were consistent at 0.01 regardless of the gate threshold level. For T_{cyc}s of 5.0 s and 6.0 s, a group of longer T_{cyc}s, and also for the patient-specific T_{cyc} pattern (T_{pbre}), the standard deviations of R_{95} for the gate threshold level offset at the 30% duty cycle (DC) were distributed more widely than the distributions for the 10% and 20% DC. However, the distributions were gradually skewed toward 0 with a decrease in the gate threshold level. On the other hand, the standard deviations of R_{95} for the variable T_{cyc} were quite different from the results of both the shorter and longer T_{cyc} groups. The SDs of R_{95} were <0.01 and had the smallest deviation for most of the breathing traces. The distribution did not change and its peak position was consistent

within a SD of less than 0.01 regardless of the gate threshold level. This result showed that there was almost no impact of the starting phase effect on the beam delivery point in the variable T_{cyc} operation regardless of the gate threshold level. Thus the variable T_{cyc} enables one to provide highly reproducible proton beam delivery with respiratory gating. The reproducibility was not influenced by patient breathing pattern, gate threshold level or the starting phase of beam delivery.

For other T_{cyc} operations, the starting phase of beam delivery caused 0.01~0.02 standard deviations of R_{95} for the 30% DC and it also varied depending on breathing pattern. This peak area gradually was shifted toward 0.01 or less as the gate threshold changed dropped from a 30% DC to a 10% DC. In spite of this change, the minimum inherent resolution of the amplitude information of RPM was approximately 0.01~ 0.02. Therefore, 0.01~ 0.02 of the standard deviations of R_{95} caused by the starting phase was smaller than the uncertainty of the amplitude information of the RPM data itself. Thus, the simulation results have demonstrated that the starting phase effect can be regarded as almost negligible. Therefore, the starting phase of beam delivery was ignored in subsequent simulations, and just the average values among five R_{95}s obtained from each simulation accounting for the starting phase effect were used as to represent for each simulation result.

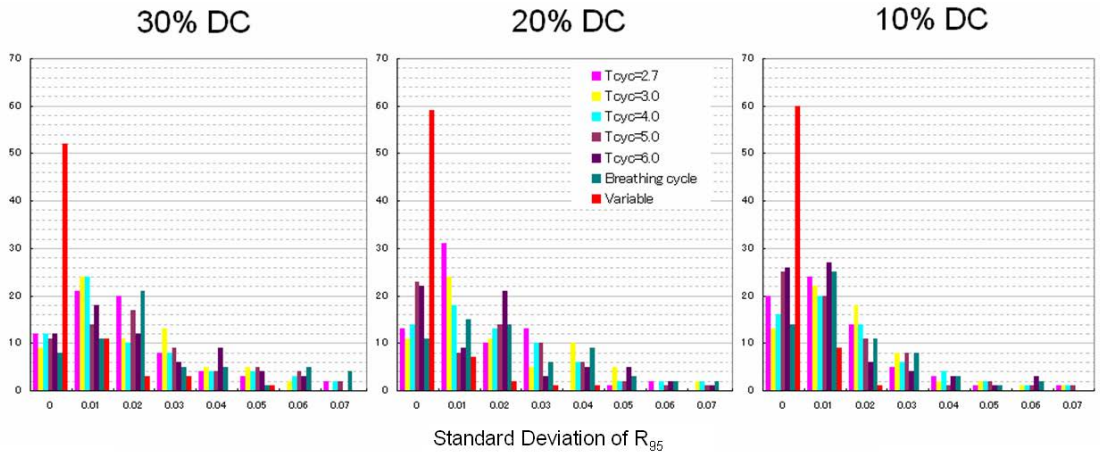

Figure 5- 6. Histograms of the standard deviations of R_{95} accounting for the starting phase of beam delivery in each simulation. The horizontal axis represents the standard deviations of the R_{95} value with several synchrotron operation cycles, T_{cyc}. Each value of the standard deviation of R_{95} expresses how each simulation (with T_{cyc}s for each gate threshold level based on one breathing trace) was influenced by the starting phase effect. Each graph shows how this would change for breathing pattern (70 breathing traces) and the gate threshold level from a 30% DC, 20% DC, and 10% DC.

5.3.2 Effect of synchrotron operation with T_{cyc}

Figure 5-7 shows the summary of the R_{95} distributions resulting from the simulations performed with 70 breathing traces for each combination of synchrotron operation cycles (T_{cyc}) and three gate threshold levels with duty cycles of 10%, 20% and 30%. Similarly the R_{95} distributions for the breathing trace under each gate threshold level were also shown in figure 5-7 and named “reference”. This may be also useful to compare simulation results of synchrotron-based respiratory gated delivery with various types of T_{cyc} with an ideal respiratory gated beam delivery using a continuous beam such as cyclotron-based beam delivery. In this case the PDF of the beam delivery is almost identical to the PDF of each breathing trace under a given gate threshold level.

The R_{95} distributions in figure 5-7 show that the R_{95} distributions of the longer T_{cyc} group (>4.0 s) were almost same for each gate threshold level. Here, most of the spills were delivered consistently within a certain residual position based on each breathing trace. It is from each gate threshold level to R_{95}= 0.1 cm at the peak of each R_{95} distribution for all gate threshold levels of 30%, 20%, and 10% duty cycles. On the other hand, for the shorter T_{cyc} (T_{cyc}=2.0 s and T_{cyc}=3.0 s), all R_{95} distributions seemed to be gradually shifted toward the expiration phase (on the right side of each graph).

For the R_{95} distribution with a gate threshold level of a 30% duty cycle, the mean values of the R_{95} distribution (0.32 cm for T_{cyc}=2.7 s and 0.30 cm for T_{cyc}=3.0 s by an expression of amplitude information in the breathing trace) were shifted by approximately 0.05 - 0.07 cm toward the expiration phase compared to the R_{95} distribution for a longer T_{cyc} (mean value was 0.25 cm). This means that most of the spills were delivered within 0.3 - 0.32 cm by the breathing trace expression from the gate threshold level for a 30% duty cycle. It is wider than the result further longer T_{cyc}, which also indicates that the residual position uncertainty expressed by the breathing trace increases for the shorter T_{cyc} operation. In other words, the reproducibility of the residual position, again expressed by breathing trace, during the spill delivery starts to become inconsistent when using the shorter T_{cyc}, and also becomes more inconsistent when using a higher gate threshold level. Furthermore, when comparing the results from the shorter T_{cyc} with the results of the reference (all data points of the breathing trace under the gate threshold) in figure 5-7, all R_{95} distributions for the shorter T_{cyc} (T_{cyc}<4 s) were similar to the distribution of the reference for all gate threshold levels. This shows that the residual positions expressed by the breathing trace during the beam delivery with the shorter T_{cyc} were similar to those with a continuous beam delivery (or cyclotron-based respiratory gated beam delivery). On the other hand, for the case of

longer T_{cyc} (T_{cyc}>4.0 s), the residual position expressed by the breathing trace during beam delivery was different from the one with continuous beam delivery.

For the case of patient specific T_{cyc} set to approximately the average breathing cycle (T_{bre}) for each patient, the R_{95} distribution was quite similar to the one for longer T_{cyc}, and the difference in the mean values of the R_{95} distribution was less than 0.02, (figure 5-7). Therefore, the use of a patient specific T_{cyc} pattern did not provide a remarkable benefit. With respect to variable T_{cyc} operation, there was a unique result in the R_{95} distribution. The change in the mean values of the R_{95} distributions for different gate threshold levels was 0.21 cm for a 30% duty cycle to 0.14 cm for a 10% duty cycle. This was a smaller change than for any other T_{cyc} operation as well as a change in standard deviations which associated with the breathing pattern. Hence, the variable T_{cyc} mode of operation provided robustness to respiratory gated beam delivery regardless of gate threshold level and/or patient breathing pattern. This means that, as explained by the R_{95} distributions, the quality of beam delivery was reproducible with a small residual position. In addition, one could state that the variable T_{cyc} provided a more “precise” beam delivery to the target than the other T_{cyc} patterns.

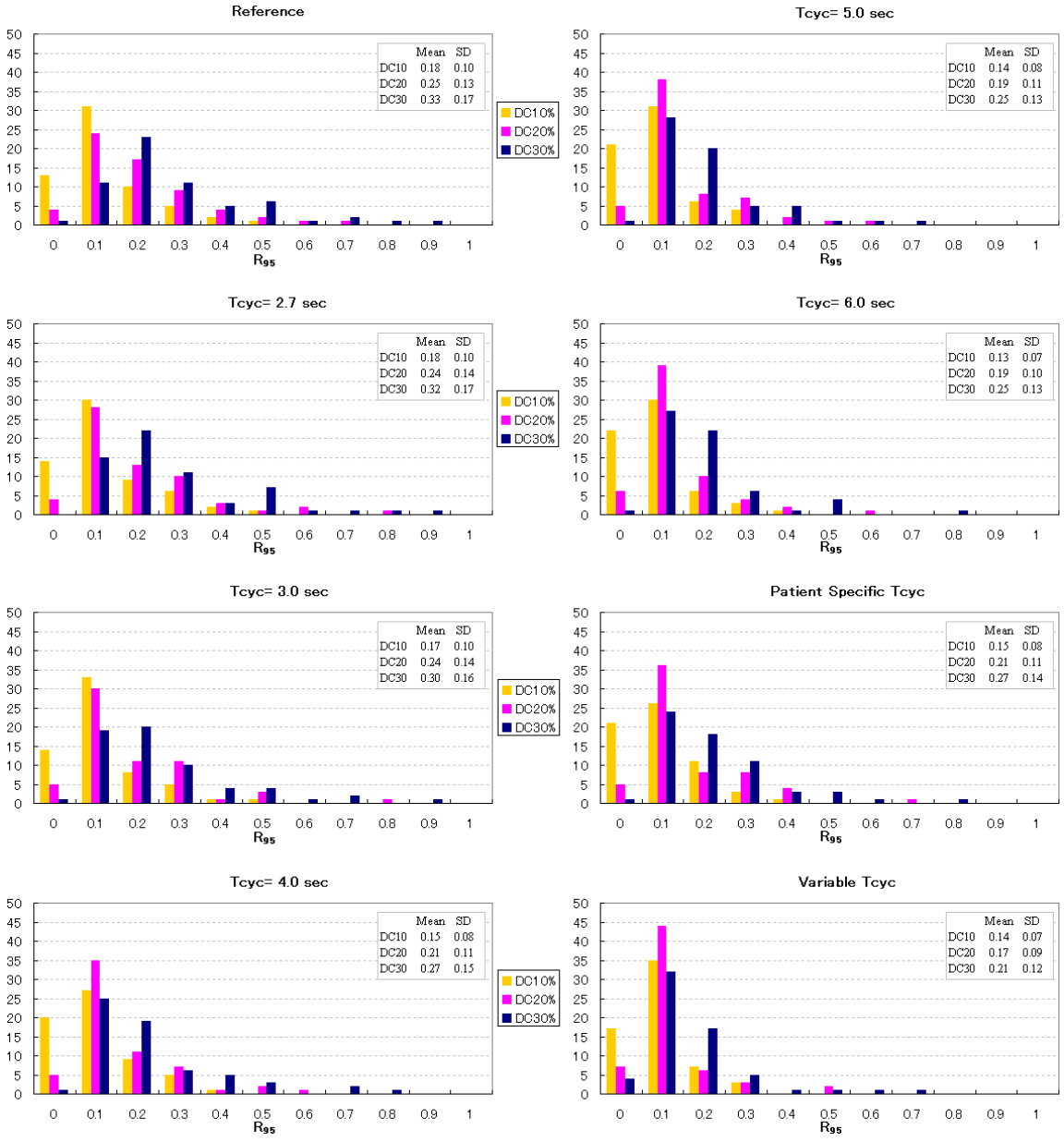

Figure 5- 7. Histograms of R_{95} for each T_{cyc} and DC as the gating threshold level for 70 breathing traces. The mean value and standard deviation (SD) for each distribution are shown in the graphs.

5.3.3 Effect of the respiratory gate threshold level

In figure 5-7, for the gate threshold of a 30% duty cycle, the R_{95} distributions were skewed toward the threshold side (at R_{95}=0) as T_{cyc} become longer, as well as for the patient specific T_{cyc} and the variable T_{cyc}. As a general trend for all R_{95} distributions with a gate threshold level for the 30% duty cycle, the peaks of R_{95} distributions were located around 0.1~ 0.2 cm and average value of the R_{95} distribution for all T_{cyc} was 0.29±0.04 cm. The variances of the R_{95} distributions for each T_{cyc} operation increased up to 0.15 in the root mean square (RMS). Similarly the averages and variances of the R_{95} distributions for gate threshold levels of the 20% and 10% duty cycles are listed in table 5.1. It should be noted that if one uses a higher gate threshold level, the R_{95} distribution is more sensitive to the synchrotron operation cycle of T_{cyc}. However, for the gate threshold level of a 10% and 20% duty cycle, there was not as big change in the R_{95} distribution (0.16±0.02, 0.2±0.03 in average and 0.09~ 0.12 in RMS) and it became less sensitive to the synchrotron operational parameter, T_{cyc} compared with the gate threshold of a 30% duty cycle. Table 5-1 supported that, as already seen in figure 5-7, the R_{95} distributions became skewed with decrement in the gate threshold level. The skewness of the R_{95} distribution for the gate threshold level of a 10% duty cycle was similar to the one for the 20% duty cycle in the shorter T_{cyc} operation. This trend

became more consistent for longer values of T_{cyc} (T_{cyc}>3.0 sec). From these results it is clear that selection of a gate threshold level is an important factor to offer precise beam delivery in respiratory gating. In order to achieve it, the gate threshold level should be selected to be neither too high nor too low, and an optimal gate threshold has a robust quality with regard to precision of the beam delivery independent of both the T_{cyc} and patient breathing. Therefore, notable findings in this study were that, first for a longer T_{cyc}(T_{cyc}≥5.0), the R_{95} distribution has robustness and precise beam delivery is available regardless of the gate threshold setting (figure 5-7). Secondly the variable T_{cyc} was the most robust synchrotron operation pattern for respiratory gating and was not affected by gate threshold level or patient breathing because for the variable T_{cyc} operation, the R_{95} distributions ranged 0.14±0.07, 0.17±0.09 and 0.21±0.12 in for the gate threshold level of the 10, 20 and 30% duty cycles respectively. These were the minimum values compared with other R_{95} distributions of T_{cyc} for each gate threshold level.

Gate threshold	*Mean*	*SD*	***RMS***
10% DC	0.16	0.02	0.09
20% DC	0.22	0.03	0.12
30% DC	0.29	0.04	0.15

Table 5- 1. Summary of the mean and standard deviation (SD) values in the overall R_{95} distributions with T_{cyc} for each gate threshold level used in figure 5-7. RMS stands for root mean square.

5.4 Discussion

The results discussed above show that, for respiratory gated passively scattered proton beam delivery, the precision of the beam delivery depends on the combination of the magnetic excitation cycle of the synchrotron operation (T_{cyc}) and the gate threshold level chosen. Secondly the impact of the starting phase effect on the precision of the proton beam delivery was almost negligible. It should be noted that even if the proton beam delivery with respiratory gating starts at any phase, the consequential precision does not change. Figure 5-7 showed when the gated beam delivery is most probably undergone on the basis of breathing information. By looking at the term R_{95}, one can see that most of gated beam delivery occurs when the amplitude of the breathing trace is in between the gate threshold level and R_{95}.

In this section, the focus was placed on the breathing data points between each gate threshold level and R_{95}. The ratio of these data points to the total breathing data for each patient breathing trace was defined as the effective duty cycle (DC). This was compared with the duty cycle originally defined and used as the gate threshold level, which is defined as the nominal duty cycle. The ratios of the effective duty cycle to the nominal duty cycle are averaged over the all breathing traces used in this study and plotted in figure 5- 8 with respect to synchrotron operation with T_{cyc} and gate threshold

level. The maximum and minimum values of each distribution of the effective duty cycle for each T_{cyc} were also shown in graph for each threshold level. As the plots of the "reference" in figure 5-8 show, the closer the ratios of the effective duty cycle to the nominal duty cycle were to 0.95, the more uniform was the total beam delivery over all spills to the residual motion expressed by the breathing traces. However, when the ratios of the effective duty cycle to the nominal duty cycle were less than 0.95, the beam delivery was non-uniform and occurred at the residual positions between the gate threshold level and R_{95}. For the former case, although each spill delivery is basically a uniform random delivery and represents statistically more uniform beam delivery over all spills. For the latter, the residual positions during beam delivery cluster toward the gate threshold following a Poisson distribution. For the case of the variable T_{cyc}, the residual position error in accordance with R_{95} was smaller compared with any other T_{cyc}, and the ratios of the effective duty cycle to the nominal duty cycle, were 0.71, 0.78 and 0.83 for the gate threshold levels of the 30%, 20% and 10 % duty cycles, respectively. These numbers were smaller than those with any other T_{cyc} for each condition. Therefore respiratory gated beam delivery with variable T_{cyc} operation has less uncertainty. This indicates that the beam delivery with the variable T_{cyc} has the

best reproducibility and can occur at a more consistent phase expressed by a smaller residual uncertainty than any other case of T_{cyc}.

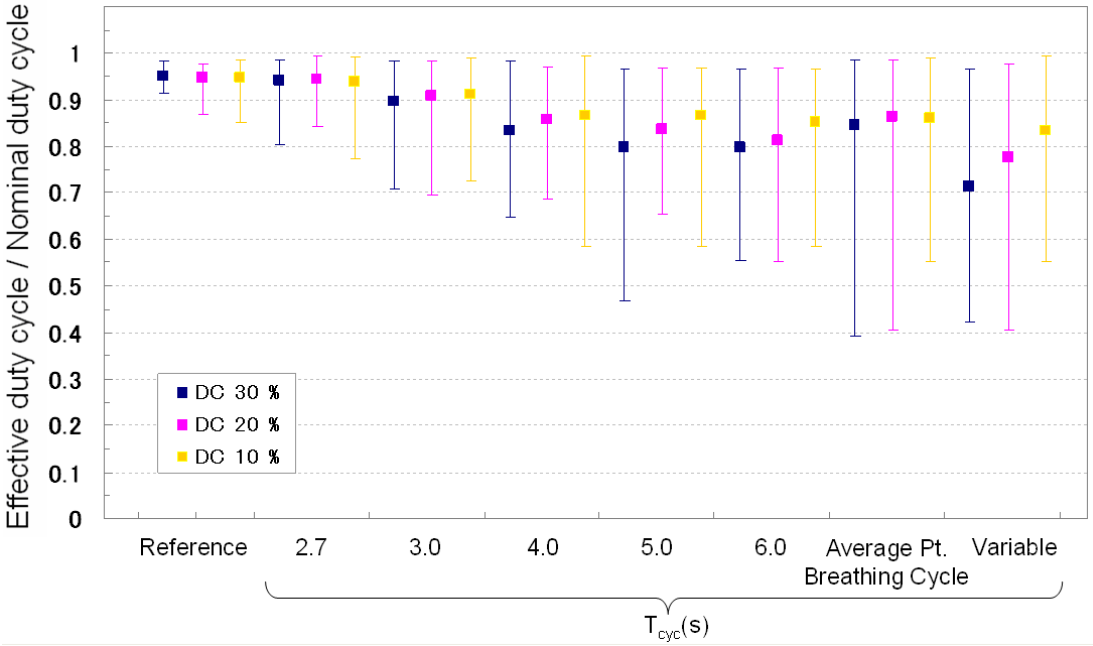

Figure 5- 8. Ratio of effective duty cycle to nominal duty cycle averaged over 70 breathing traces. The width between the maximum and minimum values represents how the beam delivery is independent of a patient breathing pattern. The effective duty cycle of the "Reference" (all data points of the breathing trace under gate threshold level) is the ideal uniform beam delivery and should be about 95 because R_{95} is the value indicating the points of 95% of the cumulative residual positions. The maximum and minimum values of the Reference are, in this case, related to inherent uncertainties caused by a limitation in the number of data points of breathing trace.

As consideration is taken into the beam quality with respect to the consistency or reproducibility point of view, there is enough information in figure 5-8 to discuss the quality of the respiratory gated proton beam delivery. The effective duty cycle was utilized to express that most (95%) beam delivery occurred when the patient breathing trace was within the area between the gate threshold level and R_{95}. On the other hand, another area including the remaining 5% was conversely interpreted to be where most beams would not likely be delivered. The focus is placed on this area. The duty cycle calculated by the breathing signal data points under the R_{95} level was defined as a non-beam delivery duty cycle (nDC). This means that when the breathing trace is under the level of nDC, beam delivery scarcely occurs. The nDCs calculated for 70 breathing traces for each value of T_{cyc} and gate threshold level are listed in Table 5-2. The numbers in the table show, as nDC becomes greater, the area that the spills would not be delivered becomes larger compared with the effective duty cycle. This reveals that the probability that the spills would be uniformly delivered within the duty cycle becomes lower. A decrease in the probability of the beam delivery is in general observed in the end-expiration phase except in the case that the breathing pattern drifts up and down. For example, for the shorter T_{cyc} based synchrotron operation (T_{cyc}=2.7 and 3.0s), the average values of the nDC for each gate threshold condition were less

than 10%. The probability that the spills were not delivered was quite low and therefore the spills were almost uniformly delivered and the likelihood of simultaneously missing the beam delivery in end-expiration phase is less over all spills when the breathing signal was below the gate threshold level. In table 5-2, the variances of nDC (mean, maximum and minimum values of nDC for all breathing traces) show how much the variability of the missing beam delivery event were influenced by patient breathing traces, T_{cyc} and gate threshold level. For a longer T_{cyc} operating mode (T_{cyc}= 5 s and 6 s) or variable T_{cyc} mode, the average nDCs were higher compared with the shorter T_{cyc}s. The probability that the spills were not delivered was three to four times greater for the gate threshold level of a 30% and 20% duty cycle, and two and three times greater for gate threshold of a 10% duty cycle as compared to the shorter T_{cyc} operation modes. The probability became much higher with use of a higher gate threshold. It should be noted, however, that the longer T_{cyc} and variable T_{cyc} operations alternatively have at least one benefit that the synchrotron operation with larger nDC offers more reproducible beam delivery even for an irregular breathing pattern. Figure 5-3 shows several colored symbols superimposed on the breathing trace for each T_{cyc} operation to express the spill delivery point resulting from simulation. For the results of the shorter T_{cyc}, each spill delivery is widely

distributed, and the residual positions where the beam delivery occurs and its R_{95} were easily influenced by an irregular breathing pattern especially when the patient's baseline drifted up and down. However, for the longer T_{cyc} and the variable T_{cyc}, the spill delivery points expressed by colored symbols in figure 5-3 were relatively distributed close to the gate threshold level and barely affected by such an irregular breathing pattern. Thus, the benefit of the longer T_{cyc} and variable T_{cyc} operations was a robust reproducibility for the beam delivery independent of patient breathing pattern. The reproducibility should be regarded as one criterion to indicate the quality of respiratory gated beam delivery. However since relating the accuracy of the beam delivery directly to residuals has not been investigated in this study, the term of quality discussed in this study was limited to precision only. A more comprehensive discussion of the quality of the beam delivery integrating both accuracy and precision needs to be done as a next step.

For both the respiratory gated beam delivery mode and free-breathing based beam delivery mode, the current proton treatment planning system needs to account for the target motion uncertainty using multiple phases of CT data sets, an average CT made from a four-dimensional CT and/or a free-breathing CT (Engelsman 2006, Kang 2007 and Mori 2010). Especially for the synchrotron-based respiratory gated mode,

one should account for not only the dosimetric impact of target motion uncertainty but also the most likely target position in which most of the spills would be delivered based on the results obtained in this study. As some of the results in this study already showed, it is not guaranteed that all spills would be delivered uniformly to the residual motion under the gate threshold level, which depends on synchrotron operation. For example, when using the shorter T_{cyc} for respiratory gating, it is preferable to use a CT data set averaged over some series of CT data sets in the expiration phase (under the gate threshold level) for treatment planning rather than a series of expiration phase CT data because most of the spills are delivered uniformly to the residual motion under the gate threshold. On the other hand, for the variable T_{cyc} or longer T_{cyc} operations, since the probability of missing the spills delivered in the end-expiration phase is higher, treatment planning with either a series of end-expiration phase CT data sets or the averaged CT data set mentioned above would not be enough to account for this effect. Therefore, for the variable T_{cyc} or longer T_{cyc} synchrotron operations, it is suggested that weighting factors based on R_{95} should be applied to the averaged CT data set used in the dose calculation for treatment planning. Furthermore, since the breathing traces, are usually acquired from external patient breathing motion, they do not always

express accurate residual motions (Kini 2003, Tsunashima 2004). Therefore, the uncertainty in the breathing traces should be taken into account in treatment planning.

It should be noted that these results and discussion are based on the synchrotron at PTCH, and results may be slightly different for each synchrotron manufacturer or facility because the spill shape and length in the time domain and other parameters associated with synchrotron operation specified by each facility are different. According to the specifications of the synchrotron used in this study, as shown in figure 5-1, each spill is controlled to have a stable output that is consistent spill by spill. However, some other facilities use a spill that appears skewed toward the beginning of the spill such as a Poisson distribution (Noda *et al* 1996). In this case, most of the spills are delivered in the beginning of the beam extraction phase. Assuming respiratory gated beam delivery was used with this spill structure, the overall effective duty cycles would be much narrower than for the variable T_{cyc} and longer T_{cyc} operation, and eventually actual residual motion during beam delivery would be much smaller and the most of spills would rarely be delivered in the end-expiration phase.

Non-beam delivery duty cycle

T_{cyc}	30%DC gate threshold			20%DC gate threshold			10%DC gate threshold		
	Ave	*Max*	*Min*	**Ave**	*Max*	*Min*	**Ave**	*Max*	*Min*
2.7 sec	**1.8**	6.0	0.0	**1.1**	3.4	0.1	**0.6**	2.3	0.0
3.0 sec	**3.1**	8.4	0.3	**1.9**	6.2	0.4	**0.9**	2.9	0.0
4.0 sec	**5.0**	10.9	0.5	**2.9**	6.5	0.6	**1.3**	4.5	0.0
5.0 sec	**6.0**	16.1	1.1	**3.3**	7.3	0.6	**1.3**	4.5	0.3
6.0 sec	**6.1**	13.8	1.1	**3.8**	9.5	0.6	**1.5**	4.5	0.2
Ave Pt. breathing cycle	**4.7**	19.0	0.0	**2.8**	11.8	0.3	**1.4**	4.6	0.1
Variable	**8.6**	17.8	1.1	**4.5**	11.8	0.5	**1.7**	4.6	0.0

Table 5- 2. Non-beam delivery duty cycle. The numbers are duty cycles for which beams are probably NOT delivered for each gate threshold level. The distribution of the non-beam delivery duty cycle for all breathing traces are shown with average, maximum and minimum values for each T_{cyc} and gate threshold level. Large values suggest that the probability of missing beam delivery in end-expiration increases and most of beam is delivered near the gate threshold level (Tsunashima et al 2010).

5.5 **Conclusions**

As a feasibility study of the implementation of synchrotron-based respiratory gated beam delivery, this investigation was focused on the quality of beam delivery. The simulation of realistic respiratory gated beam delivery was performed using patient breathing data and the magnet excitation pattern of a synchrotron.. The results obtained from this study provided some useful information for choosing an appropriate synchrotron operation pattern, T_{cyc}, in order to perform more precise beam delivery with respiratory gating. The reproducibility of beam delivery was used as criteria to assess the quality of respiratory gated beam delivery. The overall results obtained from this study and the results from the chapter 3 offer the optimal parameters for high quality and highly efficient beam delivery for respiratory gated passively scattered proton therapy. From these results, one can conclude that the variable T_{cyc} operation can offer the most efficient and precise beam delivery for synchrotron-based respiratory gated proton beam delivery in passively scattered mode.

Chapter 6. Specific aim 2: Beam scanning delivery Part I

Assess the accuracy of dose delivery in respiratory gated proton therapy with scanning beam delivery: Experimental evaluation of the interplay effect for proton scanning beam delivery

6.1 Introduction

Scanning beam delivery cannot only provide a uniform dose distribution to the target but also spare the dose in organs at risk (OAR). It makes it possible to create a complicated dose distribution. Therefore head and neck tumors could be more suitably treated with the proton scanning beam technique. Pediatric cases where a small field and much more limited dose need to be delivered could significantly benefit from proton scanning beam treatment. Furthermore, the higher dose uniformity limited only to the target would be naturally desired in lung or liver treatments as well. However, because the dose distribution is composed of a superposition of many beamlets (spot beams) in scanning beam delivery, the dose distribution is very sensitive to the errors in the reproducibility of the position of the target and its surrounding organs. Particularly for the lung and liver, where organs move with a periodic motion mainly

due to the breathing, the quality of the delivered dose is a main concern for scanning beam delivery to the moving target. This is challenging, and the use of the respiratory gating technique could be a more helpful approach to achieve it.

The main goal in this chapter is to evaluate the feasibility of respiratory gated scanning beam delivery. It is also very important to comprehend the impact of motion on the dose distributions in scanning beam mode. Several studies concerning the interplay between motion and scanning beam delivery have been published; however, these are based on simulation studies (Kraus 2011, Knopf 2011) and no real measured data has been published for proton scanning beams. However, some experimental studies of the interplay effects for carbon beams have been published (Bert 2008, Furukawa 2011). Unfortunately, for a clinical case with the target volume in a heterogeneous medium, it is very complicated to analyze the interplay effect arising from the 3D dose deterioration caused by mixing many scanning beams with different energies in the depth direction.

Therefore, in this study, a more streamlined experiment was carried out to investigate the interplay effect for proton scanning beams. The aim of this experiment is to understand how scanning beam delivery and its associated dose distributions would be affected by motion in a very simple situation. The experimental study

focuses on a fundamental understanding of the interplay effect by mono energy scan beam delivery in a uniform water equivalent material. The measurements performed in this study are basically two dimensional measurements using uniform beam scanning for a single energy layer. The deteriorations in the dose distribution caused by the motion for one energy layer were analyzed by the comparison of the dose distribution without motion.

6.2 Materials and Methods

For the measurements, 2D lateral dose distributions at a certain depth were acquired using a 2D chamber array detector. The motion effect was measured using a moving plat platform and the 2D detector. Details of the equipment and the measurement procedure of the measurement are discussed below.

6.2.1 Equipment

6.2.1.1 2D array detector

The I'mRT matrix (IBA, Schwarzenbruck, Germany figure 6-1) was used for 2D dose measurements. The matrix is composed of chamber arrays with 4.5 φ x 5mm height chambers placed in a 32x32 array with 7.62 mm spacing (center to center) between each chamber. Although the chamber array does not have as fine resolution as films, the benefit is that first it is very easy to perform repeat measurements, and secondly it offers a real time direct reading though a PC. Thus there is no need for post-measurement processing, whereas for film measurement there would be a need for developing and/or digitizing the irradiated films and for careful preservation of them as well. Also, the linear energy transfer (LET) effect is nearly negligible for chamber measurements compared with film measurements. It is very convenient for proton

beam measurements because the proton volume dose distribution is composed of many different energy proton beams, and if using films, the LET effect differs for each beam energy and needs to be corrected for accurate results. Therefore, the 2D array detector is the most suitable detector for this type of measurement. Regarding the resolution issue, since the acquired 2D dose can be interpolated, 4 mm resolution is used in the measurement, and the irradiated field was a very simple square field, it is not a relevant problem in this measurement.

Figure 6- 1. ImRT MatriXX (IBA®, Schwarzenbruck).

6.2.1.2 Moving plat form and motion

The moving plat form is composed of an acrylic board combined with sliding rails, a stepping motor unit (VXM stepping motor controller, VELMEX, Inc.) and a PC (figure 6-2). The stepping motor is attached to a lead screw with a drive nut. As the stepping motor is controlled to rotate the axis, the lead rotation is also synchronized with the motor and consequently the drive nut goes back and forth on the lead screw. Since the motion platform is directly connected to the drive nut, the drive nut motion reflects on the platform motion. Since only one stepping motor is used in this unit, the motion of the platform expresses one axis (dimensional) motion, linear motion. The motion pattern is programmed beforehand and the motion data were sent to the stepping motor control unit through the PC.

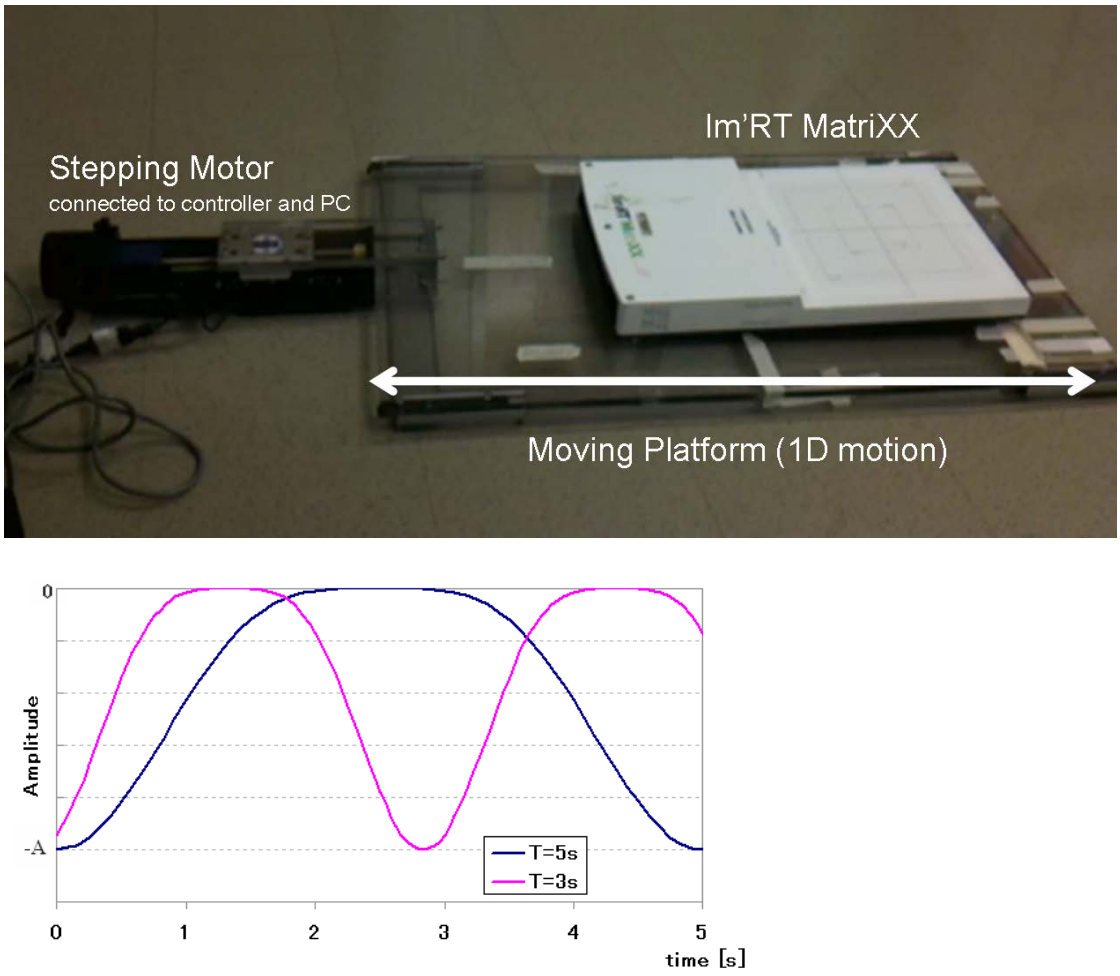

Figure 6- 2. Setup for the measurement (upper) and a sinusoidal motion pattern (lower).

The platform motion followed a theoretical patient breathing model. The use of the sinusoidal motion is one of the well known breathing models (Lujan 1999):

$$f(t)=A*\cos^{n}(\pi/T*t+\psi)$$

A: Motion amplitude [mm]

T: Cycle period [s]

Ψ: Original phase

In this study, a sinusoidal function raised to the 4^{th} power motion (n=4) was used. The phantom moved back and forth in the superior-inferior (SI) direction. The maximum superior amplitude of zero was set at isocenter and the moving platform moved down to the minimum amplitude of –A with period T. Several different motion patterns with the combination of the cycle T= 3 and 5s and the amplitude A= 2, 5, 10 and 20 mm were used to observe the dosimetric impact due to motion.

6.2.1.3 Scan beam field and its delivery pattern

Measurements were performed for a simple geometry with uniform water equivalent materials using a mono energy beam. The energy of proton beam was 173.7 MeV, whose residual range is equivalent to 20 cm in water. The energy was chosen based on the assumption that the maximum energy most often used in thoracic treatment is approximately 20 cm in water. The spot size with this energy was approximately 19.6 mm (FWHM) at the Bragg peak in water (figure 6-3). Figure 6-4 shows the relationship between the proton energy and the spot size at the Bragg peak. As seen in figure 6-4, the spot size around the energy area used in this study expresses approximately the minimum spot size. Thus, this experiment was performed with the minimum spot size available in our facility (Gillin 2010).

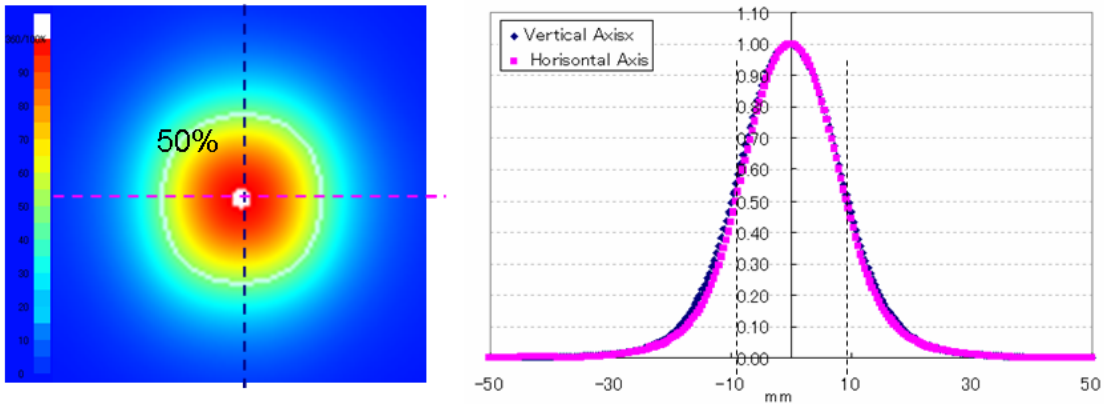

Figure 6- 3. Spot size of the 173.9 MeV beam at the Bragg Peak.

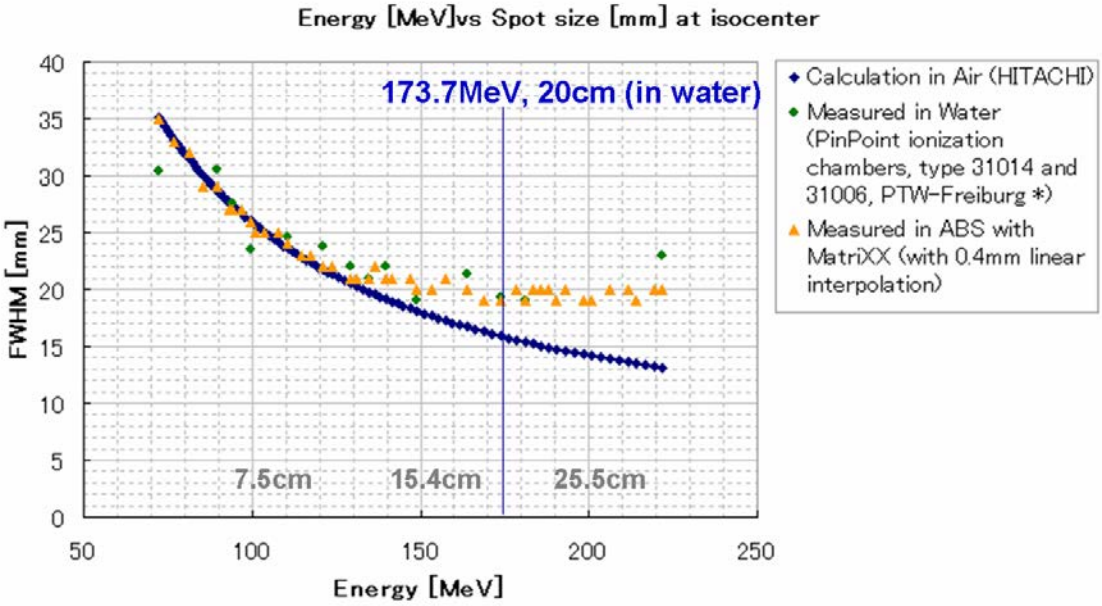

Figure 6- 4. Relationship between energy and spot size calculation in air, measured water (Anand 2010) and measured in ABS.

Using the spot beam, a 10x10 cm^2 field was created with inter-spot spacing of 8 mm along both the vertical (IS direction) and horizontal axes (Zhu 2010). In order to make the 10x10 cm^2 field, 13 spots were delivered in both the horizontal and vertical directions, resulting in 13x13=169 spots in total. Regarding the spot delivery pattern, the sequence of the spot scan delivery at our facility is governed by spot position (x and y), spot weight and beam energy (scanning layer). The user can arrange the spot delivery sequence to suit one's needs. Therefore, in this series of measurements two types of spot beam delivery patterns were prepared: scan pattern one consists of spot delivery starting from the edge of the field, and moving to each successive spot position by 8 mm in the direction of phantom motion (the Y direction) until all 13 spots are delivered and then moves perpendicular to the phantom motion (the X direction), by 8 mm, and then 13 spots are delivered in the opposite direction (figure 6-5 a). Scan pattern two is perpendicular to the scan pattern one, and the main beam scan line is perpendicular to the phantom motion (figure 6-5 b).

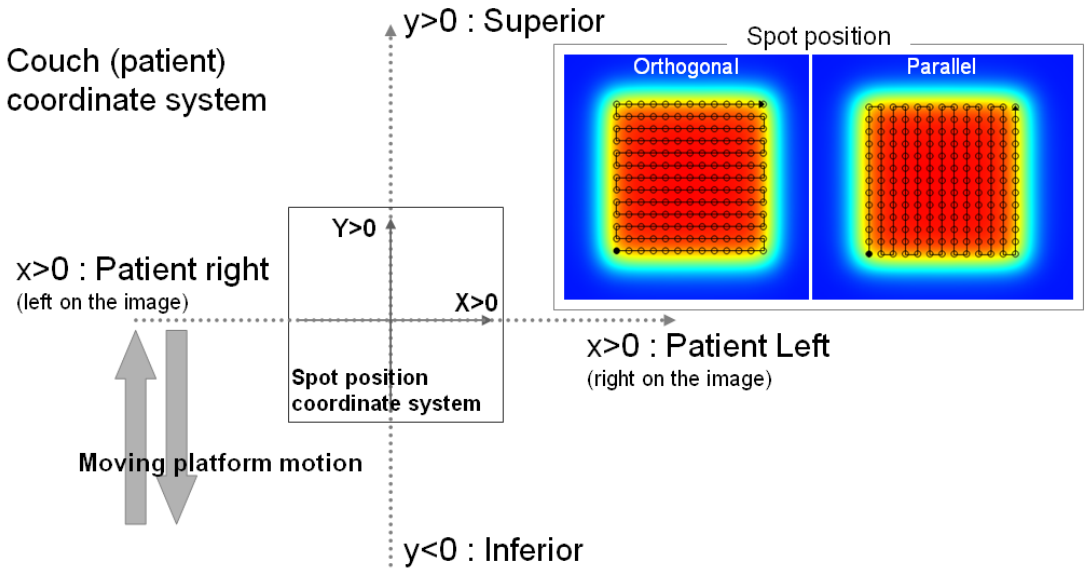

Figure 6- 5. Definition of the coordinate system in a patient and the spot scanning plane.

6.2.1.4 Re-painting

The spot beam in PTCH has a deliverable dose limit set from 0.005 MU up to 0.04 MU. The dose range is consistent for all energies. For this reason, it is necessary to consider the repainting procedure with respect to the deliverable spot dose limitation in PTCH. Repainting due to the spot dose limit is quite different from the repainting issue well known as a technique for compensating errors of spot delivery. For example, if 100 MU needs to be delivered to a given volume, in principal a maximum of 25 times the spot delivery or 25 times paintings are required at the distal energy layer of the volume.

In the measurements, the 10x10 cm^2 field made by 169 spots with 8 mm spot spacing was defined as a single painting and also used as a reference 2D dose distribution. For the repainting the spot delivery position started from the last spot position finished in the previous painting, 169 th spot in the previous scan. The spot position returns to original spot position by odd times of number of paintings in the scan delivery pattern used in the measurements.

In order to investigate the relationship between the repainting and the interplay effect, the beam delivery time or scan speed is also an important parameter. One spot delivery is composed of two processes; one is spot delivery and the other is

the transition to the next spot position. The spot delivery time varies from 1ms for 0.005 MU delivery to 4 ms for 0.04 MU delivery as previously explained in chapter 4. The spot position transition time also varies depending on the energy and the distance between the spots. The 8 mm spot spacing used in the measurement takes approximately 3 ms in both the X and Y directions and it is nearly consistent in these measurements. Delivery of a single spot beam consequently takes approximately 7 ms for a 0.04 MU spot dose and 4 ms for a 0.005 MU spot dose.

This study focused on the interplay effect for 0.04 MU spot beam delivery. The reason for this selection is first because the maximum spot dose is expected to be delivered especially at the distal end of the proton range, and secondly the total beam delivery time for 0.004 spot dose delivery is expected to be longest and which could represent the worst case scenario of the dose deterioration caused by motion. Therefore the total beam delivery time for creating a 10x10 cm^2 field with 169 spots is approximately 1.18 s for single layer painting. This was repeated from one layer paint up to 16 paintings, and the change in the dose deterioration by the number of the paintings was analyzed.

6.2.2 Setup for the measurements

Figure 6-6 shows the setup for the measurement setting. The experiment was carried out in the gantry 3 treatment room at PTCH. The gantry angle was 0 degrees. The moving platform with the stepping motor unit was placed on the treatment couch and was positioned in order that the origin of the moving platform was set at the isocenter. The motion was confined to superior-inferior (SI direction) direction on the couch. The coordinate system on the treatment couch was defined such that the superior direction was +y and inferior direction was –y, and ±x were similarly defined in figure 6-6. The 2D ion chamber array detector was placed on the moving platform. The center of the chamber array was set at the isocenter in y= 0 position of the moving platform. Based on y=0 position, the moving platform unit moved toward the inferior direction, y<0, down to the motion amplitude of A, y=-A. Therefore, as it was translated into the patient breathing motion and coordinate system, the platform position at y=0 was the end-expiration phase and y=-A was the peak of the inspiration phase. The spot position coordinate system, X and Y corresponded to -y and -x for each. For the detector setup in the depth direction, the effective center of the chamber arrays in the beam direction, depth direction, which was 4 mm from the surface of the chamber array detector, was set at isocenter. Solid water slabs with 19 cm water equivalent thickness were stacked

on top of the 2D chamber array detector. The unit composed of the water slabs, 2D chamber array and the moving platform was controlled to undergo sinusoidal motion.

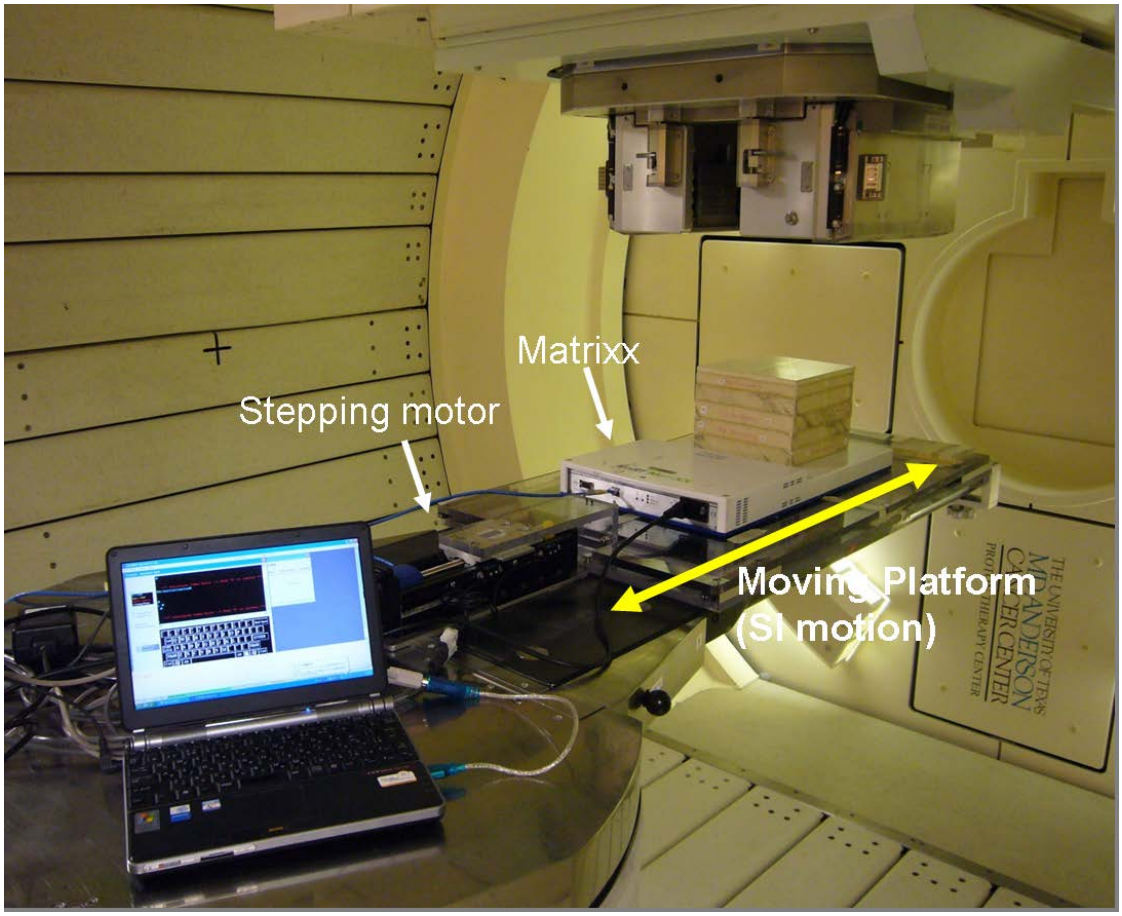

Figure 6- 6. Setup for the measurement. The moving plat form with controller and I'mRT MatriXX (2D chamber array detector) were placed on the treatment couch. The water equivalent blocks were stuck in 19 cm (physical thickness). The gantry angle is set at 0 degree.

6.2.3 Measurements

The 10x10cm^2 uniform field was delivered to the 2D ion chamber array detector using a 173.7 MeV beam with an approximately 20 mm spot size (FWHM in water) and 8 mm spot spacing. The two types of scan pattern directions were used to create the field using scanning directions orthogonal and perpendicular scan to the phantom motion. The 10x10 cm^2 field was delivered for different motion amplitudes: A=0 (reference), 3, 5, 10 and 20 mm and motion cycles T=3 s and 5 s. The same measurements were repeated changing the number of paintings from 1 to 16 times.

6.2.4 Starting phase effect

As mentioned above, a single painting with 169 spots takes only about 1.2 s. The dose distributions made during this short time span are therefore very sensitive to object motion during beam delivery (figure 6-7). Especially since the platform motion used in this measurement was not a simple sinusoidal motion but weighted on the end expiation phase, the consequent dose distribution should vary depending on the phase of motion in which the beam delivery is initiated. This was defined as the starting phase effect. This does not only affect the dosimetric quality but also the total beam delivery time for synchrotron-based respiratory gated proton beam irradiation.

Therefore the measurements under each condition mentioned above were furthermore repeated at different phases of platform motion. However, since it was difficult to start beam the delivery at exactly the same phase due to mechanical delay, the beam delivery was ultimately initiated at two different phases: when the moving platform was located at the top in the SI direction, phase "+", and when the moving platform was at the bottom position, phase "–" (figure 6-7). Beam delivery with same conditions was initiated around each phase multiple times, from which the worse and best dose deterioration were selected as representative results of dose distributions at each starting phase.

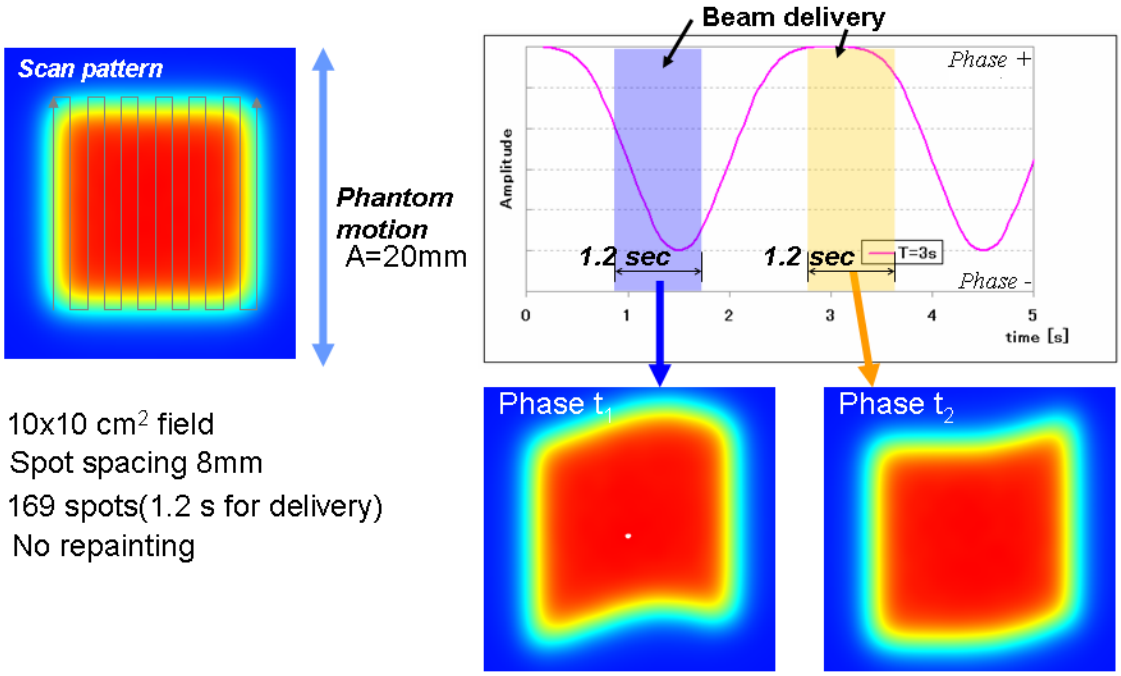

Figure 6- 7. Example of the starting phase effect.

6.2.5 Analysis

The dose distributions obtained from measurement, including the motion for each amplitude and cycle, were compared with the reference dose distribution, which was the same beam delivery without motion. The comparison focused on the dose uniformity inside of a certain reason of interest (ROI) because the dose deterioration caused by the object motion directly reflects on the decrease in the dose homogeneity relative to the reference uniformity in the ROI. A similar comparison using the quantified homogeneity was performed to study the interplay effect for a carbon scanning beam by Bert et al (Bert 2008). Here the dose homogeneity, *H*, is defined by

$$\mathbf{H=1-\sigma/D_{ave}}$$

σ:standard deviation

D_{ave}: mean dose

First, based on the reference dose distribution (no motion), 95%, 90% and 50% isodose comparisons were delineated as ROI_{95}, ROI_{90} and ROI_{50}, and the dose homogeneities of the reference were computed for each ROI and defined as $H_{ref,\,95}$, $H_{ref,\,90}$ and $H_{ref,\,50}$. Secondly, with the other measured dose distribution including motion, the dose

homogeneities for each measurement condition (motion cycle, amplitude and the number of paintings) were also computed inside of the ROIs copied from the ones made based on the reference dose distributions. These were defined as $H_{95,}$ $H_{90\ and}$ H_{50} , where the term "n" indicates the number of paintings (figure 6-8). Concerning the ratio of H to H_{ref} for each isodose comparison, the closer H/H_{ref} is to unity, the more similar is the dose homogeneity with and without motion. The dosimetric impact due to motion could be seen in the change in the homogeneity ratio, H/H_{ref}, with increase in the number of the paintings for different motion amplitudes and cycles. The impact due to the difference in the scan direction, orthogonal and perpendicular to the object motion, was also investigated.

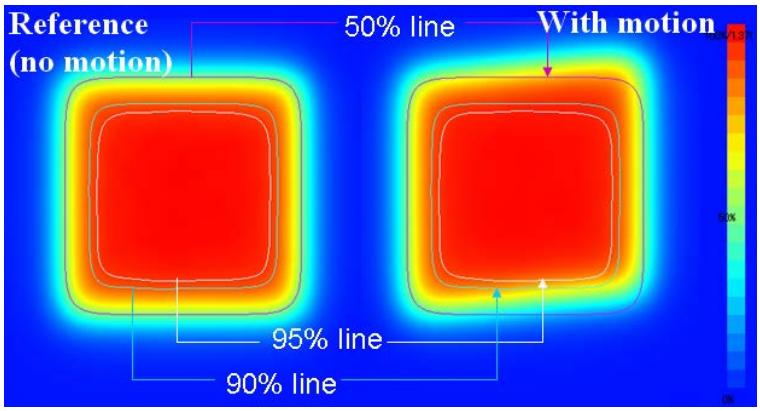

Figure 6- 8. Homogeneity calculation for the 95%, 90% and 50% isodose lines made on the reference (no motion) dose.

6.3 Results

6.3.1 Parallel scan direction

Figure 6-9 shows the 2D dose distributions acquired under each condition with the motion cycle = 3 s for various motion amplitudes and the number of paintings. 2D dose distributions for two different starting phases were shown for each condition. The right side of the figure shows the 2D dose distribution with 3 mm motion, extending to 5 mm, 10 mm and 20 mm motion. It is seen that the dose distribution is deformed with increment in the motion amplitude (right to left). The top row in figure 6-9 shows the measured data for a single painting, 169 spot delivery. For 3 mm motion, it appears that the dose distribution is nearly the same as the reference dose (no motion). For 5 mm motion (figure 6-10), there was some deformation seen on the peripheral area, and this became more apparent in the dose distribution for 10 mm motion. For 20 mm motion, not only peripheral dose deformation but also a hot spot (white spot in the figure) in the center of the dose distribution was observed. As the number of paintings was increased from the top to the bottom in figure 6-9 and 6-10, the dose deformations seen in the top of row on each figure were somehow blurred by repeating the spot delivery multiple times. The results for T=5 s motion were in total slightly better than

for T=3 s for each condition because slower platform motion showed less impact against the scan pattern.

Figure 6-11 shows the homogeneity ratio for each of the measured conditions and how the homogeneity ratios were quantitatively improved by the number of paintings for each phantom motion amplitude and breathing cycle. The worst and best values of homogeneity ratio caused by accounting for different starting phases were expressed for each condition on the graphs. The homogeneity ratios were compared for each 95, 90 and 50% isodose comparison based on the reference dose distributions.

The starting phase effect had a great impact on the dose homogeneity in the single painting for 20 mm and 10 mm object motion regardless of the motion cycle. However the starting phase effect was greatly compensated by the repainting. For the T=3 s motion results, the differences in the homogeneity ratio with single repainting were 11%, 15% and 18% for 95%, 90% and 50% comparison respectively. These differences reduced to less than 2~3% for all results from two times paintings. For T=5 s and 20 mm motion, the results of the starting phase effect were 13% 18% and 27% for each isodose comparison, and these were improved down to 10% for all cases. This result represented the worst result of the starting phase effect. Even in this case, the differences caused by the starting phase were less than 3% for two times paintings.

For a single painting, the homogeneity ratio was very sensitive to the motion amplitude. The homogeneity became worse with increment in the object motion. The average homogeneities taken between the + and – starting phase were minimum for each result; however, these were improved by repainting, and as a general trend, the homogeneities seemed to reach at a certain value from 8 times paintings for all results. The average homogeneity of 95% isodose comparison were over 0.97 for 20 mm motion and 0.99 for 10 mm motion for both 3 s and 5 s motion cycles. The 90% isodose comparison was above 0.95 for a 3 s cycle and 0.96 for a 5 s cycle for 20 mm motion, and above 0.99 for both 3 and 5 cycles and 10 mm motion. For the 5 mm and 3 mm motion, all results for homogeneity were above 0.98 regardless of number of paintings, motion amplitude and motion cycle.

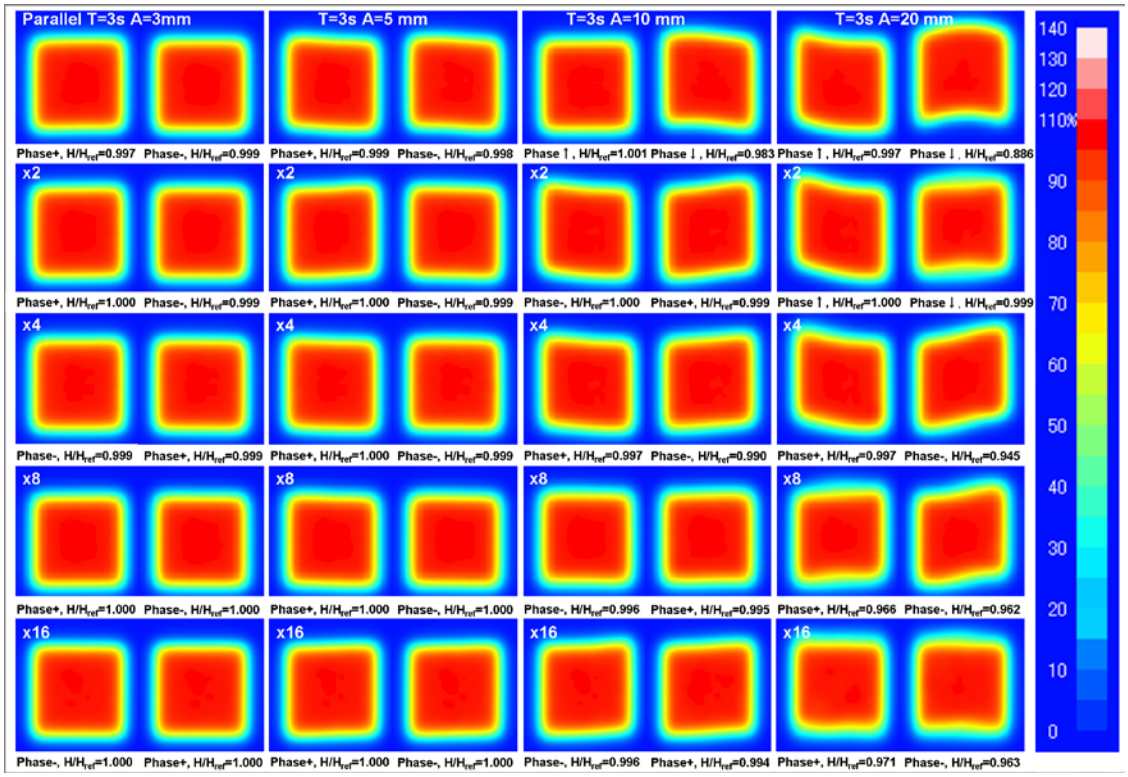

Figure 6- 9. Dose distributions for the parallel scan pattern with 3 s motion and amplitude of 3~ 20 mm (left to right) and various numbers of paintings (top to bottom). The phase + is defined as end-expiration phase (the platform position=0) and the phase – is defined inspiration phase (the plat form position= 3, 5, 10 and 20 mm). ↑ is the phase changing from phase - to phase +. ↓ is the phase changing from phase + to phase –. H/H_{ref} represents the homogeneity ratio of 95% isodose comparison for each condition.

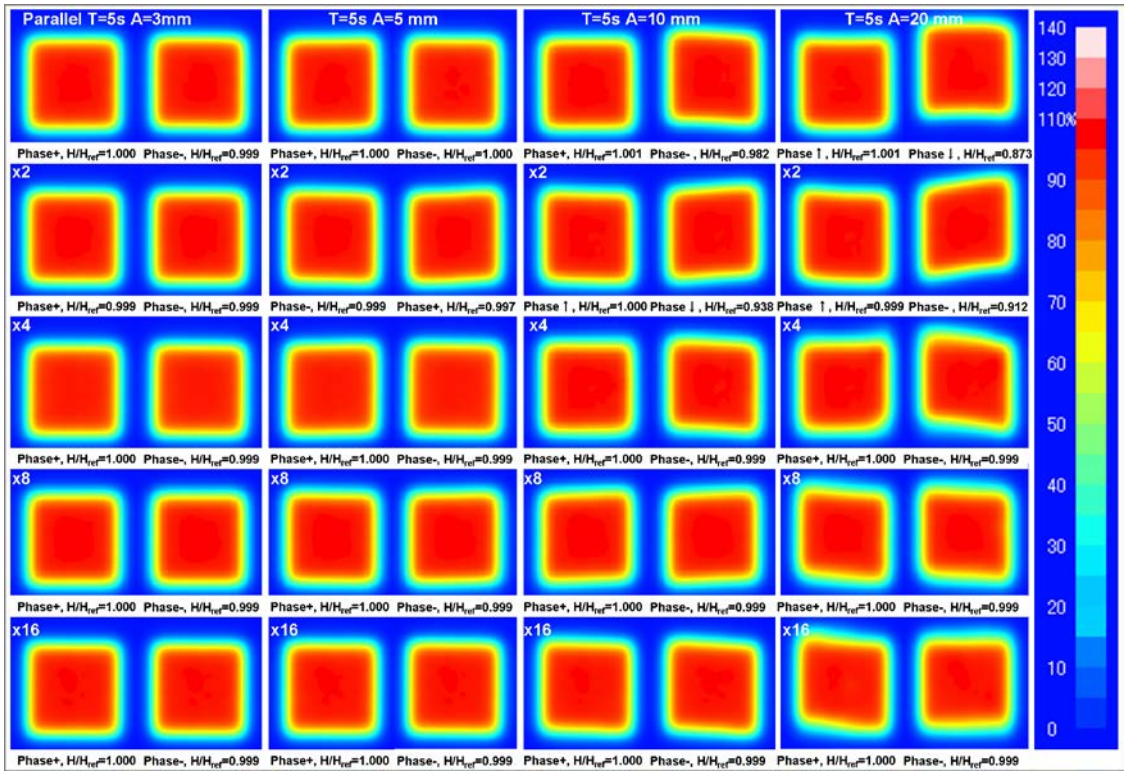

Figure 6- 10. Dose distributions for the parallel scan pattern with 5 s motion and amplitude of 3~ 20 mm (left to right) and various numbers of paintings (top to bottom).

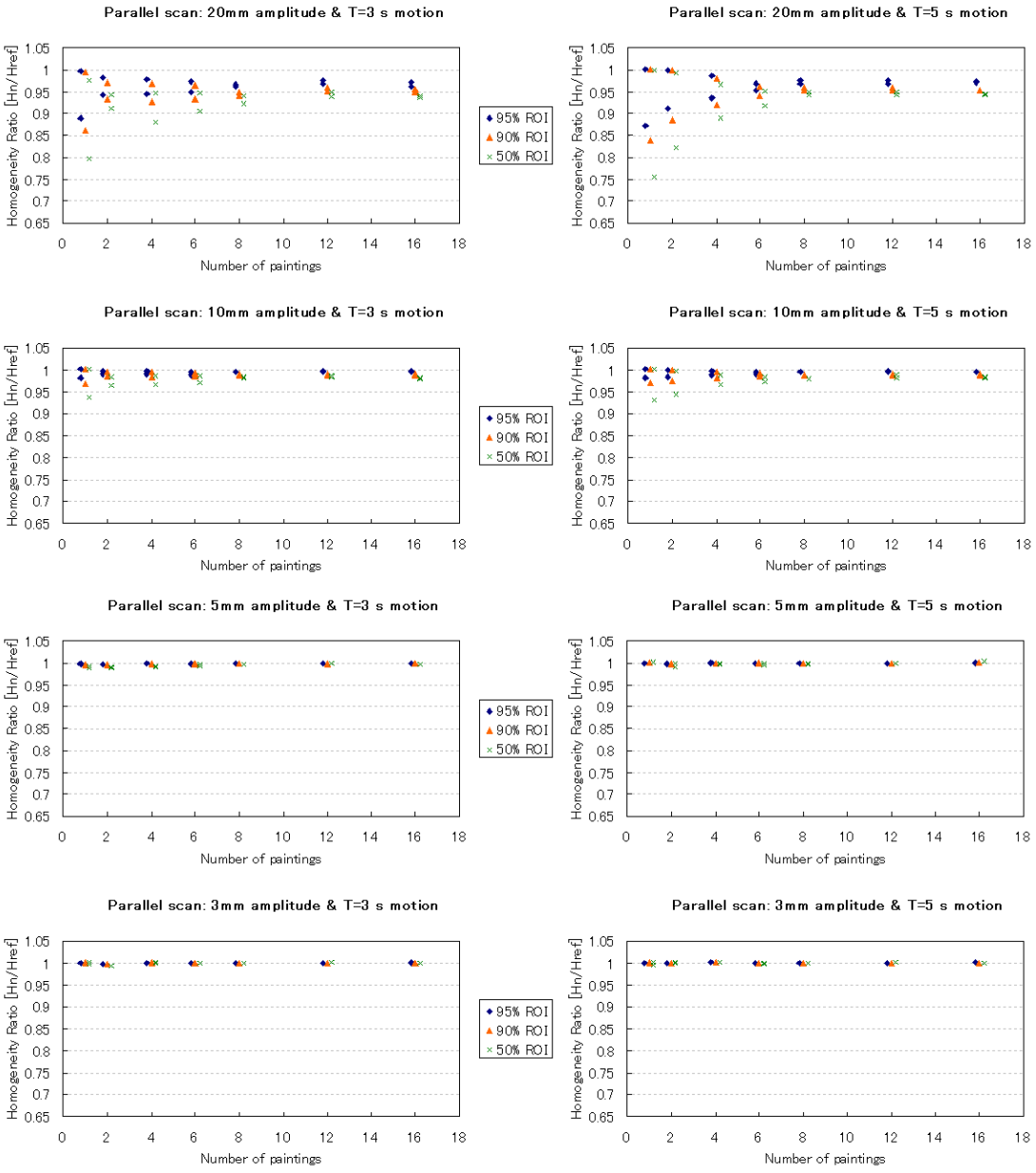

Figure 6- 11. Homogeneity ratio for the parallel scan pattern and the improvement caused by repainting for each motion pattern.

6.3.2 Orthogonal scan direction

Figure 6-12 and figure 6-13 show the 2D dose distributions for the orthogonal scan direction for a motion cycle of 3 s and 5 s for each. For the result of 3 mm motion, similarly there was no motion impact observed. For 5 mm motion, some dose non-uniformity and hot spots that were higher than the maximum dose on the reference dose distribution were observed, and the penumbra of the dose distribution in the SI direction became smeared out in the platform direction. For 10 mm motion, the dose distribution was skewed toward a certain location. The line-by-line scan pattern appeared to be synchronized with the object motion for a single painting (169 spot delivery). When the line by line scan was synchronized exactly with the object motion moving in the opposite direction, the change in dose distribution for 20 mm motion was seen as an oblique line inside of the dose distribution. Although the non-uniformity of the dose distributions for the orthogonal scan direction was quite different from the parallel scan pattern, the dose non-homogeneity was quite blurred by repeating the spot delivery multiple times.

Figure 6-14 quantitatively expresses the result of the dose distributions in figure 6-12. For the dose with 3 mm motion, the homogeneity ratio was above 0.98 for all isodose comparisons regardless of the number of paintings and degree of motion.

The homogeneity ratios of the dose distribution with the 5 mm motion were over 0.95 for any measured condition as well. From 10 mm, the differences in the homogeneity ratio due to the starting phase effect were not improved by repainting. The homogeneity ratios with orthogonal scanning were so sensitive to the motion that the homogeneity plots were deviated (scattered). Unlike the results for the parallel scan pattern, the starting phase effect was almost unavoidable regardless of the number of paintings. Although the average value of the homogeneity ratio for the result of 10 mm motion became gradually better by repainting, the homogeneity ratio was over 0.98 for the 95% and 90% isodose comparisons from 6 times paintings for both 3 s and 5 s cycle motion. For the result of 20 mm motion, similarly the average homogeneity ratio reached 0.95 for the 95% and 90% isodose comparisons with 3s cycle motion and 12 times paintings; however it was under 0.95 for 95% and 90% isodose comparisons with 5 s cycle motion.

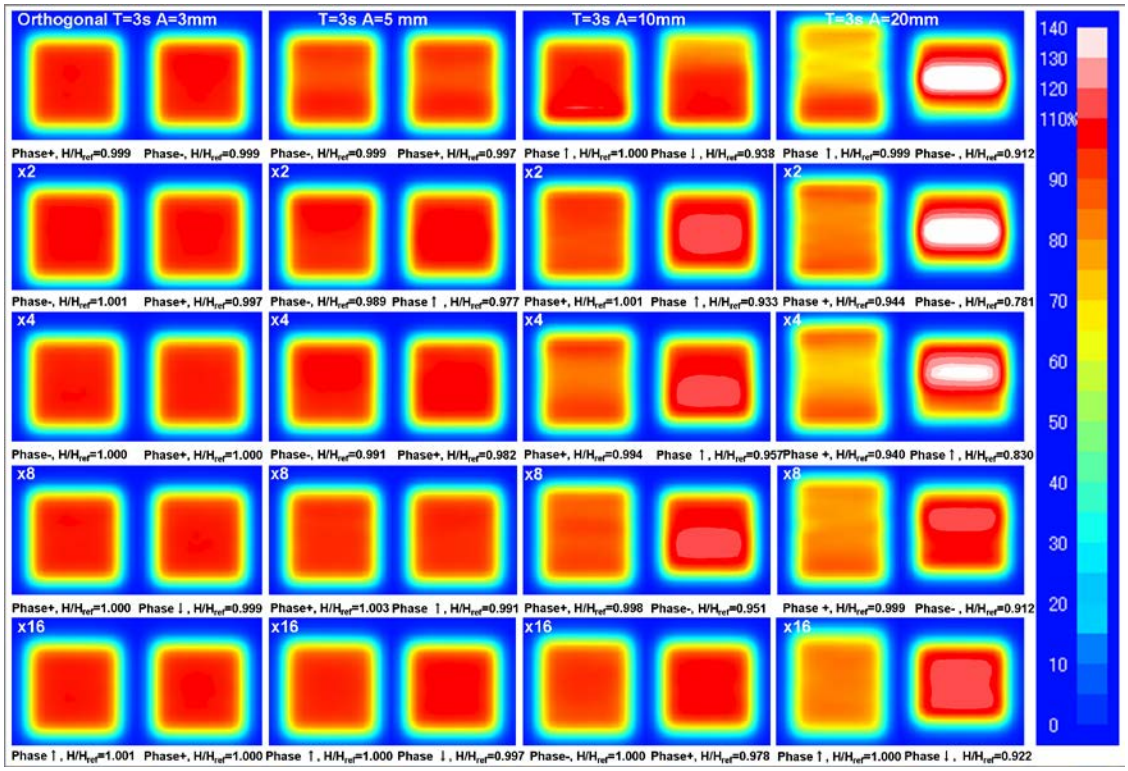

Figure 6- 12. Dose distributions for the orthogonal scan pattern with 3 s motion and amplitude of 3~20 mm (left to right) and its repainting effect (top to bottom).

The phase + is defined as end-expiration phase (the platform position=0) and the phase – is defined inspiration phase (the plat form position= 3, 5, 10 and 20 mm). ↑ is the phase changing from phase - to phase +. ↓ is the phase changing from phase + to phase –. H/H_{ref} represents the homogeneity ratio of 95% isodose comparison for each condition.

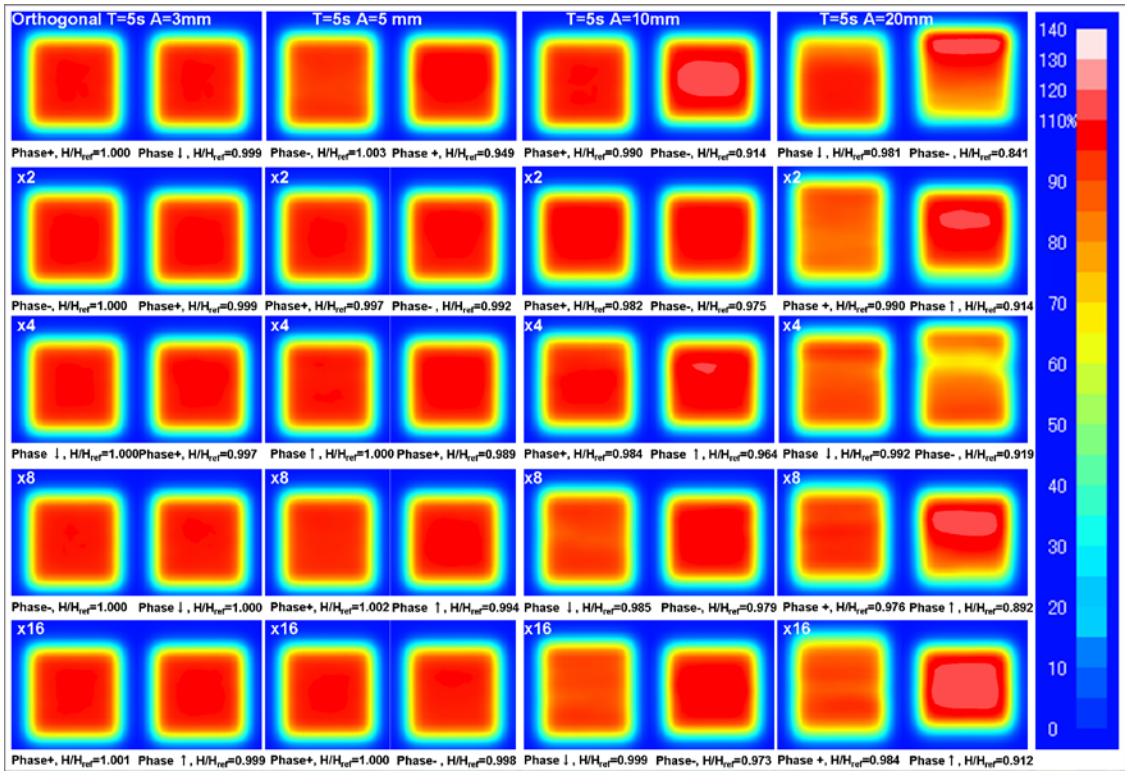

Figure 6- 13. Dose distributions for the orthogonal scan pattern with 5 s motion and amplitude of 3~20 mm (left to right) and its repainting effect (top to bottom).

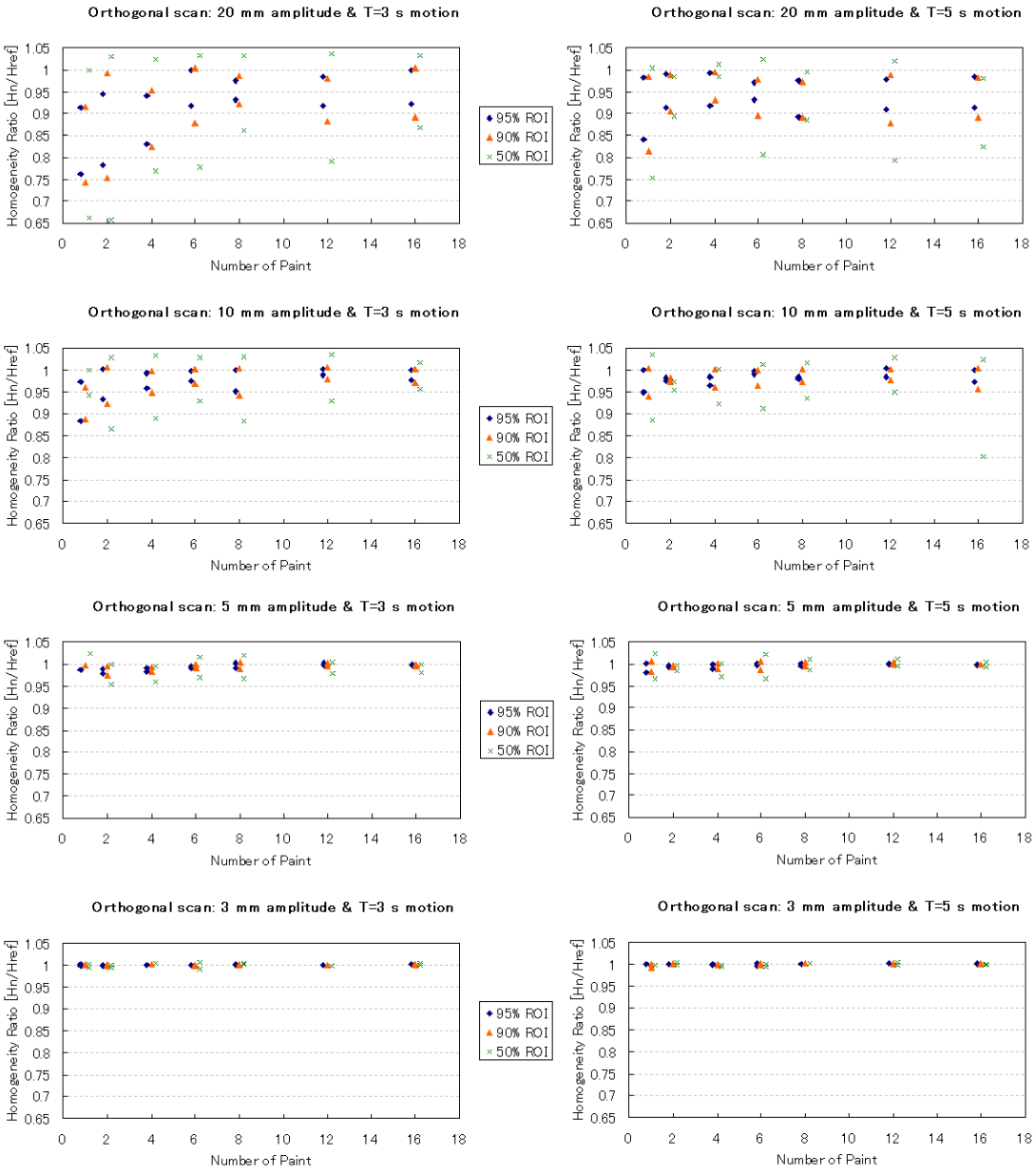

Figure 6- 14. Homogeneity ratio using the orthogonal scan pattern for each motion and the degree of improvement by repainting for each motion pattern.

6.4 Discussion

The proton beam scan pattern and the impact of the object motion on the scanned dose distributions were investigated for several conditions including the object motion patterns, motion amplitude and motion period. Dosimetric comparison between the parallel and orthogonal scan to the moving object showed that the parallel scan pattern achieved the better homogeneity, which was also improved by increasing the number of paintings up to 12 times. The number of paintings also improved the starting phase effect in the parallel scanning pattern. Figure 6-15 summarizes the dose homogeneity ratios shown in figures 6-9, 6-10, 6-12 and 6-13. Comparison of the dose homogeneity between the parallel scan pattern and orthogonal scan pattern were represented for 95% isodose comparison. Each point was the homogeneity ratio averaged over the starting effect for each condition, the number of paintings, the motion cycle and amplitude (20 mm and 10 mm only). The solid circle and square represented the homogeneity ratio for the parallel scan pattern with 3 s and 5 s motion cycles respectively. The open circle and square were similarly the homogeneity ratio of the orthogonal scan pattern with 3s and 5s motion cycle. These graphs clearly show that the homogeneity with the parallel scan pattern was always better than the orthogonal scan pattern. The dose homogeneity made by the parallel beam pattern was not influenced by the change in

the motion cycle. The variance of the dose homogeneity reached seemed saturated around 8 times paintings. The dose homogeneity of the orthogonal painting pattern was not as good as the parallel scan pattern, and was easily influenced by the object motion cycle. The difference seen for the orthogonal painting pattern between 3 s motion (open circle) and 5 s motion (open square) from 1 to 4 times paintings, which was not seen in the parallel scan results, became considerably minimized around 8 times paintings. This shows that the orthogonal scan pattern is more sensitive to not only motion amplitude but also the motion cycle than the parallel scan pattern. This was also improved somewhat by repainting. However, in this case, the difference could not be minimized as much as for the parallel scan. This trend was also seen for 10 mm motion.

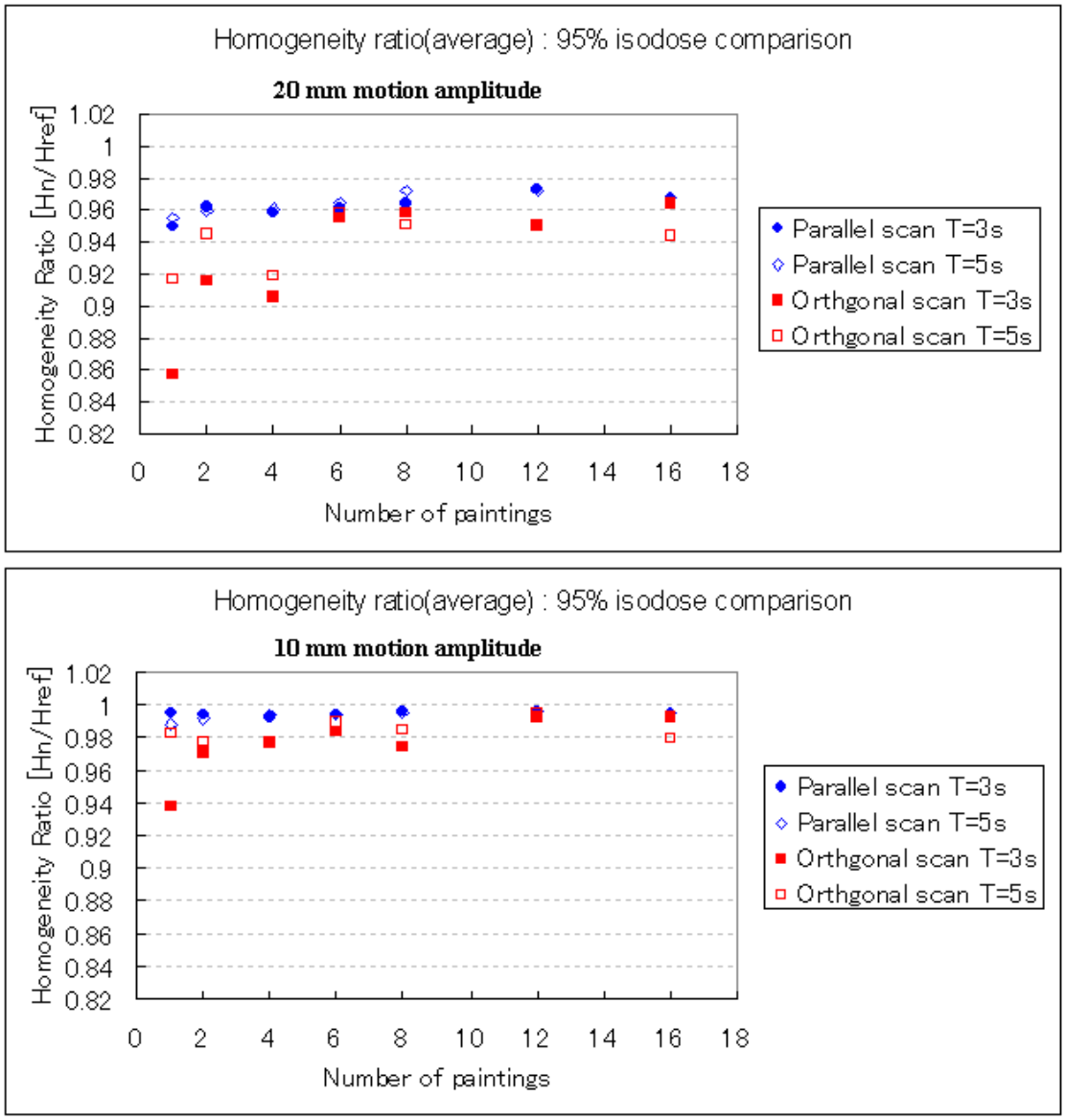

Figure 6- 15. Average dose homogeneity ratio for the 95% isodose comparisons. The solid circle and square represented the homogeneity ratio for the parallel scan pattern with 3 s and 5 s motion cycles respectively. The open circle and square were similarly the homogeneity ratio of the orthogonal scan pattern with 3s and 5s motion cycle.

Regarding the homogeneity ratio for less than 5 mm motion, as shown in figures 6-9 – 6-14, the homogeneity ratio of with-motion to without-motion (static: reference) was above 0.98 for all results in the parallel scan pattern and above 0.98 with 3 mm motion and above 0.95 with 5 mm motion in the orthogonal scan pattern. Based on the spot beam conditions in our facility, there is almost no difference in the dose homogeneity with the scan beam delivery to a moving and non-moving object (but the object is assumed to be composed of homogeneous water equivalent material).

Bert et al reported the dose homogeneities based on a single layer with a raster scanned carbon beam delivery to a moving phantom (2010). According to the dose homogeneity results, which were calculated based on a square field, the homogeneity ratio of each condition to the static homogeneity (no motion) was estimated to be approximately 80% for 20 mm motion and 93% for 8 mm motion. As compared with the homogeneity ratio obtained in this study, the homogeneity ratio of the 90% isodose comparison with 20 mm motion was above 92% for the parallel scan pattern and above 82% even for the orthogonal scan pattern. These values were single painting results, and the homogeneity ratios became better by repainting as shown in figure 6-15. The main reason for this difference is the spot size. Our spot beam size was 19.6 mm FWHM while their study used very narrow 6 mm FWHM. The important point from

this is that scanning beam delivery with a somewhat larger spot size may be more motion tolerant. In addition, an appropriate number of the paintings also make the beam delivery to a moving target more robust.

Knop et al (2011) investigated the treatment planning based interplay effect for proton spot scanning beam delivery to clinical targets using 4DCT patient data sets. The spot size used in this study was as half the spot size at PTCH and their investigation dealt with the interplay effect of volumetric targets. In spite these differences, the results obtained in this study support their results at least with respect to the data with the single beam field. The motion amplitude, beam delivery starting phase, scan direction and the need for repainting were very important factors to provide uniform dose distributions. Especially for the appropriate number of paintings, both studies showed that 1~ 4 times paintings did not guarantee improvement in the dose homogeneity or made it worse; however, for more than 4 times paintings, the dose homogeneity was successfully improved. Furukawa et al (2010) performed a study for carbon raster scanning with beam delivery under quite different conditions, and they also reported that the dose uniformity become close to a certain value in the standard deviation for 6 times paintings or more.

It should be noted that the results of the interplay effect obtained in this study were based on a 2D dose distribution, single layer (plane), using mono energy only, while Knop et al (2011) investigated the interplay effect with a volumetric target using a sharper spot beam. If the measurements performed in the present study were to be done three dimensionally, the results could be somewhat different. to the results could be similar to those for the mixed-phase layer-by-layer because our synchrotron needs approximately 2 s to change energy (layer) and the starting phase would differ layer-by-layer, which would case a more blurred dose distribution three dimensionally. Further experimental study is needed extend our present results to the more realistic case with volumetric and inhomogeneous structures more realistically representing patient anatomy.

The experiments undergone in this study focused on the interplay effect based on a single layer in water equivalent homogeneous material. The main drawbacks in this study are first of all that it did not account for the dose contribution from other layers or other beam energies and might represent a worse case of the interplay effect than a study with a volume target. Secondly this study did not account for the interplay effect in the beam depth direction because the density of the moving object was homogeneous. In a more heterogeneous case, for example in lung cancer, the water

equivalent path length to each planned spot position drastically varies due to inhomogeneous object motion, for which many spots pass through or cannot stop at the original planned spot position in beam depth as well as lateral beam position uncertainty. This also causes dose inhomogeneity in the depth direction and occurs spot-by-spot in spot beam delivery to moving inhomogeneous object.

Ideally in order to understand the interplay effect it might be possible to carry out the experiment undergone in this study using a human phantom. However, it might be very hard to analyze the dose distribution and how each cold and hot spot arise because so many spot beams with different energies coming from different positions are mixed and this is very confusing. As the scan pattern is more complicated for such a clinical case, it would be much more difficult to interpret the interplay effect. Thus, initial study of the interplay effect should be performed with a very simple scanning pattern and a 2D dose distribution on a single scan layer such as done in this study. Therefore, the experimental results obtained in this study provided very important information for basic comprehension of the interplay effect. This study could next be extended to volume scanning beam delivery to homogeneous and simple inhomogeneous objects composed of a few materials.

6.5 Conclusions

The impact of the motion on 2D dose distributions for a single energy layer was investigated by experiment. In the presence of motion, the delivered dose distribution was typically distorted and non-uniform. These dose inhomogeneities are related to not only the scan pattern but also the motion pattern e.g. motion amplitude and cycle. However, if the motion amplitude was less than 5 mm, there was less dosimetric impact (<2~5 % difference in homogeneity) regardless of motion cycle, number of paintings, and the beam starting phase conditions. However, if the motion was larger than 10 mm, these scan and motion conditions considerably affect the dose inhomogeneity. The worst cases were 17% and 7.2 % dose difference inhomogeneity for 10 and 20 mm motion amplitudes compared to the dose distribution with no motion. However, these dose inhomogeneities were improved up to 7.0% and 2.7% for 20 mm and 10 mm motion for each by repainting. These results serve as the basis for further interplay effect studies such as volume scanning in an inhomogeneous object. It might be also directly applicable for a clinical case with a target whose beam path is composed of nearly water equivalent materials. Furthermore the results in this study propose that the respiratory gating technique is needed for scanning beam delivery to a moving target with motion amplitude > 10mm.

Chapter 7. Specific aim 2: Beam scanning delivery Part II

Assess the accuracy of dose delivery in respiratory gated proton therapy in scanning beam delivery: A verification experiment of respiratory gated spot scanning beam delivery

7.1 Introduction

The interplay effect study discussed in the previous chapter showed that for scanning beam delivery motion less than 5 mm can be ignored. However, when motion is 1 cm or greater, the dosimetric impact due to motion causes a dose deterioration and the dose homogeneity depends both on the number of paintings and the scan direction. Employing a respiratory gating beam delivery technique for the case of the motion larger than 1 cm in spot scanning mode may improve dose homogeneity and help to mitigate the effects of motion.

The main concern about employing respiratory gating techniques into a synchrotron based beam delivery system is first, if all spots cannot be delivered within one respiration gate, there could be a lack of continuity of the relative spot and target positions between the phase when the beam delivery has stopped in the previous gate and the phase when the next beam delivery will start in the next breathing gate. This is

in principal caused by a specific synchrotron issue in that a spill extracted from a synchrotron is not always ready when the respiratory gating system becomes ready to start beam delivery. In other words, the spill delivery can be initiated randomly within the respiratory gate-on status. The interplay effect was the main concern in the previous chapter, but in this chapter the interplay effect between respiration gates on one layer scan is more important in synchrotron based respiratory gated spot scanning beam delivery. The interplay effect may also affect the volumetric dose distribution and even the 2D dose in the case that the multiple painting cannot be completed within one respiration gate.

In this section, the purpose is to investigate the feasibility of respiratory gated beam delivery for synchrotron based spot scanning by experiment. The experiment and dosimetric comparison performed in previous chapter were repeated with respiratory gating.

7.2 **Materials and Methods**

The equipment, procedure and analysis performed for these measurements were the same as in the previous chapter. For details of the measurements, one should refer to the **Materials and Methods** in the chapter 6-2. Additional equipment newly used for the respiratory gating experiment is explained below.

7.2.1 Respiratory gating system

The respiratory gating system was developed for this study. It is composed of a laser displacement sensor (ZS-LDS2VT, Omron, Japan) and a control unit (figure 7-1a). The laser sensor measures the distance from the sensor to the surface of an object. The control unit is mainly composed of an AD converter and digital signal circuits for generating a gate signal. It converts and transfers the signal from the laser sensor to a laptop PC. In-house software displays the signal from the control unit in a frame ratio of 100 ms (figure 7-1b). The gate-on threshold level can be variable, and under the gate threshold level the software sends a gate signal to ZENKEI via the control unit. The mechanical delay of the gate signal between the software and the control unit is less than 10 ms (figure 7-1c).

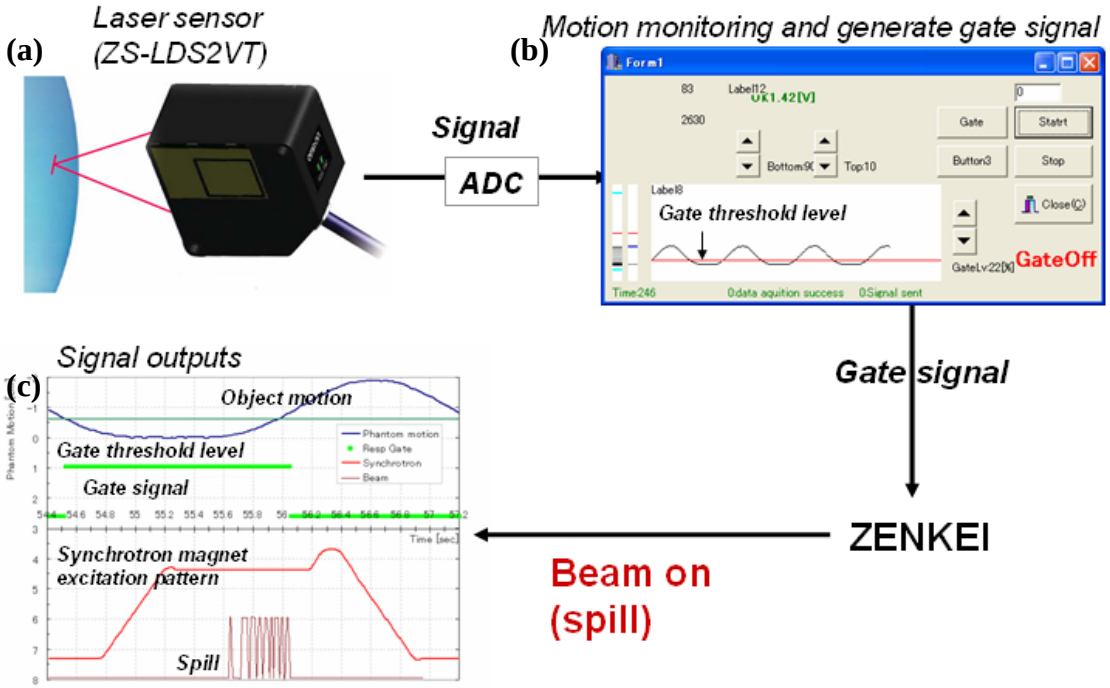

Figure 7- 1. System outline of the respiration gating unit and software.

7.2.2 Setup for measurements with the respiratory gating unit

Under the same setup condition as in the previous chapter, the laser sensor was set near the edge of the moving platform in the direction of platform motion (figure 7-2). Since the moving phantom, 2D chamber array and the solid water phantom move together in rigid motion, there is no difference where the laser sensor measures in the part of this unit. When the platform moves, the sensor measures the distance from the sensor to a certain point on the platform. This dynamically changing distance was measured as platform motion and displayed on the software.

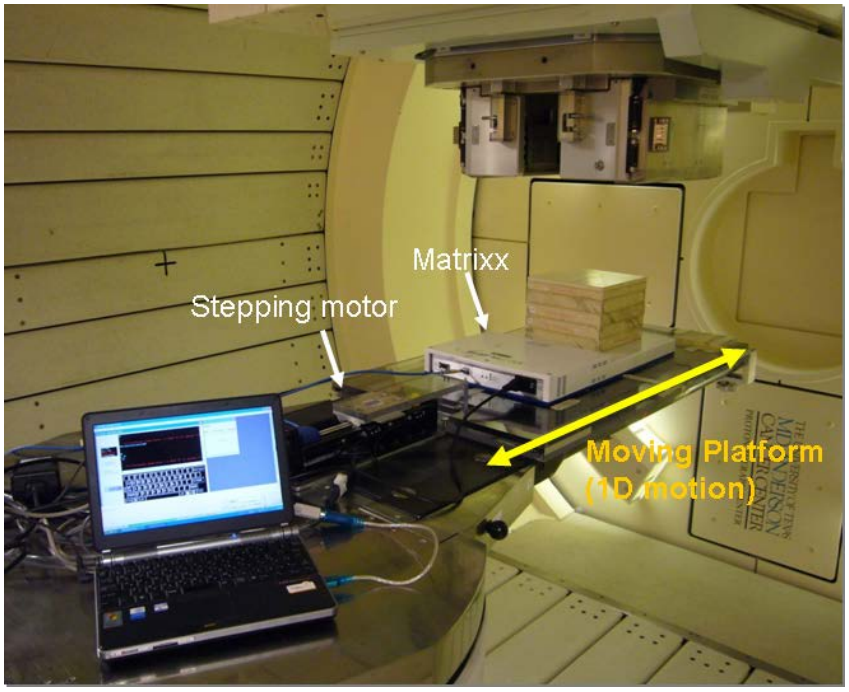

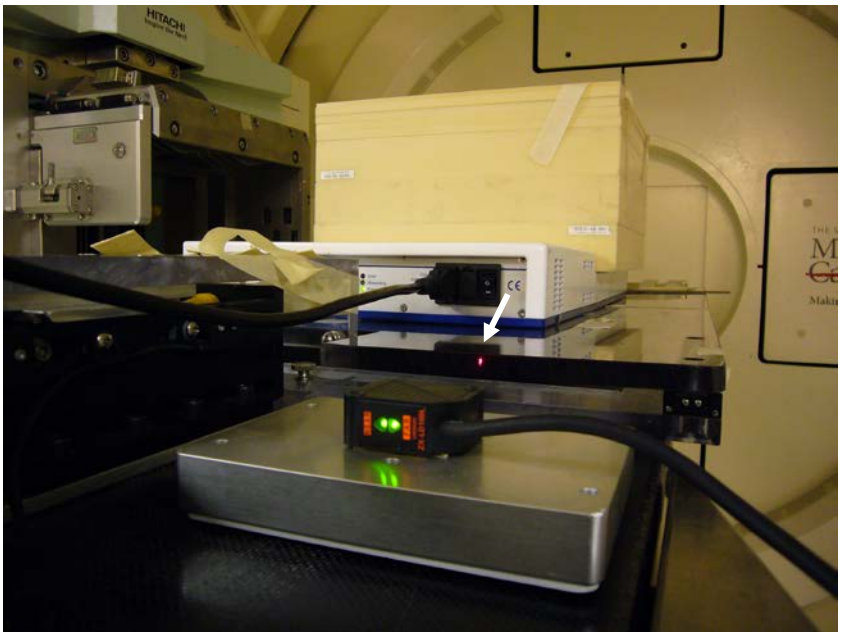

Figure 7- 2. Setup of the laser sensor in the measurement. The upper image is an overview of the setup of the equipment. The lower image is the setup of the laser displacement sensor, which measured the distance between the edge of the moving platform (red spot seen on the image at the arrow) and the sensor.

7.2.3 2D dose measurement

Information concerning the spot beam, conditions and procedure for the measurement were same as in the previous chapter except for platform motion. The same measurement was repeated with respiratory gating and it was compared with the results without gating. This is summarized in table 7-1. Regarding the platform motion, the same sinusoidal motion following the formula (formula 2-1 in the chapter 6) with n=4 was used and the cycle of the motion was also same and used, T= 3 s and 5 s; however, the amplitude of the platform motion was fixed with 20 mm motion. In this situation, the end-expiration phase corresponds to the platform position at y=+0, where the center of the 2D chamber array detector was set at isocenter, and the end-inspiration phase corresponds to y= -20mm, at the inferior position in the treatment couch coordinate system explained in figure 7-3. Based on the 20 mm motion amplitude in the SI direction, the respiratory gate level was set at 30% in the expiration phase (figure 7-3). The platform motion under the 30% gate level, or the intra-fractional motion under the gate level, was approximately 6 mm. The gate width for T=3 s and 5 s cycle of the sinusoidal motion was 1.1 s and 2.4 s for each. In principal, it is impossible to complete one painting, including delivery of 169 spots, in T=3s motion. On the other hand, it is probably possible to complete it in 5 s motion; however, this

depends on when the beam delivery starts during the gate-on status. This is a synchrotron specific problem with the respiration gating and depends on the specification of synchrotron manufactured by each vendor.

This measurement focused on the dosimetric impact of such inter-play effect within the 6 mm motion and interplay effect under the conditions listed in table 7-1.

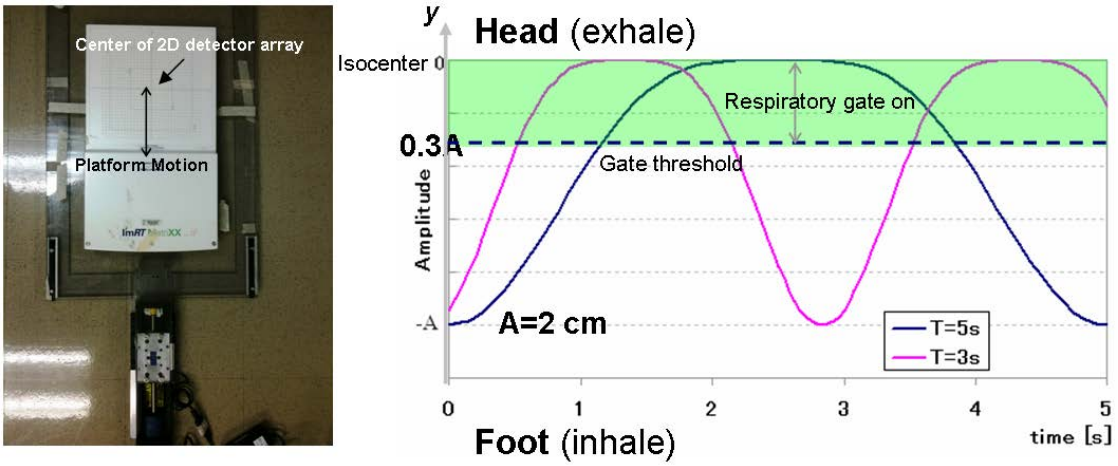

Figure 7- 3. Platform motion (sinusoidal motion) pattern and respiration gate setting. The center of the 2D array ion chamber detector was set at the isocenter. Note that the end-expiration position is set to y = 0, and the end-inspiration level at y = -2 cm.

Beam information	
Energy [MeV]	173.7 (200 mm in water)
Measured Depth [mm]	195 in water (equivalent to ≈95% dose)
Spot size [FWHM mm]	19.6
Spot Spacing [mm]	8
Spot delivery time	4 ms delivery
	3 ms to move to next spot position
Scan field [cm2]	10x10
Number of spots	13x13=169
Time for single painting [s]	1.18
Moving platform	
Motion	$\sin^4$
Motion amplitude[mm]	20
Motion cycle[s]	3 and 5
Respiratory gate condition	
Gate level	30%
Motion under the gate level[mm]	6
Gate duration time [s]	1.1 in T=3s motion
	2.4 in T=5s motion
Measurement: Beam delivery	
Number of paintings	1, 2 ,4 , 6 , 8 , 10 , 12
Scan direction	Orthogonal (to moving platform)
	Parallel

Table 7- 1. Measurement conditions.

7.2.4 Analysis

The 2D dose distribution with motion was normalized based on the absolute dose at the center of the reference 2D dose. The relative 2D dose distributions obtained under each condition were compared by means of the dose homogeneity ratio, H_n/H_{ref}, where H is the dose homogeneity. This is the ratio of the dose homogeneity with gating (with motion) to static (no motion) for each number of paintings (*n*). Details of dose homogeneity were explained in the previous chapter. The dose homogeneity was calculated inside of three types of regions of interest (ROI)s, including the 95%, 90% and 50% isodose lines, ROI_{95}, ROI_{90} and ROI_{50}, which were based on the reference dose distribution (static, no motion) for each beam delivery condition (number of paintings, *n*, and parallel or orthogonal scan pattern). H_{ref} was computed inside of each ROI, and H_n for each beam delivery condition was also calculated inside of the same geometric area of each ROI (figure 7-4).

The homogeneity ratio $Hn/H_{ref}=1$ means that there is principally no difference in the dose homogeneity between the 2D dose distribution with gated (with motion) and static (without motion) beam delivery, where the static dose distribution is the reference. In other words, in this case there would be no dose deterioration caused by motion.

7.2.5 Starting phase

In the free breathing based interplay effect study, the beam delivery starting phase was a very relevant factor influencing the dose distribution. With respect to the respiratory gating mode, beam delivery ideally was controlled under a certain phase of object motion. Based on the current situation for respiratory gating, unfortunately, it is technically impossible to initiate beam delivery precisely even at the gate-on phase (under the gate threshold level). Therefore different types of beam delivery were attempted in this set of measurements: for one, beam delivery was initiated within the first half of respiration gated-on status, and thus beam delivery started in <1/2 of the gate-on duration. Another was beam delivery starting in the latter half of the gate-on status. The measurement was repeated several times at different phases among these early and late phases, and maximum and minimum homogeneity ratios were interpreted in the Results section.

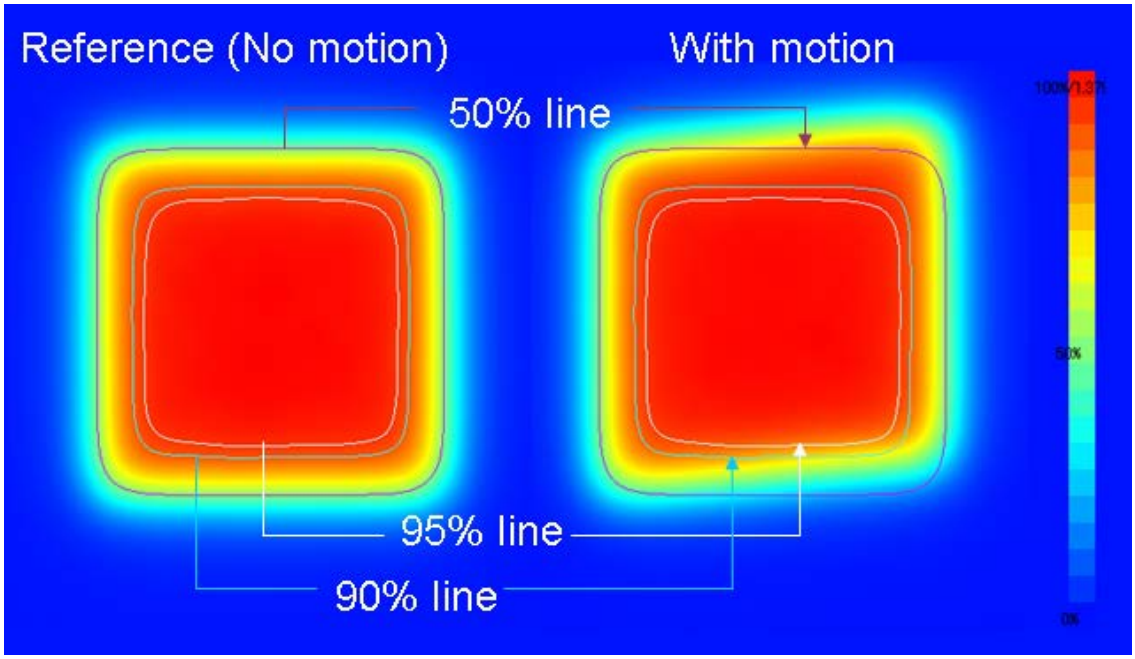

Figure 7- 4. Schematic overview of the homogeneity calculation on each ROI, including ROI_{95}, ROI_{90} and ROI_{50}. Each ROI was made based on 95%, 90% and 50% isodose lines on the static (no motion) dose distribution (left), named the reference dose distribution. The homogeneity, H_{ref}, of the reference dose distribution was computed inside of these ROIs. These ROIs were superimposed on each gated 2D dose distribution (with motion, right) and the homogeneity, H_n (n: number of paintings) was then calculated.

7.3 **Results**

7.3.1 2D dose measurement

7.3.1.1 Scan pattern parallel to the platform motion with respiratory gating

Figure 7-5a shows the 2D dose distributions measured with a parallel scan pattern in a single painting (13 lines × 13 spots = 169 spots) with respect to a 3 s motion cycle and the signal outputs recorded during beam delivery. Figure 7-5b shows the signal outputs of object motion (laser sensor), gate-on trigger, synchrotron magnet excitation pattern and spill, or spot delivery (RF-on for beam extraction). Based on the signal information, the actual delivered spot positions were approximately re-assigned on the map assuming a 2D array detector (figure 7-5c). The completion of 169-spot delivery needed tow spills in this case. As shown in figure 7-5b, the object position (expressed as the motion amplitude, cm) at the end of the first spill was quite different from the object position at the beginning of the next spill. The first spot in the second spill (figure 7-5c, red circle) was not delivered at the correct position that was supposed to be next to the end of the last spot in the first spill (blue circle in figure 7-5c), there was gap of approximately 6 mm between the spills. This caused a cold spot seen in the middle of the field in figure 7-5a. During spot beam delivery in each spill, the object motion influenced the dose distortion especially seen on the top and bottom peripheral

regions. However, there was no continuity between these dose distortions between the spills. This consequently generated the winding distortion shape in the top and bottom penumbras. The dose distortion occurring in each spill was associated with the intra-spill object motion, and the cold (or hot) spot and the discontinuities in the dose distortion were associated inter-spill object position error. This effect was considerably influenced by the number of paintings, and the dose distortion and cold (hot) spots were barely visible with 4 times paintings. Figure 7-6 shows the impact of multiple paintings on the distorted 2D doses.

7.3.1.2 Scan pattern o*rthogonal to the platform motion with respiratory gating*

Figure 7-7 shows the 2D dose distributions measured with the orthogonal scan pattern in single painting with respect to a 3 s motion cycle (figure 7-7a), the signal outputs recorded during beam delivery (figure 7-7b) and the reassigned delivered spot position (figure 7c). Contrary to the results for the parallel scan pattern, figure 7-7c showed that not only the shift between scan lines caused by the motion but also the position of the individual spots in the scan line was considerably influenced by the motion. The scan line ran obliquely in the worst case of intra-spill object motion. In addition, the spot position error due to inter-spill object motion uncertainty occurred between the end of

the first spill and the beginning of the second spill. The unbalanced delivered spots shown in the middle of the field (0<y <2 cm) seen in figure 7-7c reflected on the hot and cold spots in figure 7-7a. The cold and hot spots caused by both intra- and inter-spill object motion were more sensitive than the results for the parallel scan pattern. Figure 7-8 shows the impact of the multiple times of painting (re-painting) on the intra- and inter-spill motion effect. The dose distribution was not smeared as well as with the parallel scan pattern, which is seen even in dose distributions for 8 times paintings or more.

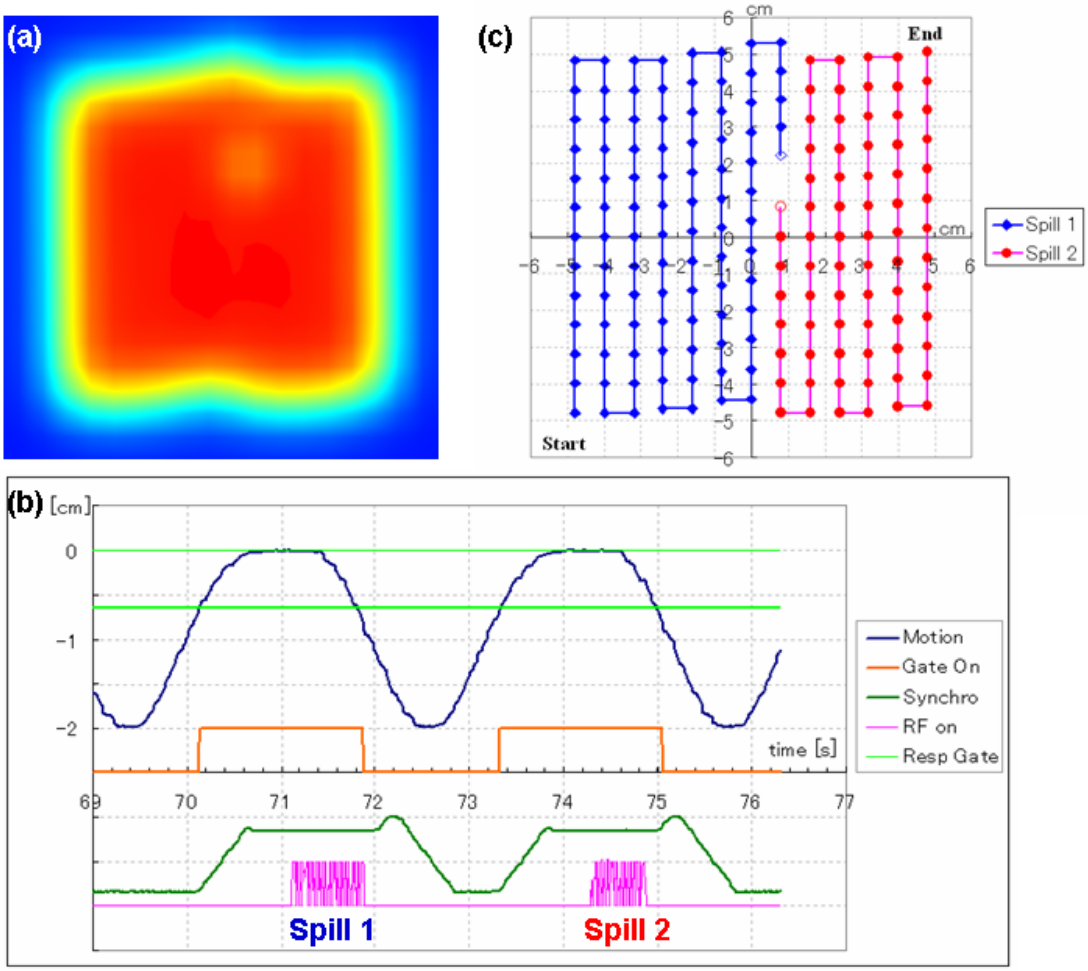

Figure 7- 5. Result of single painting in the parallel scan direction and signal outputs during beam delivery. (a) The measured 2D dose distribution in the case of a 3 s motion cycle. (b) The signal output of the moving platform (blue), respiratory gate status (cm, orange), gate threshold (arbitrary units, light green), synchrotron magnet excitation pattern (arbitrary units, dark green) and RF kicker for beam extraction: indirectly expressing spill beam extraction (arbitrary units, pink). (c) Based on the signal outputs, the actual delivered spot positions were reassigned on the map.

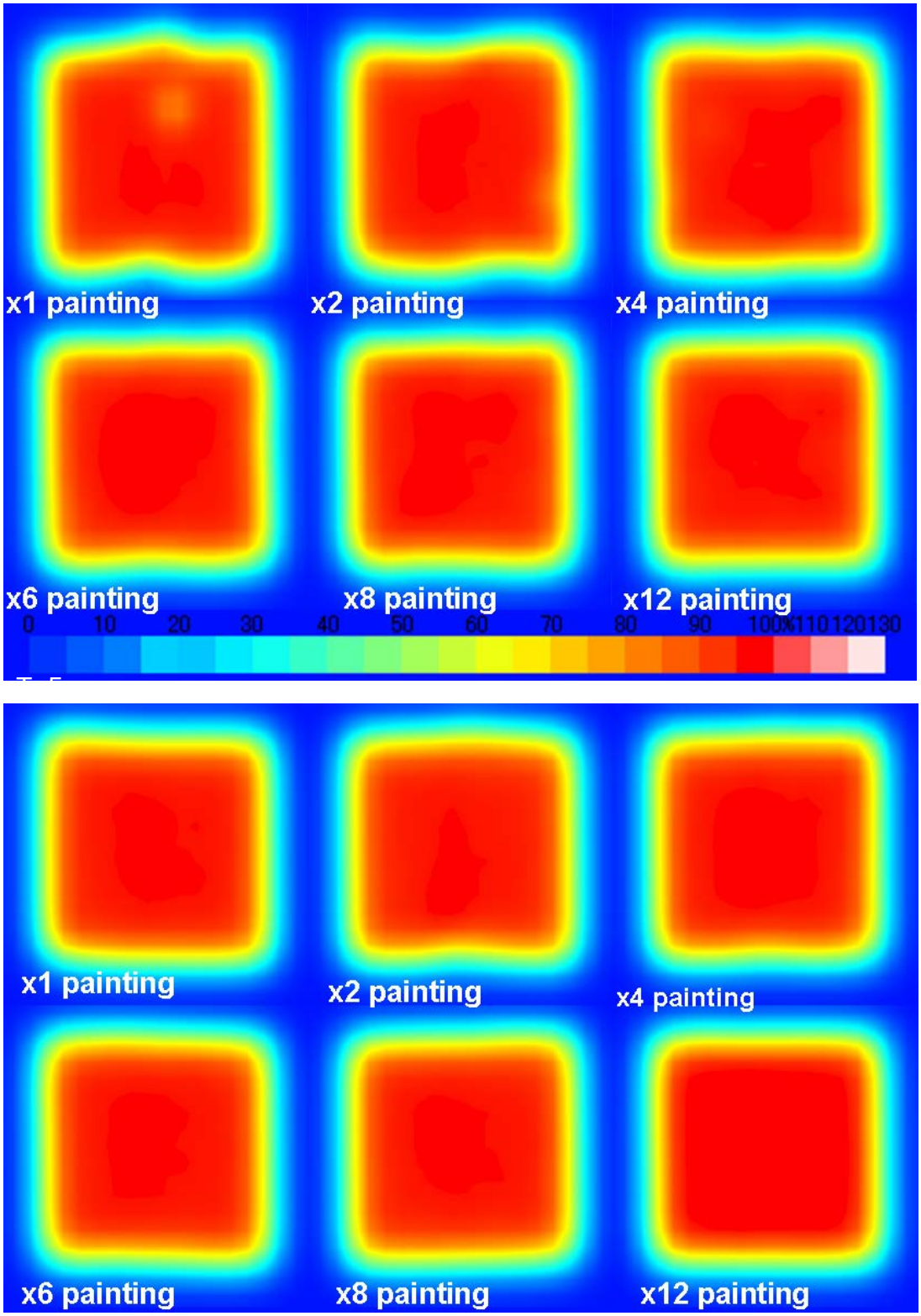

Figure 7- 6. Dose distribution with the parallel scan pattern (x1~12 paintings) with a 3 s motion and gating (upper) and a 5 s motion cycle (lower).

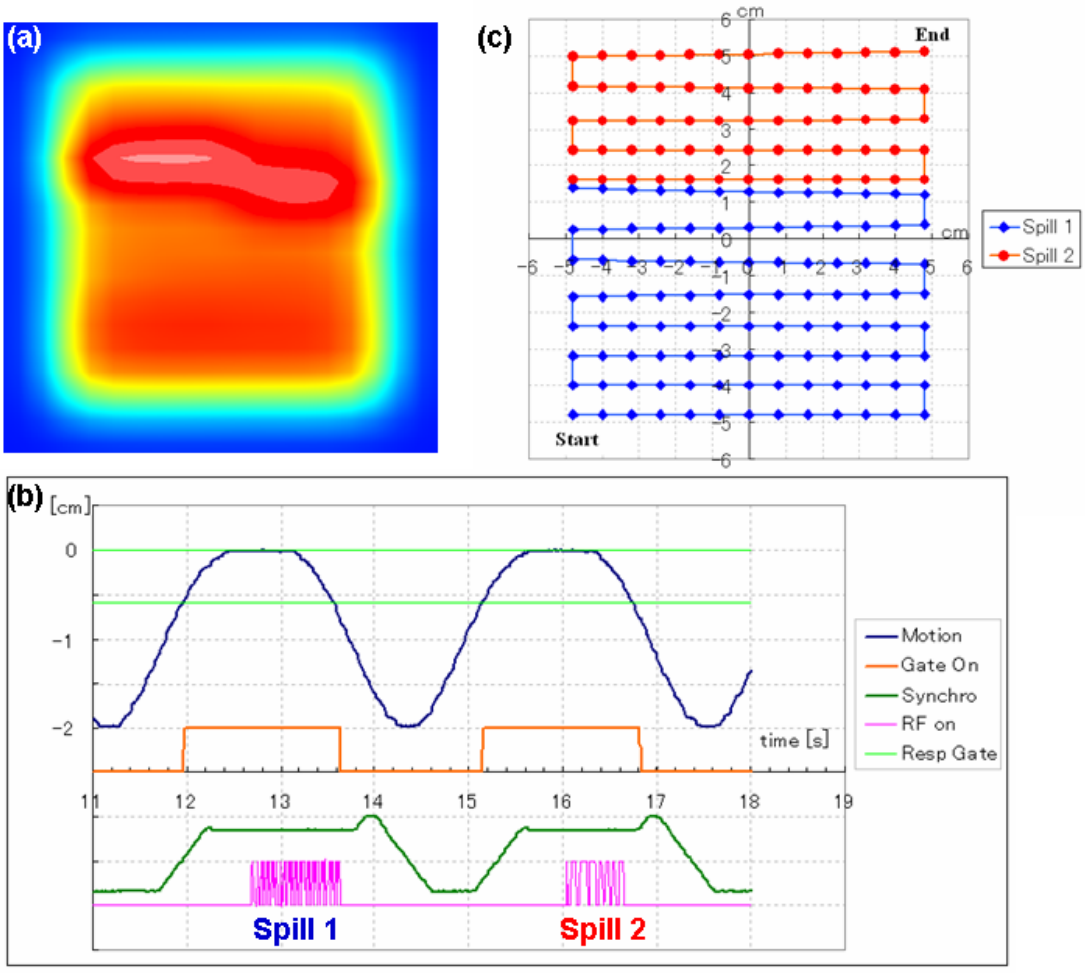

Figure 7- 7. Result of single painting in the orthogonal scan direction and signal outputs during beam delivery. (a) The measured 2D dose distribution in the case of 3s motion cycle. (b) The signal output of the displacement of the moving platform (cm, blue), respiratory gate status (arbitrary units, orange), gate threshold (light green), synchrotron magnet excitation pattern (arbitrary units, dark green) and RF kicker for beam extraction: indirectly expressing spill beam extraction (arbitrary unit, in pink). (c) Based on the signal outputs, the actual delivered spot positions were reassigned on the map.

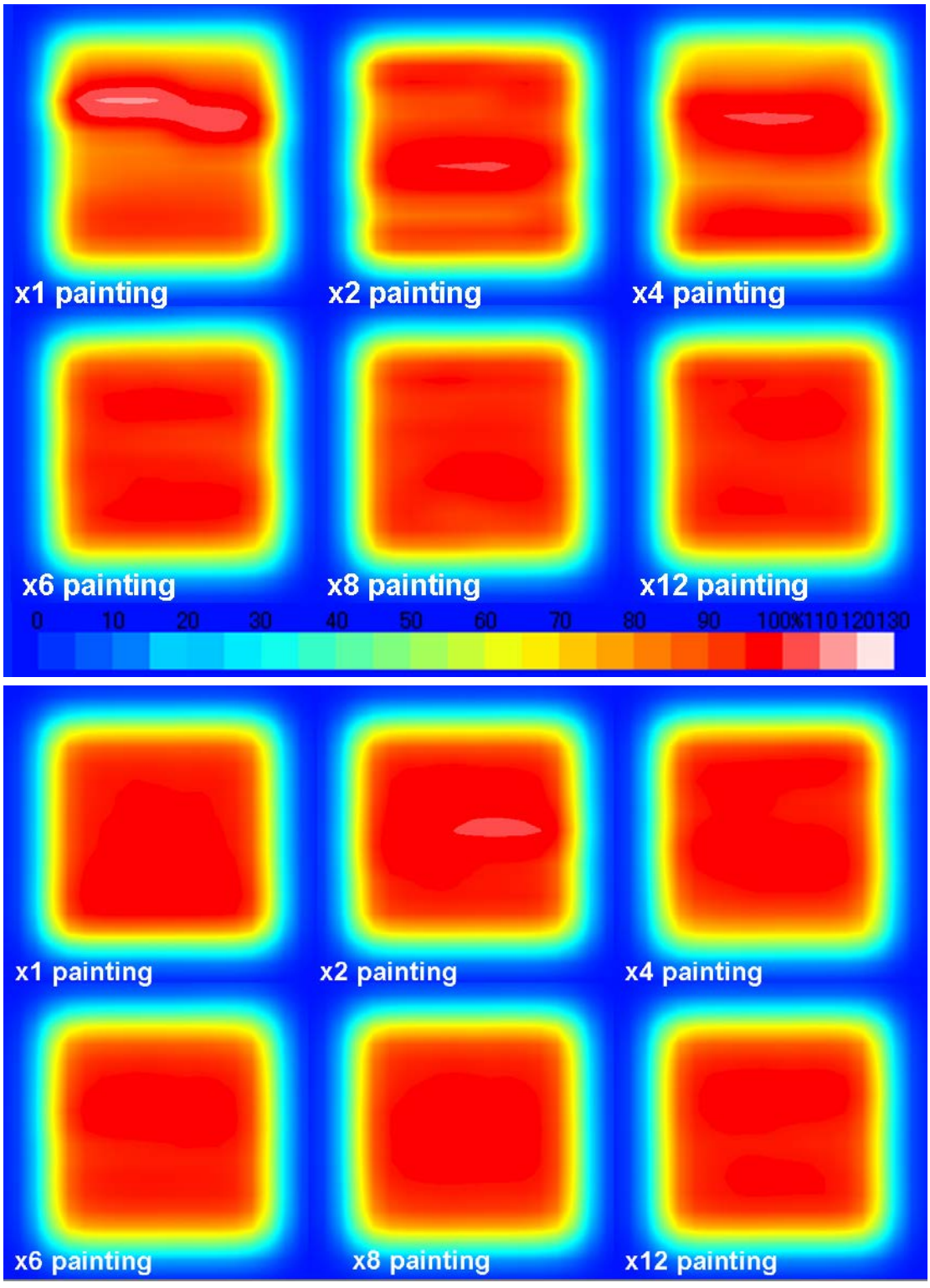

Figure 7- 8. Dose distribution with the orthogonal scan pattern (x1~12 paintings) with 3 s motion and gating (upper) and a 5 s motion cycle (lower).

7.3.2 **Analysis: Dose homogeneity**

7.3.2.1 Parallel scan direction beam delivery with respiratory gating

The measured 2D dose distributions and the dosimetric impact of the number of paintings for each motion cycle shown in figures 7-6 (a) and (b) were compared with respect to the dose homogeneity ratio for each motion cycle in figures 7-9(a) and (b). Since the reduction in the homogeneity ratio accounting for the starting phase effect was below 1% for all results, only the worst results were plotted on each graph. Both graphs show all the homogeneity ratios, Hn/H_{ref}: the dose homogeneity ratio of gated motion to no motion, were above 0.98 for each isodose comparison regardless of the number of paintings in the parallel scan pattern and both object motion cycles. The homogeneity ratio for a single painting shown in figure 7-5 was worse for the 95% (ROI95) and 90% (ROI90) isodose comparison than for the 50% (ROI50) isodose comparison due to the appearance of cold spots and the distortion around the penumbra. This should not imply that the dose homogeneity was improved, however. In the 50% isodose area the homogeneity ratio was conversely increased by the high dose distribution contributing the penumbra reason due to the distortion. Except for the case of a single painting, there was a 2% difference in dose homogeneities between the gated and static dose distributions for all isodose areas of both motion cycles

(σ=0.15%). There was a dosimetric impact caused by the intra-spill object motion and inter-spill object position uncertainty with respiratory gating; however it was less than 2% for more than two times paintings for the parallel scan pattern. It is noted again that even for a single painting, the homogeneity ratio was above 0.98.

7.3.2.2 Orthogonal scan direction beam delivery with respiratory gating

Figure 7-10 showed the homogeneity ratio of the 2D dose distributions shown in figure 7-8. Since the results including the starting phase effect made some differences in the same measurement conditions, the graphs of the homogeneity ratio for the motion cycle of 3 s (upper) and 5 s (lower) showed the worst and best results plotted for each number of paintings. As seen in figure 7-8, the hot and cold spot yield influenced the dose homogeneity in the high dose areas. The worst homogeneity ratios for ROI_{95}, ROI_{90} and also ROI_{50} were below 0.95.

For the homogeneity ratio with a 3 s motion cycle and 2 times paintings, ROI_{95} and ROI_{90} were still below 0.95 in the worst case. However this gradually improved from four paintings and became above 0.96 and finally above 0.98 from 8 paintings. In addition, the starting phase effect was also minimized with a 1%

difference between the best and worst results except for the result of ROI_{95} and 6 paintings.

For the homogeneity ratio with 5 s motion, the starting phase did not have as much influence on the results of 3s after 2 paintings. The homogeneity ratio for all cases was also above 0.96 and reached 0.98 for 6 paintings. There was a slight difference in the dose homogeneity associated with the speed of the platform motion for 1-4 paintings.

The impact of the starting phase still had an influence on the dose homogeneity due to production of cold and hot spots. Over 6 times paintings, the homogeneity ratio become above 0.98 and there were almost no differences in dose distributions between motion for both 3 s and 5 s with gating and no motion. In addition the impact of the starting phase effect could be ignored with re-painting. The dosimetric impact caused by the intra-spill object motion and inter-spill object position uncertainty with respiratory gating became minimized and maintained consistency for more than 6 times paintings in the orthogonal scan pattern to the object motion.

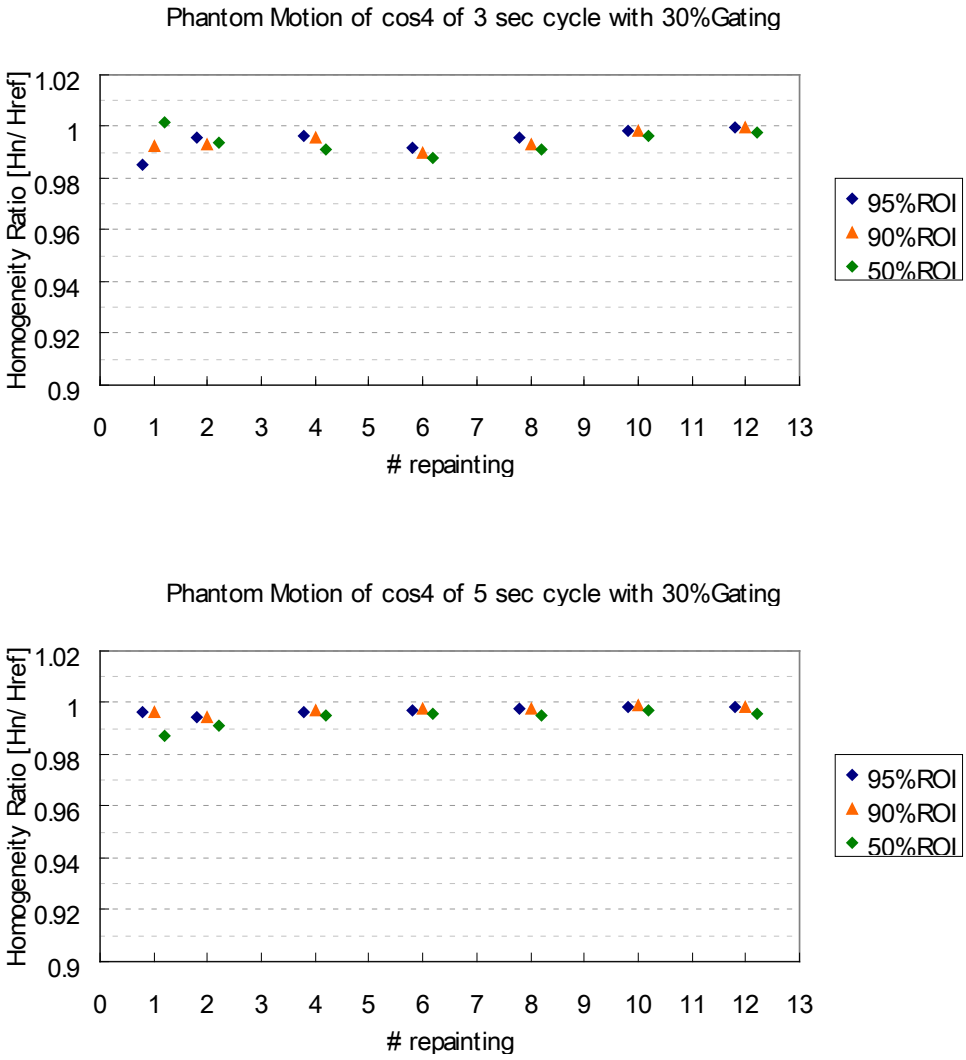

Figure 7- 9. Homogeneity ratio with the orthogonal scan pattern for 3s (upper) and 5s (lower) motion cycle and its improvement by re-painting for each motion pattern. Each plot of the homogeneity ratios of the 95%, 90% and 50% ROIs for each number of paintings was slightly shifted to avoid overlap for each number of paintings.

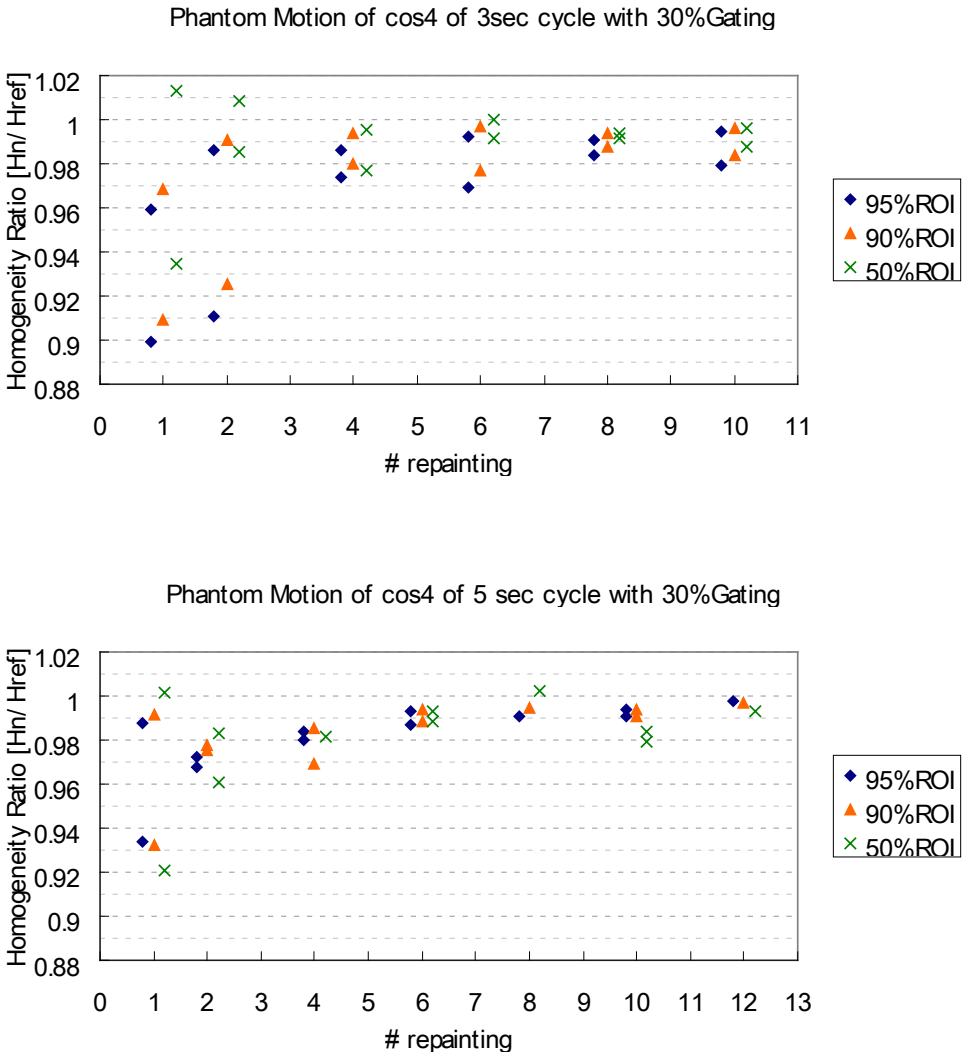

Figure 7- 10. Homogeneity ratio by orthogonal scan pattern for 3 s (upper) and 5 s (lower) motion cycles and its improvement by re-painting for each motion pattern. The worst and best homogeneity ratios were plotted for each condition (two plots for each condition). Each plot of the homogeneity ratios of the 95%, 90% and 50% ROIs for each number of paintings was slightly shifted to avoid overlap for each number of paintings.

7.4 **Discussion**

The experiments performed in this study examined the dosimetric impact caused by use of respiratory gated spot beam delivery to the moving object. The concern in this experiment was the dose deterioration and loss of homogeneity due to the intra-spill object motion and inter-spill object position uncertainty caused by the respiratory gating. The result represented showed that parallel scan pattern had less dosimetric impact than the orthogonal scan pattern. This minimized the impact within less than 2% by two paintings even in the peripheral dose area. In the previous study, it was demonstrated that the parallel scan pattern had more motion tolerance than the orthogonal scan pattern in the dosimetric impact of the scanning beam delivery for free breathing, no gating or continuous, motion. In the present study, the intra-spill object motion and inter-spill object position uncertainty were also main concerns for the dosimetric impact due to non-gated motion especially in synchrotron based scanning beam delivery. However the spill length for non-gated scanning is approximately 5 second at maximum, during which the beams delivery is available, and it is more than 2~4 times longer than the duration time of the 30% duty cycle based the respiration gate (1.1 s for 3s and 2.4 s for 5 s motion) at the PTC. The intra-spill position uncertainty indeed occurs approximately once in every 4 times paintings at the same

energy layer (no energy change) with the 13×13=169 spot delivery pattern used in this experiment. Therefore the inter-spill position uncertainty might have greater impact on the dose distributions with respiratory gated scanning because the number of spills is ultimately increased by use of the respiratory gating.

The results of the dose distributions and the dose homogeneity ratio included about 6 mm motion uncertainty during the gate-on phase. These were 0.98 in a single paint and above 0.99 in more than 2 paintings with the parallel scanning pattern using respiratory gating. While the homogeneity ratios with 5 mm non-gated, or free breathing with the same parallel scan beam delivery condition performed in the chapter 6 was above 0.99 for all conditions, including the numbers paintings, any starting phase and both 3 s and 5 s motion cycles. Except the single painting, the use of respiratory gating with a certain motion amplitude within the gate-on phase in the parallel scanning pattern to the moving object can offer as the accurate beam delivery as the case of the same motion amplitude in free-breathing (without respiratory gating) with less than a 30% duty cycle gate threshold.

Similarly, regarding the orthogonal scanning pattern, the dose homogeneity ratio of the 95% and 90% isodose areas were above 0.98 for all measured conditions, including single painting. However, there was a worst case result that the dose

homogeneities of 50% isodose area with a 3 s motion cycle were ranging from 0.95 up to 0.98 regardless of the number paintings. This was associated with the starting phase effect. A similar issue occurred in the case of 5 s motion; however, there were two values of 0.97 in homogeneity and the others were above 0.98. According to the result for the same scan pattern with respiratory gating obtained in this study, the same or better dose homogeneity, 0.98, was offered from 6 paintings for both 3 and 5 s motion, and, in this case, the homogeneity of 50% isodose was better than the result of the free breathing case. This indicated that the dose distribution of the penumbra area was improved by respiratory gating.

The dosimetric impact with respiratory gating was investigated from the viewpoint of the number of paintings, scan pattern and motion cycle. The difference in the motion cycle, associated with the speed of the object motion against the scanning, turned out to have no impact on the dose distributions in the parallel scan pattern. Contrary to this, in the orthogonal scan pattern, the dose homogeneity for 3 s motion was 2~3% worse than the 5 s case for 95, 90 and 50% isodose areas from 1 up to 4 paintings, which was more influenced by the starting phase. However, there was no difference after 6 paintings.

Bert et al (2009) reported the relationship between spot size and a gate width able to preserve a 5% deviation on 1×1 mm^2 and 2×2 mm^2 scan grids. The authors found that for a 18 mm FWHM spot size, up to approximately a 6 mm gate width can offer a dose deviation within 5% on a 2×2mm^2 scan grid. The experiments in the present study produced both better and worse results than this value depending on the starting phase for the case of a single painting with same scan direction pattern (orthogonal). Since the scan grid size and object motion pattern were quite different, it is difficult to analyze the difference in these results. This difference does suggest that tighter spot spacing does not always guarantee mitigation of the interplay effect caused by motion. In carbon scanning beam delivery with respiratory gating, Furukawa (2010 and 2007) reported that the interplay effect of the carbon beam can be mitigated, with a spot size of less than half that produced by the PTC, with at least 6 paintings employing the phase control rescanning method, which utilizes a highly sophisticated synchrotron operation and beam delivery system. On the other hand, the present study demonstrated that a larger spot size can easily provide motion tolerant scanning beam delivery regardless of the intra-spill motion and inter-spill position uncertainty associated with synchrotron operation in respiratory gating. This is also achievable

with a fewer number paintings as long as an appropriate scan direction is selected, which leads to highly efficient scanning beam delivery with respiratory gating.

7.5 Conclusions

Respiratory gated spot scanning beam delivery with a synchrotron has been experimentally investigated in this study. There were some concern about the interplay effect associated specifically with synchrotron operation, inter-spill object position uncertainty and intra-spill object motion. From the experimental results with a gate level equivalent to a 30% duty cycle, which produces 6 mm motion within the gate, the scan pattern parallel to the moving object can mitigate the interplay effect in respiratory gated scanning beam delivery within a 2% difference compared with the static (no motion) dose distribution regardless of motion cycle. Even in the worse case of the orthogonal scan pattern, it is possible to reduce the dosimetric impact due to the interplay effect to 4% by 4 times paintings regardless of the motion cycle or more than 2 % difference in dose homogeneity by more than 6 times paintings compared with the no motion case.

Chapter 8. Conclusions of the dissertation and Future work

8.1 Conclusions of the dissertation

Simulation and experimental studies undergone in this dissertation provide strong supporting data for the hypotheses stated in chapter 1. In the chapter 3, figure 3-4 demonstrated that the variable flat top synchrotron operation pattern is the most efficient synchrotron operation pattern suitable for respiratory gating. Figure 3-10 showed the degree to which the efficiency is decreased for some conditions in our synchrotron based respiratory gated spot scanning beam delivery. These results provide important information when one attempts to implement respiratory gating beam delivery. These results are used to assess the efficiency of respiratory gated proton dose delivery, which is stated in specific aim 1.

Chapter 5 provides an investigation of how respiratory gated beam delivery is affected by residual motion in passively scattered mode. Figure 8-1 summarized the average values from figure3-10 and figure 5-9. The supporting data was used to analyze the precision in the beam delivery in passively scattered beam delivery mode with respiratory gating for each synchrotron operation pattern, T_{cyc}. This is the result of the passively scattered mode in specific aim 2. The overall results for passively scattered mode, from the efficiency point of view, show that the variable $_{Tcyc}$ operation

is much better than the any other T_{cyc} operation. In addition, the beam delivery is precisely undergone at a certain phase of the residual motion during beam delivery. The lower the gate threshold level is, the more precise and uniform the beam delivery is offered in passively scattered beam delivery mode. However, in this case, the efficiency of the beam delivery with respiratory gating is worse; in other words, the beam delivery time takes longer than in the case of a higher gate threshold setting.

In scanning beam mode, figures 4-3 and 4-4 in the chapter 4 showed the simulation results of the relationship between scanning target volume and beam delivery time with respiratory gating. From this one can conclude that the number of scan layers has a stronger relationship with the beam delivery time rather than the target volume (cm^3). The efficiency of the use of the proton beam, determined by MU/min, scarcely changes with the scanning volume. It is understandable that, as shown in figure 4-4, the higher the gate threshold level is, the higher the efficiency is. On the other hand, the chapter 6 and 7 showed that if the motion is less than 5 mm, the impact of the motion on the dose distribution is almost negligible, and even if the motion is larger than 5 mm, the combination of respiratory gating with the gate threshold level when the residual motion is less than 5 mm and the use of the scanning direction parallel to the target motion can achieve respiratory motion tolerant scanning

beam delivery. The beam delivery time with gating and the beam efficiency with the appropriate gate threshold level can be easily estimated from the figures 3-3 and 4-4. This is how one can easily determine the most efficient and accurate respiratory gated scanning beam delivery. These results comprise the latter part of specific aim 2 regarding scanning beam delivery mode.

Thus this dissertation has validated the hypothesis ***"Optimization of synchrotron operating parameters can lead to greater efficiency and accuracy of respiratory gating for all modes of synchrotron based proton treatment delivery"***. All the data provided in this dissertation were useful when implementing respiratory gating beam delivery for both passively scattered and scanning beam delivery mode.

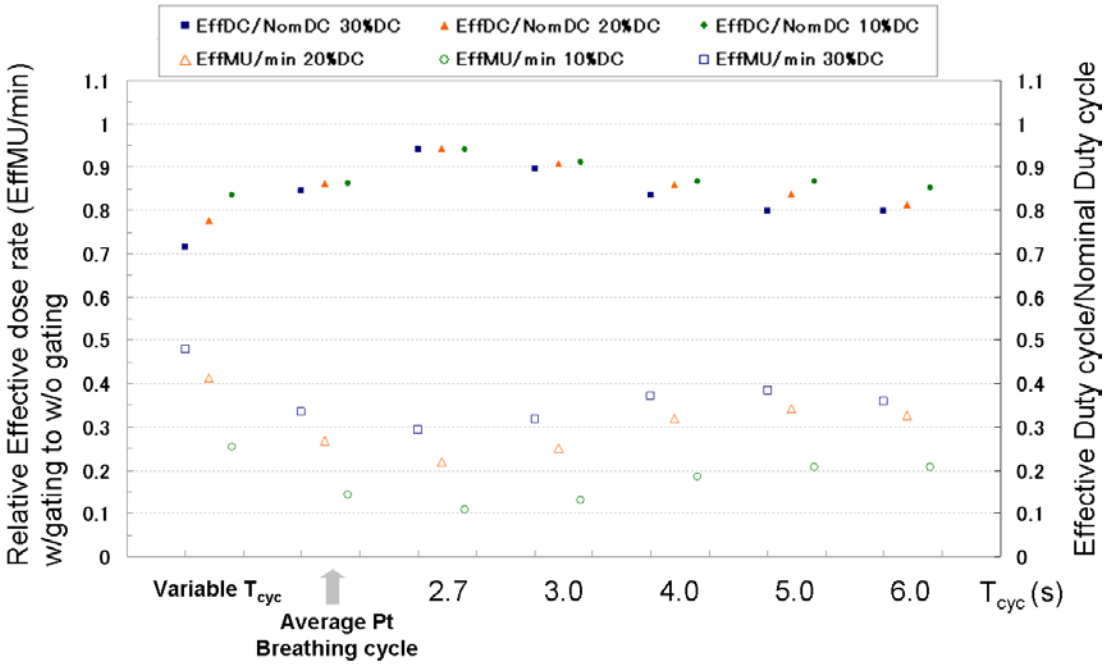

Figure 8- 1. Efficiency and precision of passively scatted respiratory gated proton beam delivery for each T_{cyc}. The open circles and squares represent the result of the ratio of the effective MU/min with gating to the effective MU/min without gating (figure 3-9 in the chapter 3). The solid circles and squares represent the ratio of effective duty cycle to nominal duty cycle (figure 5-8 in chapter 5).

8.2 Future work

This dissertation has evaluated the dosimetric impact of the motion on a single energy layer with and without the respiratory gated scanning beam delivery, and it has been measured for homogeneous and water equivalent objects only. The dosimetric impact of scanning beams in the depth direction was not taken into account. Therefore the same measurement needs to be extended into a volumetric dose distribution using a spot position (or scan) pattern composed of different energy layers, for example, a $10x10x10cm^3$ volume dose distribution. This is a more realistic evaluation accounting for scanning beam delivery to the moving target either with or without respiratory gating.

In order to deepen the respiratory gated scanning study for clinical implementation, as a first step, the same experiment needs to be performed for a very simple inhomogeneous object, composed of two materials; for example, water equivalent and air (lung) equivalent materials, with motion. From a certain beam's point of view, the water equivalent thickness dynamically varies in a moving inhomogeneous object. This causes a dosimetric impact in both the lateral and depth directions simultaneously, and it is anticipated that the dose homogeneity would be worse than the results discussed in this dissertation. Such an experiment would be

closer to the dosimetric impact occurring inside of a real patient's body. As suggested above, it is very important for respiratory gated scanning delivery to evaluate the dosimetric impact in lung because lung may best benefit by using respiratory gated scanning delivery. Since the initial validation is completed, the same study will be extended into the gated beam scanning to a volume target and then the same measurement could be performed with a more complex object, for example a lung phantom with motion. These careful investigations need to be performed for the clinical implementation of respiratory gated scanning delivery.

Bibliography

1. Anand A, Sahoo N, Zhu XR, Sawakuchi GO, Poenisch F, Amos RA, Ciangaru G, Titt U, Suzuki K, Mohan R and Gillin MT. 2010 A procedure to determine the planar integral spot dose values of proton pencil beam spots. *Med. Phys.* **39** (2), 891-899

2. Bert C and Rietzel E 2007 4D treatment planning for scanned ion beams *Radiat. Oncol.* **2** 24

3. Bert C, Gemmel A, Saito, N and Rietzel E. 2009 Gated irradiation with scanned particle beams. *Int. J. Rad Onc Biol. Phys*. **73(4)** 11270-1275

4. Bert C, Grozinger S O and Rietzel E 2008 Quantification of interplay effects of scanned particle beams and moving targets *Phys. Med. Biol.* **53** 2253–65

5. Bonett D E. 1993 Current developments in proton therapy: review *Phys. Med. Biol.* **38** 1371-1392

6. Chang J Y, Zhang X, Wang X, Kang Y, Riley B, Bilton S, Mohan R, Komaki R and Cox J D 2006 Significant reduction of normal tissue dose by proton radiotherapy compared with proton radiotherapy with three-dimensional conformal or intensity modulated radiation therapy in stage I or stage III non-small cell lung cancer *Int. J. Radiat. Oncol. Biol. Phys.* **65** 1087–1096

7. Chen G T Y, Rajinder P S, Castro J R, Lyman J T and Quivey J M 1979 Treatment planning for heavyion radiotherapy. *Int. J. Radiat. Oncol. Biol. Phys.* **5** 1809–19

8. Chiba T, Tokuue K, Matsuzaki Y, Sugahara S, Chuganji Y, Kagei K, Shoda J, Hata M, Abei M, Igaki H, Tanaka N, Akine Y 2005 Proton beam therapy for hepatocellular carcinoma: a retrospective review of 162 patients *Clin. Cancer Res.* **11** 3799–3805

9. Christoph B, Sven O G, Eike R 2008 Quantification of interplay effects of scanned particle beams and moving targets. *Phys. Med. Biol.* **53** 2253–2265

10. Engelsman M and Kooy H M 2005 Target volume dose considerations in proton beam treatment planning for lung tumors *Med. Phys.* **32** 3549–57

11. Engelsman M, Rierzel E and Kooy H M 2006 Four-dimensional proton treatment planning for lung tumors *Int. J. Radiat. Oncol. Biol. Phys.* **64** 1589–95

12. Furukawa T, Inaniwa T, Sato S, Shirai T, Shinichiro M, Takaoka E, Mizushima K, Himukai T, Noda K 2010 Moving target irradiation with fast rescanning and gating in particle therapy *Med Phys.* **37** 4874–4879

13. Furukawa T, Inaniwa T, Sato S, Tomitani T, Shinichi M, Noda K and Kanai T. 2007 Design study of a raster scanning system for moving target irradiation in heavy-ion radiotherapy. *Med. Phys.* **34** 1085-1097

14. George R, Chung T D, Vedam S S, Ramakrishnan V, Mohan R, Weiss E and Keall P J 2006 Audio-visual biofeedback for respiratory-gated radiotherapy: impact of audio instruction and audio-visual biofeedback on respiratory-gated radiotherapy *Int. J. Radiat. Oncol. Biol. Phys.* **65** 924-33

15. Gierga D P, Brewer J, Sharp G C, Betke M, Willett C G and Chen G T 2005 The correlation between internal and external markers for abdominal tumors: implications for respiratory gating *Int. J. Radiat. Oncol. Biol. Phy.* **61** 1551-8

16. Gillin M. T., Sahoo N, Bues M, Ciangaru G, Sawakuchi G., Poenisch F, Arjomandy B, Martin C, Titt U, Suzuki K, Smith A. R., and Zhu X. R 2010 Commissioning of the discrete spot scanning proton beam delivery system at The University of Texas M. D. Anderson Cancer Center, Proton Therapy Center, Houston. *Med. Phys.* **37** 154–163

17. Grozinger O S, Rietzel E, Li Q, Bert C, Harber T, Kraft G 2006 Simulations to design an online motion compensation sytem for scnned particle beams, *Phys. Med. Biol.* **51** 3517–3531

18. Hidetsugu H Nakayama, Shinji S Sugahara, Mari M Tokita, Kuniaki K Fukuda, Masashi M Mizumoto, Masato M Abei, Junichi J Shoda, Hideyuki H Sakurai, Koji

K Tsuboi and Koichi K Tokuuye 2009 Proton beam therapy for hepatocellular carcinoma: the University of Tsukuba experience *Cancer* **115(23)** 5499-506

19. ICRU Report 62 1999 Prescribing, recording, and reporting photon beam therapy (Supplement to ICRU Report 50). Bethesda, MD: International Commission on Radiation Units and Measurements
20. Inada T, Tsujii H, Hayakawa Y, Maruhashi A and Tsujii H 1992 Proton irradiation synchronized with respiratory cycle *Nippon Igaku Housyasen Gkkai Zasshi* **52** 1161–67
21. Kraus K M, Heath E and Oelfk U 2011 Dosimetric consequences of tumor motion due to respiration for a scanned proton beam *Phys. Med. Biol.* **56** 6563–6581
22. Kang Y, Zhang X, Chang Y J, Wang H, Wei X, Liao Z, Komaki R, Cox D J, Balter A P, Liu H, Zhu R X, ohan R 2007 4D Proton treatment planning strategy for mobile lung tumors. *Int. J. Radiat. Oncol., Biol., Phys.* **67** 906-914
23. Kini R V, Vedam S S, Keal J P, Patil S, Chen C, Mohan R 2003 Patient training in respiratory gated radiotherapy. *Medical Dosimetry,* **28(1)** 7–11
24. Kini V R, Vedam S S, Keall P J, Patil S, Chen C and Mohan R 2003 Patient training in respiratory-gated radiotherapy *Med. Dosim.* **28** 7–11

25. Kjellberg R N, Sweet W H, Preston W M and Koehler A M 1962 The Bragg peak of a proton beam in intracranial therapy of tumors *Trans. Am. Neurol. Assoc.* **87** 216

26. Knopf A C, Hong T S and Lomax A. 2011 Scanned proton radiotherapy for mobile targets—the effectiveness of re-scanning in the context of different treatment planning approaches and for different motion characteristics. *Phys. Med. Biol.* **56** 7257–7271

27. Koehler A M, Schneider R J and Sisterson J M 1975 Range modulators for protons and heavy ions *Nucl. Instrum. Methods* **131** 437–440

28. Koehler A M, Schneider R J and Sisterson J M 1977 Flattening of proton dose distributions for large-field radiotherapy *Med. Phys.* **4** 297–30

29. Kubo H D and Hill B C 1996 Respiration gated radiotherapy treatment: A technical study. *Phys Med Biol* **41**(1) 83–91

30. Kubo H D, Len P M, Minohara S and Mostafavi H 2000 Breathing-synchronized radiotherapy program at the University of California Davis Cancer Center *Med. Phys.* **27** 346-53

31. Lambert J, Suchowerska N, McKenzie D R and Jackson M 2005 Intrafractional motion during proton beam scanning *Phys. Med. Biol.* **50** 4853-62

32. Larsson B, Leksell L, Rexed B, Sourander P, Mair W and Anderson B 1958 The high-energy proton beam as a neurosurgical tool *Nature* **182** 1222

33. Li Q, Groezinger S O, Haberer T, Rietzel E and Kraft G. 2004 Online compensation for target motion with scanned particle beams: simulation environment Phys. *Med. Biol.* **49** 3029-46

34. Lu H M, Brett R, Sharp G, Safai S, Jiang S, Flanz J and Kooy H 2007 A respiratory-gated treatment system for proton therapy. Med Phys **34(8)** 3273-3278

35. Lujan A E, Larsen E W, Balter J M, and Ten Haken R. K 1999 A method for incorporating organ motion due to breathing into 3D dose calculations *Med.Phys.* **26** 715-720

36. Mageras G S and York E 2004 Deep inspiration breath hold and respiratory gating strategies for reducing organ motion in radiation treatment *Semin. Radiat. Oncol.,* **14(1)** 65-75

37. Minohara S, Endo M, Kanai T, Kato H and Tsujii H 2003 Estimating uncertainties of the geometrical range of particle radiotherapy during respiration. *Int. J. Radiat. Oncol. Biol. Phys.* **56** 121-125

38. Minohara S, Kanai T, Endo M, Noda K and Kanazawa M 2000 Respiratory gated irradiation system for heavy-ion radiotherapy *Int. J. Radiat. Oncol. Biol. Phys.* 47 1097-103

39. Mori S, Chen G T Y and Endo M 2007 Effect of intrafractional motion on water equivalent path length in respiratory-gated heavy charged particle beam radiotherapy. *Int. J. Radiat. Oncol. Biol. Phys.* **70** 308-317

40. Mori S, Wolfgang J, Lu H M, Schneider R, Choi C N, Chen T Y G 2008 Quantitative assessment of range fluctuations in charged particle lung irradiation. *Int. J. Radiat. Oncol., Biol., Phys.***70** 253-261

41. Mori S, Yanagi T, Hara R, Sharp G C, Asakuma H, Kumagai M, Kishimoto R, Yamada S, Kato H, Kandatsu S, Kamada T 2010 Comparison of respiratory-gated and respiratory un-gated planning in scattered carbon ion treatment of the pancreas using four-dimensional computed tomography. *Int. J. Radiat. Oncol. Biol. Phys.* **76** 303-312

42. Noda K, Kanazawa M, Itano A, Takeda E, Torikoshi M, Araki N, Yoshizawa J, SatoK, Yamada S, Ogawa H, Itoh H, Noda A, Tomizawa M, and M Yoshizawa 1996 Slow beam extraction by a transverse RF field with AM and FM. *Nucl. Instr. and Meth.* **A374** 269-277

43. Ohara K, Okumura T, Akisada M, Inada T, Mori T, Yokota H, Calaguas M J B. 1989 Irradiation synchronized with respiration gate. *Int. J. Radiat. Oncol. Biol. Phys.* **17** 853-857

44. Ozhasoglu C and Murphy M J. 2002 Issues in respiratory motion compensation during external-beam radiotherapy *Int. J. Radiat. Oncol. Biol. Phys.* **52** 1389-99

45. Paganetti H, Jiang H and Trofimov A 2005 4D Monte Carlo simulation of proton beam scanning: modelling of variations in time and space to study the interplay between scanning pattern and time-dependent patient geometry. *Phys. Med. Biol.* **50** 983–990

46. Pedroni E, Bacher R, Blattmann H, Bohringer T, Coray A, Lomax A, Lin S, Munkel G, Scheib S, Scneider U and Tourovsky A 1995 The 200MeV proton therapy project at the Paul scherrer institute: conceptual design and practical realization. *Med. Phys.* **22(1)** 37-53.

47. Phillips M H, Pedroni E, Blattmann H, Boehringer T, Coray A and Scheib S. 1992 Effects of respiratory motion on dose uniformity with a charged particle scanning method *Phys. Med. Biol.* **37** 223-234

48. American Association of Physicists in Medicine. 2006 Report of AAPM Task Group 76

49. Schulz-Ertner D, Jakel O and Schlegel W 2006 Radiation therapy with charged particles *Semin. Radiat. Oncol.* **16** 249-59

50. Seppenwoolde Y, Shirato H, Kitamura K, Shimizu S, Herk M V, Lebesque J V, Miyasaka K 2002 Precise and real-time measurement of 3D tumor motion in lung due to breathing and heartbeat, measured during radiotherapy. *Int J Radiat Oncol Biol Phys* **53** 822-834

51. Shinji S Sugahara, Koichi K Tokuuye, Toshiyuki T Okumura, Akira A Nakahara, Yukihisa Y Saida, Kenji K Kagei, Kiyoshi K Ohara, Masaharu M Hata, Hiroshi H Igaki and Yasuyuki Y Akine 2005 Clinical results of proton beam therapy for cancer of the esophagus *Int. J. Radiat. Oncol. Biol. Phys.* **61(1)** 76-84

52. Shioyama Y, Tokuue K, Okumura T, Kagei K, Sugawara S, Ohara K, Akine Y, Ishikawa S, Sato H Sekizawa K 2003 Clinical evaluation of proton radiotherapy for non-small-cell lung cancer. *Int. J. Radiat. Oncol. Biol. Phys.* **56(1)** 7–13

53. Shirato H, Seppenwoolde Y, Kitamura K, Onimaru R and Shimizu S 2004 Intrafractional tumor motion: Lung and Liver. *Semin. Radiat. Oncol.* 14(1) 10-18

54. Shirato H, Shimizu S, Kitamura K, Nishioka T, Kagei K, Hashimoto S, Aoyama H, Kunieda T, Shinohara N, Dosaka A H, Miyasaka K. 2000 Four-dimensional

treatment planning and fluoroscopic real-time tumor tracking radiotherapy for moving tumor. *Int J Radiat Oncol Biol Phys* **48** 435-442

55. Shirato H, Shimizu S, Kunieda T, Kitamura K, van Herk M, Kagei K, Nishioka T, Hashimoto S, Fujita K, Aoyama H, Tsuchiya K, Kudo K, Miyasaka K 2000 Physical aspects of a real-time tumor-tracking system for gated radiotherapy *Int. J. Radiat. Oncol. Biol. Phys.* **48** 1187–1195
56. Shirato H, Shimizu S, Shimizu T, Shimizu T, Nishioka T, Miyasaka K 1999 Real-time tumour-tracking radiotherapy *Lancet* **353** 1331-1332
57. Slater J M, Archambeau J O, Miller D W, Notarus M I, Preston W and Slater J D 1991 The proton treatment center at Loma Linda University Medical Center *Int. J. Radiat. Oncol Biol. Phys.* **22** 383
58. Smith A R 2006 Proton therapy. *Phys. Med. Biol.* **5(**1) R491–R504
59. Tobias C A, Lawrence J H, Born J L, McCombs R K, Roberts J E, Anger H O, Low-Beer B V A and Huggins C B 1958 Pituitary irradiation with high-energy proton beams: a preliminary report *Cancer Res.* **18** 121
60. Tomizawa M, Yoshizawa M, Chida K, Yoshizawa J, Arakaki Y, Nagai R, Mizobuchi A, Noda A, Noda A, Kanazawa K, Ando A, Muto H and Hattori T 1993 A Slow beam extraction at TARN II *Nucl. Instr. and Meth.* **A326** 399-406

61. Tsujii H, Tsuji H, Inada T,Maruhashi A, Hyakawa Y, Takada Y, Tada J, Fukumoto S, tatuzaki H, Ohara K, Kitagawa T 1993 Clinical results of fractionated proton therapy *Int. J. Radiat. Oncol. Biol. Phys.* **25(1)** 49-60

62. Tsunashima Y, Sakae T, Shioyama Y, Kagei K, Terunuma T, Nohtomi A and Akine Y 2004 Correlation between the respiratory waveform measured using a respiratory sensor and 3D tumor motion in gated radiotherapy *Int. J. Radiat. Oncol. Biol. Phys.* **60** 951-958

63. Tsunashima Y, Vedam S, Dong S, Umezawa M, Sakae T, Bues M, Balter P, Smith A and Mohan R 2008 Efficiency of respiratory-gated delivery of synchrotron-based pulsed proton irradiation *Phys. Med. Biol.* **53** 1947–1959

64. Underberg R W M, Lagerwaard R J, Slotman B J, Cuupers J P and Seman S 2005 Use of Masimum intensity projections (MIP) for target volume generation in 4DCT scans for lung cancer. *In.t .J Radiat. Oncol. Biol. Phys.* **63(2)** 254-260

65. Vedam S S, Kini V R, Keall P J, Ramakrishnan V, Mostafavi H and Mohan R 2003 Quantifying the predictability of diaphragm motion during respiration with a noninvasive external marker Med. Phys. **30** 505-13

66. Water S van de, Kreuger R, Zenklusen S, Hug E, and A J Lomax 2009 Tumor tracking with scanned proton beams: assessing the accuracy and practicalities *Phys. Med. Biol.* **54** 6549-6563

67. Wilson R. R. 1946 Radiological Use of Fast Protons *Radiology* **47** 487-491

68. Wong W J, Sharpe B M, Jaffaray A D, Kini R V, Robertson M J, Stromberg S J, Martinez A A 1999 The use of active breathing control (ABC) to reduce margin for breathing motion *Int. J. Radiat. Oncol. Biol. Phys.* **44** 911-919

69. Zhang X, Li Y, Pan X, Li X, Mohan R, Komaki R, Cox J D, Chan J Y. 2010 Intensity-modulated proton therapy reduces the dose to normal time compared with intensity-moderated radiation therapy or passive scattering proton therapy and enables individualized radical radiotherapy for extensive stage IIB non-small lung cancer: available clinic study *Int. J. Radiat. Oncol. Biol. Phys.* **77(2)** 357–366

70. Zhu XR, Sahoo N, Zhang X, Robertson D, Li H, Choi S, Lee A K, Gillin M. T 2010 Intensity modulated proton therapy treatment planning using single-field optimization: The impact of monitor unit constraints on plan quality. *Med. Phys.* **37** 1210–1219

Vita

Yoshikazu Tsunashima was born in Asahikawa, Japan on April 14, 1975, the second son of Kazuyoshi and Ritsuko Tsunashima.

Yoshikazu graduated from Hokkaido Asahikawa Kita High School in 1993. He then attended the College of Medical Technology, Hokkaido University, Hokkaido, Japan, where he graduated with a major in radiation technology and he simultaneously earned a certificate as a *Radiological Technologist (Radiation Therapist)* in June 1998. In 1998 after graduation, he transferred to the Tokyo University of Science, Tokyo, Japan and graduated with a major in physics in 2000. In April 2000 he started to work at the Proton Medical Research Center of the University of Tsukuba, Ibaraki, Japan and he earned five years of experience there as a radiation therapist. In 2001, he entered the graduate medical science program, University of Tsukuba, Ibaraki, Japan while still employed as a radiation therapist, and received his M.S. in Radiation Biology and Physical Engineering in March 2003. In 2006 he then entered the Medical Physics program of The University of Texas Graduate School of Biomedical Sciences at Houston.